UNIVERSITY OF CALIFORNIA, MERCED

Self-assembled nanoparticles for sensing and functionalized for charge transfer and cargo encapsulation applications

A dissertation submitted in partial satisfaction of the requirements for the degree

Doctor of Philosophy

in

Materials and Biomaterials Science and Engineering

by

Mark Bartolo

Committee in charge:
Professor Jay Sharping, Chair
Professor Ryan Baxter
Professor Sayantani Ghosh

2021

The dissertation of Mark Bartolo is approved, and it is acceptable in quality and form for publication on microfilm and electronically:

Professor Jay Sharping, Committee Chair Date

Professor Ryan Baxter, Committee Member Date

Professor Sayantani Ghosh, Committee Member Date

University of California, Merced

2021

This work is dedicated to:

- Maria, my beloved wife, for her constant love, encouragement, and support.
- To my parents, Roberto Bartolo and Vilma Bartolo, for always believing in me, even when I did not believe in myself. Their love, encouragement, patience, and sacrifices provided inspiration.
- To my in-laws, Antonio and Dominga, for their utmost support and constructive criticisms for a good moral compass.

Table of Contents

List of Abbreviations

NPs	Nanoparticles
AuNPs	Gold nanoparticles
QDs	Quantum dots
CdSe	Cadmium selenide
ZnS	Zinc sulfide
CZ	CdSe/ZnS
Fe	Iron
F_3O_4	Magnetite
MNP	Magnetic nanoparticle
LC	Liquid crystal
SL	Superlattice
a-Si	Amorphous silicon
MoSi	Molybdenum silicide
EDS	Energy dispersive spectroscopy
TEAM	Transmission electron aberration-corrected microscopy
L-TEAM	Lorentz mode transmission electron aberration-corrected microscopy
ODA	Octadecylamine
BIP	Bis(imino)pyridine
BIP-H	Unsubstituted BIP
BIP-Me	Dimethyl BIP
BIP-iPr	Diisopropyl BIP
RNI	Redox non-innocent
HOMO	Highest occupied molecular orbital
TAT	Triazatruxene
PL	Photoluminescence
PLQY	Photoluminescent quantum yield
TRPL	Time-resolved photoluminescence
SPAD	Single photon avalanche diode
TCSPC	Time-correlated single photon counting
MO	Magneto-optics
MOKE	Magneto-optical Kerr effect
PMOKE	Polar magneto-optical Kerr effect
LMOKE	Longitudinal magneto-optical Kerr effect
TMOKE	Transverse magneto-optical Kerr effect
PEM	Photo-elastic modulator
LCP	Left circularly polarized
RCP	Right circularly polarized
5CB	4-cyano-4’-pentylbiphenyl
DLS	Dynamic light scattering
DDS	Drug delivery system
ITO	Indium tin oxide
n-ZnO	n-type zinc oxide

FRET	Forster resonance energy transfer
fwhm	Full width half max
NMR	Nuclear magnetic resonance
2,6-DAB	2,6-Diacetylbenzene
2,6-DAP	2,6-Diacetylpyridine
CTAB	cetyltrimethylammonium bromide
SEM	Scanning electron microscopy
TEM	Transmission electron microscopy
DSC	Differential scanning calorimetry
ANSI	American national standards institute
wt%	Weight percent
rpm	Revolutions per minute
mW	Milliwatt
mT	Millitesla
eV	Electronvolt
keV	kiloelectronvolt
mg	Milligram
mL	Milliliter
μL	Microliter
m	Meter
nm	Nanometer
µm	Micrometer
Hz	Hertz
s	Second
ns	Nanosecond
MeCN	Acetonitrile
$CHCl_3$	Chloroform
mct	Microcentrifuge tube

List of Symbols

θ_k	Kerr rotation
φ_k	Kerr ellipticity
Φ_K	Kerr angle
n	index of refraction
ε	permittivity
ω_{PEM}	Resonant frequency of PEM
δ(t)	Phase modulation
β	Phase modulation amplitude
D	Thickness of PEM crystal
λ	Wavelength
π	Pi conjugated system
Å	Angstrom
τ	Recombination lifetime
r	Interdot separation
ε_{total}	Total efficiency
ε_{FRET}	FRET efficiency
τ_{film}	Recombination lifetime of thin film
$\tau_{solution}$	Recombination lifetime in solution
R_0	Forster distance where FRET is 50%
η	Charge transfer efficiency
P_{IN}	Effective pressure between nematic and isotropic phases
δf_{IN}	Change in free energy between nematic and isotropic phases
γ	Compressive stress
t_S	Shell thickness
R_S	Shell radius
δG_P	Free Energy cost
T_{IN}	Thermotropic phase transition form isotropic to nematic

Table of Figures

Acknowledgements

This dissertation would not have been possible without the help and support of so many people.

I would like to express my utmost gratitude to my Ph.D. advisor Sayantani Ghosh for her support and guidance on academic, professional, and personal issues throughout graduate school. She has been a supporting and inspirational mentor during my years at UC Merced. This work would not have been possible without her vision, guidance, knowledge, and expertise. Thank you, Sai for being a great mentor, friend, and a member of your lab. It has been a rewarding experience.

I would like to express my sincere appreciation of Professor Ryan Baxter who has collaborated in the projects within this thesis.

Additionally, I express my appreciation for my committee chair, Jay Sharping for his support, suggestions, guidance, and insightful comments.

I am grateful for the funding sources that allowed me to pursue my graduate school studies: Center for Cellular and Biomolecular Machines (CCBM) Fellowship, Physics Graduate Program, Materials and Biomaterials Science and Engineering (MBSE) Bobcat Fellowship, Merced nAnomaterials Center for Energy and Sensing (MACES) Summer Fellowship.

Without all the people who have provided significant influence on my career, this work would not exist. Words are not enough how grateful I am to all of you.

Curriculum Vitae

Mark De La Cruz Bartolo

3746 Morning Glory Ave • Merced, CA • 95348 USA
(760) 716-8695
mdbartolo@gmail.com
https://www.linkedin.com/in/markdbartolo/
https://github.com/lavarius

Summary

- PhD in materials and biomaterials science and engineering with a focus on **nanoparticle self-assembly** in **soft matter** research and strong interests in data science tools and methodologies
- Materials research
    - Chemical synthesis,
    - electrical, spectral and electron microscopy characterization, and
    - experimental design and implementation
- Strengths in analytical and technical communication, collaboration, and teamwork to accomplish objectives

Education

2015-05/2021 **Ph.D.**, Materials and biomaterials science and engineering, University of California Merced
GPA: 3.74

2015 **BS**, Applied Physics with Concentration in Applied Electronics, California State University San Marcos
GPA (last 60 units): 3.534

2013-Present Independent Learning through Udemy, SuperDataScience, DataCamp
- Statistics for Business Analytics and Data Science A-Z
- SQL Fundamentals, Intermediate, Joining Data
- Intermediate Python, Data Science Tools
- Machine Learning A-Z (In Progress)

Research Experience

2015-Present **Graduate student research assistant in materials science at University of California Merced**
PI: Sayantani Ghosh PhD
Explored self-assembly in soft matter, materials science, data science, and major principles of biochemistry
Research concentration: Develop applications in drug delivery, tissue engineering, material platforms for light matter interactions, and sensing

Project Management

- Oversaw project lifetime as resulted from 2 publications
- Built laser optics system for spectral data acquisition with optical equipment for 4 spectroscopic experimental setups for 5 projects
  - Photoluminescence
  - Time correlated photoluminescence
  - Scanning photoluminescence
  - Magneto-optical Kerr Effect (Polar)
- Planned and executed experimental design for a major project that fostered 3 cross functional collaborations

Information Management

- Authored and edited materials and process specifications for 5 projects
- Documented analysis, recommendations, implemented solutions, plans, and presentations reflecting status and results of projects in progress on a weekly basis providing 140+ reports
- Parsed, analyzed, and mapped data with MATLAB scripts resulting in 360 2D mapped data

Innovation

- Integrated automated data acquisition via AutoHotkey script saving 6+ hours of time
- Cultivated cross functional collaborations in surface material development for nanoparticle functionalization resulting in 1 protocol for the self-assembly of micro-shell platform
- Troubleshooted and adjusted optical experimental setups for more than 50% improved signal acquisition
- Programmed, tested, and assessed micron precisions optical translation stages and spectrometer for actuation & data acquisition using LabVIEW resulting in 100k+ points of data

Communication

- Conveyed work through presentations at 10 events and briefed course materials to 240 students
- Mentored interdisciplinary team of undergraduate and graduate students with defined procedures and processes accomplishing 4 objectives
- Demonstrated module of surface area to volume ratios co-developed in a high school development workshop to 120 students

2013-2015 **Undergraduate Student Research Assistant in physics and chemistry at California State University San Marcos**
PI: Stephen Tsui PhD
Co-PI: Eric Reinheimer PhD

Explored inorganic & organic chemical synthesis, computer science, embedded systems programming, and mathematics

Applied Research Methods

- Synthesized organic crystals based on tetrathiafulvalene and measured resistivity versus temperature
  - Used automated data acquisition with LabVIEW
  - Communicated with a temperature controller and SR850 Digital Signal Processing Lock-In Amplifier
- Superconductor pellet synthesis of $YBa_2Cu_3O_{7-g}$ (YCBO)
- Basic LabView Programming

Communication and Leadership

- Mentored Office for Training, Research and Education in the Sciences (OTRES) Scholar during Summer 2014
- Conveyed work through presentations at meetings and 3 events

Embedded Systems Programming

- Interfacing with AVR microcontroller to program a omnidirectional wheel robot that avoids objects via 2 infrared sensors
- Object oriented programming in C/C++ • Read, Design, Implement, Test, and Correct programs • Data structure using linked list using pointers, recursion, stack, queue, and trees

Summer 2013 Summer Research Experience for Undergraduates (REU) program for characterization of advanced materials at Washington State University
PI: Soumik Banerjee PhD

- Computational modeling and analysis of a binary system of the photoactive layer of organic photovoltaic cells by utilizing a standard computational model via GROMACS
- Determined a suitable donor molecule for organic photovoltaic cells

Teaching Experience

- Lead undergraduate discussion & lab sections, exam proctoring, and office hours as a teaching assistant
- Physics 08: Introductory Physics I (Mechanics)
- Physics 09: Introductory Physics II (Electricity and Magnetism)
- Physics 19: Physics II – Bio Majors

Awards and Honors

2020 Spring	2020 NSF-Crest Center for Cellular and Bio-Molecular Machines (CCBM) Fellowship
2019 Fall	2019 NSF-Crest Center for Cellular and Bio-Molecular Machines (CCBM) Fellowship
2019 Summer	2019 Summer Materials and Biomaterials Science and Engineering (MBSE) Bobcat Fellowship
2017 March	2017 Merced nAnomaterials Center for Energy and Sensing (MACES) Summer Research Fellowship
2016 August	NSF-Crest Center for Cellular and Bio-Molecular Machines (CCBM) Scholar
2016 April	2016 Merced Nanomaterials Center for Energy and Sensing (MACES) Summer Research Fellowship
2015 Sept	Graduate Dean's Relocation Award
2014-2015	Sigma Pi Sigma Physics Honor Society
2014-2015	Louis Stokes Alliance for Minority Participation (LSAMP) – Program for Recognition Undergraduate Distinction (PROUD) Research Award
2013-2015	Maximizing Access to Research Careers (MARC), Award recipient [T34]
2013-2015	CSUSM Dean's List, College of Sciences and Mathematics
2013-2015	Louis Stokes Alliance for Minority Participation (LSAMP) Scholar recipient

Peer Reviewed Publications

Google Scholar link

Mark Bartolo, Ryan Brisbin, James C. Fettinger, Sayantani Ghosh, Ryan Baxter, *Impact of Bis(imino)pyridine Ligands on Mesoscale Properties of CdSe/ZnS Quantum Dots.* J. Phys. Chem. C, 124, 41, 22677-22683, 2020

Mark Bartolo, Jose Amaral, Linda. S. Hirst, and Sayantani Ghosh, *Directed assembly of magnetic and semiconducting nanoparticles with tunable and synergistic functionality,* Scientific Reports, 9 15785, 2019

Dylan Kimball, Raechel Munns, Steven P. Fischer, **Mark Bartolo**, Jose Valdez, Simmon J. Teat, Stephen Tsui, Eric W. Reinheime, *Utilizing Perylene in New Organic Donor-Acceptor Materials: Highlighting the Synthesis, Structure and Physical Properties of Perylene-pDNB and Perylene-TCNP,* Journal of Chemical Crystallography, vol 45 (4) p. 169-177, 2015

S. P. Fisher, S. C. Keene, **M. Bartolo**, S. Tsui, and E. Reinheimer, *Identification and Analysis of a New Organic Donor-Acceptor Material: Synthesis, Structure, Spectroscopy and Transport Properties of the 2:1 Complex o-Me_2TTF-pDNB*, Journal of Chemical Crystallography vol. 44 (5) p. 261-268, 2014

Technical Seminars and Workshops

Mark Bartolo, Ryan Brisbin, Sayatani Ghosh, Ryan Baxter, Tuning nano-assembled shell sizes with BIP ligands, External Advisory Board Virtual Presentation, UC Merced, CA, September 2020

Mark Bartolo, Ryan Brisbin, Sayantani Ghosh, Ryan Baxter, Discovery of ligand controlled self-assembling nano-shells, Oral Presentation, CSU Stanislaus, Turlock, CA, February 2020

Mark Bartolo, Randy Espinoza, Jussi Amaral, Sayantani Ghosh, *Optimizing parameters in co-assembly of magnetic and semiconducting nanoparticles templated by iquid crystal phase transition*, Oral Presentation, American Physical Society, Los Angeles, CA, March 2018

Mark Bartolo, Randy Espinoza, Jussi Amaral, Sayantani Ghosh, *Nano-assembled synergistic magneto-optical sensors*, Oral Presentation, American Physical Society – Far West, Merced, CA, 2017

Light/matter interactions at the nano-bio interface, University of Illinois at Urbana-Champaign, Fall 2016, Workshop

Mark Bartolo, Randy Espinoza, Jussi Amaral, Sayantani Ghosh, *Tuning the synergistic functionality of semiconducting and magnetic nanoparticle co-assemblies*, Oral Presentation, American Physical Society, New Orleans, LA, March 2017

Mark Bartolo, S. Tsui, E. Reinheimer, *Synthesis and Characterization of Tetrathiafulvalene Derivatives*. Poster Presentation, American Physical Society, San Antonio, TX, March 2015

Mark Bartolo, S. Tsui, E. Reinheimer, *IR Spectrum and Electrical Transport Characterization of DMDT-TCNB*. Oral Presentation at the Symposium on Student Research, Creative Activities & Innovation CSUSM, San Marcos, CA February 2015

Mark Bartolo, S. Tsui, E. Reinheimer, *Characterization and Comparison of DMTTF-pDNB and DMTTF-TCNQ*. Oral Presentation at the Symposium on Student Research, Creative Activities & Innovation CSUSM, San Marcos, CA 2014

Mark Bartolo, S.M. Mortuza, and Soumik Banerjee, *Modeling Donor-Acceptor Copolymers Used in the Photoactive Layer of Organic Photovoltaic Cells*, Oral Presentations at the UCSD Summer Research Conference, University of California San Diego; CSUSM Frontiers of Science; Invitation by Office for Training Research and Education in the Sciences CSUSM San Marcos, CA August 2013

S. M. Mortuza, C. Cisneros, **M. Bartolo**, and S. Banerjee, *Molecular modeling of nanoparticles and conjugated polymers during synthesis of photoactive layers of organic photovoltaic solar cells*, Oral Presentation at the Proceedings of AlChE Annual Meeting, San Francisco, August CA 2013

Mark Bartolo, S.M. Mortuza, Soumik Banerjee, *Modeling Donor-Acceptor Copolymers Used in the Photoactive Layer of Organic Photovoltaic Cells*, Summer Research Poster Presentation, Washington State University, Pullman, WA August 2013

Community Involvement

2020 February oral presentation seminar for CCBM & MACES outreach at CSU Stanislaus

2019 February Student Poster presentation for MBSE graduate student visitation week

2018 October CCBM Poster Presentation at Annual open house and advisory board meeting

2018 Yosemite National Park Face Lift

2018 Volunteer at Merced County Special Olympics

2017 CCBM Outreach event for Burbank/Peterson Elementary Schools

- Escort and helium demo

2016 Buhach Colony High School Nanoscience Module with Merced nAnomaterials Center of Energy and Sensing (MACES)

- Lectured topic of surface area to volume ratios
- Led alka seltzer experiment

2016 High School Curriculum Development Workshop

- Development of classroom modules to be included in high school classrooms

2015 Peterson Elementary Kindergarteners Merced Campus Visit

- Demonstration of the difference between light and lasers

2015 Summer Research Training Program (SRTP), San Marcos, CA

- Termite wrangler
- Poster presentation moderator
- SRTP student supervisor of physics and chemistry based projects
- Senior scholar representative

2015 Super STEM Saturday Volunteer, San Marcos, CA

- Presented the amount of sugars in the common beverages that society drinks and what their effects have on adults versus children
- Demonstrated mechanical power and electromagnetism, electrostatics, and inertia

2014 Super STEM Saturday Volunteer, San Marcos, CA

- Demonstrated the autonomous activity of low level programming of microcontrollers.

2013 Annual Robotics Expo Volunteer; CSUSM Physics Department, San Marcos California

- Demonstrated robots that were programmed and interfaced at the hardware layer.

Skills/Techniques/Software

- Statistics
- Python | SQL | C/C++
- Machine Learning
- Data Analysis
- Detailed Design
- Implementation
- Illustrator & Premiere Pro
- Photoshop
- Microsoft Office 365
- Excel Pivot Tables
- HTML5 & CSS
- Image Analysis (FIJI/ImageJ)
- Optics
- Optical & electron microscopy
- AutoCAD | SolidWorks
- Electronics
- LabVIEW | MATLAB

Relevant Software Skills

MS Office Suite; C/ C++; LabVIEW; SolidWorks; AutoCAD; MasterCAM;

Relevant Hardware Skills

Analog Circuit Analysis and Troubleshooting; SR850 lock-in amplifier; Janis ST-100 cryostat

Membership of Professional Organizations

Association for Computing Machinery (ACM)
American Society of Mechanical Engineers (ASME)
American Physical Society (APS)
Society of Physics Students (SPS)
Society for Advancement of Hispanics/Chicanos and Native Americans in Science (SACNAS)
SuperDataScience | DataScienceGo
DataCamp

Abstract

Self-assembled nanoparticles for sensing and functionalized for charge transfer and cargo encapsulation applications

By

Mark Bartolo

Doctor of Philosophy in Materials and Biomaterials Science and Engineering

University of California, Merced

2021

Professor Jay Sharping, Chair

The interactions of semiconducting quantum dots (QDs) and Fe_3O_4 magnetic nanoparticles (MNPs) co-assembled together with thermotropic liquid crystalline (LC) materials are studied in this work. LC materials allow for bottom-up organization of nanoparticles via thermotropic phase transition. Using nanomaterials as building blocks to create new materials with meta functionalities is of great interest in the materials design and synthesis space.

The first study is about dispersing QDs and MNPs together within isotropic LC and co-assembling them into clusters driven by the LC's thermotropic phase transition. The co-assemblies are micron-size clusters that can be modulated in situ by applied magnetic fields <250 mT that results in the enhancement of QD photoluminescence (PL). The enhancement is reversible in clusters that have MNPs smaller than 10 nm. Using transmission electron microscopy (TEM) and energy dispersive spectroscopy, nanoscale placement of QDs are shown to be aggregated in the center, and MNPs are dispersed throughout the cluster volume. MNPs in LC were observed to be able to rotate and align along the direction of the applied magnetic field with Lorentz TEM. This rotation and alignment are attributed to the cause for PL enhancement. By correlating multiscale spectroscopy and microscopy characterization, this part highlights how the interactions in the nanoscale can manifest in the microscale. This co-assembly of QDs and MNPs is a reversible magnetic field sensor where the emission intensity is tuned by an applied magnetic field.

Second, this work covers research done on the addition of charge transfer capabilities to CdSe/ZnS (CZ) QDs and the self-assembly of shells with CZ QDs with LC thermotropic phase transition. Concepts such as surface functionalization and biomaterial strategies for controlled delivery in applications such as drug delivery and tissue engineering are discussed. Surface functionalized NPs with bis(imino)pyridine (BIP) are studied. BIP molecules are a class of molecules that are normally used in base metal charge

transfer on the molecular scale. BIPs behavior in the nano and micro scale were unexplored and here we made some interesting discoveries. From crystallography and TEM, we observed that the BIP molecules alter NP interdot separation in QD films. Using ultrafast spectroscopy we were able to determine that due to this interdot separation, the optical and electronic properties were altered. With three different types of BIPs, improved energy and charge transfer were observed. The study also found that the BIP ligands were able to stabilize the QD emission quicker than the native octadecylamine ligands.

Third, is a continuation of the second, utilizing the BIP ligands allowing for the controllable size distribution of shell formation when self-assembled using thermotropic LC. Over the years, the Ghosh group and collaborators have developed self-assembled microstructures composed of semiconducting QDs and AuNPs that were functionalized with custom-designed ligands. In this work, I have focused on a new group of ligands, the BIP ligands, which are much smaller and could improve stability, optical properties, biocompatibility, and possibly allow cargo release via electrochemical stimulation. Additionally, it offers a controllable size tunability of the assembled structures based on changing the alkyl group on the BIP molecule. With this size tunability, an optimal nanostructure assembly may be utilized in cargo encapsulation systems.

The main goal of this research combines increasing the functionality of QDs or nanoparticles in general, and utilizing surface modification with customized ligands to make them electro-responsive. The use of these ligands are currently good at being photogenerated hole acceptors, provide non-toxic properties to NPs, and the utility of allowing NPs to assemble to shells from LC thermotropic phase transition. The combination of these features allows the use of these materials in charge transfer devices, drug delivery, and tissue engineering platforms.

Chapter 1 Introduction and Overview

Motivation and Overview

Nanomaterials are the materials with less than 100 nm size in at least on dimension. The nanomaterials show different physiochemical properties than that of their bulk counterparts which inherently depends on their size and shape. By modifying the shape and size at the nanoscale, nanomaterials can exhibit capabilities and unique characteristics. The common shapes and sizes are nanorods, nanoparticles, nanosheets. They can be categorized based on dimensions such as zero-dimensional for nanoparticles, one dimensional for nanorods or nanotubes, and two dimensional for films and layers. Nanomaterial types consist of carbon-based, metal, semiconductor, polymeric, and lipid-based types.

Ferrite nanoparticles are used in a wide range of fields due to magnetic, electrical, optical and chemical properties. Their applications range from medical to modern industries, such as biomedical[1] and the dye industry [2] to name a few. In terms of bioapplications, some nanoparticles (NPs) inherently have cytotoxic effects on cells and uptake efficiently thereby limiting their use in clinical practice. By modifying their physico-chemical properties, nanoparticles that undergo surface modification gain enhanced biocompatibility and cellular uptake[3–5].

In this work, we are using NPs to assemble an ensemble nanostructure or microstructure using a self-assembly method using liquid crystals. I have used various sized CdSe/ZnS quantum dots (QDs) and magnetic nanoparticles, 5 and 10 nm in diameter. Two projects emphasized in magneto-optical sensing and the other in tissue engineering and drug delivery.

While QDs have been previously used in various applications [6–10], they are inherently hydrophobic and need their surfaces to be functionalized with organic ligands (surfactants) that prevent them from aggregating and increases their aqueous solubility for applications in biological environments. This chapter lays out some of the introductory concepts, parameters, and applications for nanoparticle self-assembly.

Nanoparticle assemblies and their applications

A current goal in nanotechnology focuses on the autonomous-assembly or self-assembly of different nanoparticle types into 3D organized structures or superstructures that give way to emergence of material properties that are not normally found in nature. The assembly can be done either directed with external stimuli or autonomously without any external stimuli. The idea of self-assembly is not new as it is a natural phenomenon

where natural materials are made, but the potential to create programmed matter from the molecule-scale on up is exciting. The types of emergent material properties and their applications span a wide range. There is optical property enhancement[11], mechanical resilience[12], water treatment[13], drug delivery, to high-density data storage [14].

Such superstructures can mimic the behavior of natural materials[15], however, natural materials may not have flexibility in altering subunits of the overall superstructure to allow access to a range of tunable nanomaterials. By altering subunits that make up the building blocks of superstructures such as ligands, polymers, nanoparticles, or template medium, the self-assembly parameters are changed. The self-assembly results can range from clusters to tunable 1D, 2D arrays or 3D structures.

Most nanoparticle assembly processes are enabled by the surfactant molecules or ligands on the surface of the nanoparticle. In doing so nanoparticles can become dipolar to assemble into a chain-like structure without a template [16], creating helical structures with liquid crystal templating[17], and the formation of shells[18] for example. By altering a nanoparticle's surface, there are opportunities that result in the capability of making them multifunctional. When multifunctional, the nanoparticles are open to a applications in biological systems if devised with stealth like features to evade the immune system, ensure membrane permeation, protect cargo, or provide specific targeting.

In self-assembly, the components (nanoparticles, ligands, host material, etc.) are autonomously organized into patterns or structures which are commonly seen throughout nature and technology. Bottom-up self-assembly provides a practical approach to synthesizing functional nano – micro scale structures applicable to electronics [7,19], drug delivery[20–22], photonics [13], sensors and others. Some examples of directed self-assembly are superlattices and microstructures.

Superlattices

Nanoparticles can be assembled into ordered arrays resulting in lattice structures similar to crystal structures similarly seen in atomic assemblies. These artificial materials composed of nanoparticles have exhibited collective properties that are different from their bulk materials which can be seen as another dimension in the periodic table[23]. Methods of developing these structures can be done by evaporation-induced assembly during drop casting of unary nanoparticle [24] or a co-composite of binary nanoparticle[25] arrays. Despite this simple approach, an applicable fabrication of superlattices is difficult to manipulate due to the complexity of nanoscale forces among them. Therefore, better methods to manipulate the fabrication process is to utilize soft ligands (molecules, polymer or DNA). By doing so prevents the aggregation among nanoparticles and enables tunability of the lattice structure and interparticle distances[26].

The application space for superlattices is dependent on the type of nanoparticles used. For example, metallic nanoparticles such as gold nanoparticles[27] can have a broad

range of applications, from fundamental studies of light-matter interaction[28], optical metamaterials and substrates for surface enhanced spectroscopies, materials for plasmonic sensing, biodiagnostics[29], and photocatalysis. In the case of magnetic nanoparticles, there are multiferroic materials for memory and logic device applications[30].

Templated assembly

There are various methods to templated assembly and many require materials surfaces that are modified (chemical etching[31], lithographic patterning[32]) to established defined target sites to capture nanostructures. The templated assembly here will be utilizing liquid crystal as a host material[33]. The templated assembly type discussed here is of an assembly process that requires a host material, such as liquid crystal, and a guest material, such as nanoparticles, that can be templated to assemble into a superstructure provided certain conditions having been met. My work follows this kind of assembly. Nanoparticles are driven to specific arrangements following surface functionalization. In general, it is termed as a bottom-up process in that superstructures are constructed from (molecular / nanoparticle) constituents into larger (ordered/organized) structures, and this is typically seen in nature – such as the self-assembly of the lipid bilayer membrane for cells. Block copolymers are another material used in self-assembly process to create functional materials.

Shortcomings in current applications

The shortcoming in current applications that are primarily built from top-down assembly methods are primarily the lack of ability to tune properties (optical, electrical, etc. in situ due to rigid constraints and having less disorder in morphology that can arise in bottom-up assembly arising from static or dynamic deviations. The role of disorder in bottom-up assembly is important since they can result in interesting structures such as 3D architectures precise spatial control [34,35]. The produced assembled constituents can be manipulated postproduction. Phases where disorder can become ordered by changing temperature, i.e. liquid to crystalline phase for liquids or metals, isotropic to nematic for liquid crystal, and ordered-disordered transitions in block-copolymers[36].

The bottom-up assembly is inspired by nature, where a great number comes from biological systems. In the realm of drug delivery systems, the current assembly processes use complex synthesis methods involving polymers and co-block-copolymers, vesicles, and others that tend to necessitate the usage of laser exposure for release with times greater than 10 minutes.

It has been inherently difficult when engineering at lengths scales going down past the micro scale and increases costs. By utilizing a self-assembly process that is effective in the nano- and micro- scale, the systems can be designed to assemble into desired structures such as shells and magnetic semiconducting aggregates.

Nanoparticle cargo delivery systems

Nanostructured drug delivery systems (DDSs) aim for efficient transport and controlled release of drug molecules in the diseased tissue sites of living systems. The recent drug delivery systems can be divided into two major categories based on materials, organic and inorganic NPs. Polymeric (liposomes, vesicles[37]), Inorganic nanoparticles (silica[38], quantum dots[39] i.e. CdSe/ZnS, metal-organic frameworks [40] i.e. gold or silver, magnetic i.e. iron oxide). All of which have been used to study treatment of cancer and disease, and imaging. These nanocarriers come in different sizes, structures and surface properties. There are many obstacles for nanoparticles for clinical use in cancer [41–43] and disease treatment such as scaling up, toxicity and biodistribution, poor control over loading and releasing of drugs, and physiological barriers which others have studied and my work will cover.

Limitations of conventional DDSs has drawbacks such as the ones that you take orally for example, have limited effectiveness with variable absorption rate and break down before entering blood circulation due to insolubility, controllability and lacks selectivity [40]. The usage of nanoparticle-based drug delivery systems have brought to point the capability of improving therapeutic outcomes in treating diseases effectively with minimum side effects and addressing the drawbacks above. By altering surfaces of NPs, cellular uptake can be synergistically controlled on size dependence and cationic surface coverage [44].

In comparison to the self-assembled NPs geared towards tissue engineering and drug delivery, a few common platforms of such cargo release systems are AuNPs with smart polymers[45], silica-gold-core-shell composite NPs[46], AuNP-assembled nano-micelles and cross-linked nano-vesicles[47] to name a few. Various studies have shown that nanocarrier based drug delivery systems have improved or enhanced therapeutic efficacy in the treatment of various cancer therapies[40,43] and diseases [21,22]. These nano-based platforms account for various parameters that need to be addressed when considered for drug delivery and tissue engineering applications. The two primarily parameters are biocompatibility (nontoxic) and having a controllable release profile such as low optical input power (< 2 mw) resulting in less heating and safe for tissue and quick release times of less than 10 minutes [48].

Measures have been made to ensure biocompatibility with nanoparticle, whether they are polymer- organic-[49] or inorganic-based[50]. Some nanoparticles are surface functionalized (for hydrophilicity) for nano-bio surface interactions as well as ‘stealthy’ drug and targeted delivery on the surface while others use a cargo encapsulation and delivery platform[41,51,52]. Toxicities have been addressed by using nanoparticles that are non-toxic or have been made non-toxic by surface functionalization[53]. AuNPs that are less than 10 nm in size are more readily accepted by cells[54].

Despite the novel cargo release systems, the ones mentioned above had temporal release profiles of at least 10 minutes, optical input power greater than 2 mW, and the complexity of their multistep processes to synthesize them. My work focuses on a nanocarrier DDS based on a shell-like structure rather than vesicle based or specified targeting to cells. There are two drawbacks to the polymeric and vesicle DDSs, they are the multistep synthesis to create the system and the required long exposure time to light irradiation of excitation powers greater than 2.5 mW generating greater local temperature and time greater than 10 minutes. The ANSI Standard for laser exposure should be less than 2.5 mW and a maximum of 10 minutes of exposure. There are limitations in cellular uptake or cellular engulfment for nanosystems[55]. The largest size nanostructure in this work for example is 4 μm so the possible use of our nano-assembled shell system for growth factor or drug delivery is within the limits. The nanoparticle constituents that make up the nanosystem have a maximum size of 20 nm.

This work utilizes semiconducting nanocrystals also known as quantum dots and magnetic nanoparticles. The quantum dots and gold nanoparticles are surface functionalized to construct a spherical nanocarrier for cargo encapsulation in delivery applications and will address how surface functionalization, when designed, can minimize toxicity, enable charge transfer, and shell formation.

In this thesis, a directed self-assembly process in which thermodynamic forces drive the self-assembly and can be modulated is utilized. To form nano – micro size shells, the molecular surface ligands used not only stabilize but add functionality to our nanoparticles to form nano – micro sized shells with a liquid crystal phase transition to assist in assembly. Figure 1-1 below illustrates a proof of concept of a possible application space in tissue engineering.

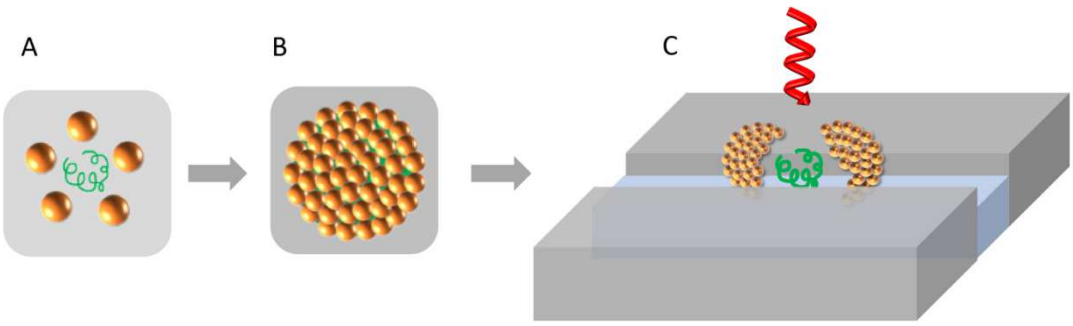

Figure 1-1 Schematic of nanoparticles assembled into a shell structure encapsulating drugs. A) functionalized nanoparticle and drug molecules dispersed in solution for encapsulation and assembly, B) nanoparticles with drugs encapsulated within, and C) Shell deposited in cell cultures and then ruptured to release drugs. Shell rupture to be designed to be actuated by electric potential or optical excitation in 540 nm wavelength.

Chapter 2 Experimental Methods

The techniques used to prepare and characterize samples in this dissertation are outlined in this chapter. This includes scientific principles, equipment, and procedures involved in each technique. Any variations from the techniques used here are specified in subsequent chapters.

2.1 Sample Preparation/Synthesis

The samples used in this work include colloidal CdSe/ZnS (CZ) quantum dots (QDs), Fe_3O_4 magnetic nanoparticles (MNPs), and gold (Au) nanoparticles (AuNPs) prepared in liquid crystal, 4-cyano-4'-pentylbiphenyl (5CB). CZ and MNPs were assembled together with 5CB. Surface functionalized CZ QDs were assembled into shell structures with three different ligand molecules, bis(imino)pyridine (BIP) – BIP-H, BIP-Me, and BIP-iPr.

Surface functionalized CZ QDs were prepared on indium tin oxide (ITO)-coated glass substrates and semiconducting zinc oxide (ZnO) single crystals from (MTI Corporation) for spectroscopic measurements. ITO glass substrates were cut from a large substrate in 15 mm x 15 mm pieces using a diamond cutter and a metal ruler to ensure straight edges. The conductive side was identified with a multimeter and the non-conductive side is marked to allow identification of sample side during measurements. ZnO substrates were purchased as 5 mm x 5 mm sizes with conductive size identified by edge markings. Shell structures were deposited on transmission electron microscopy grids to locate shells within grids during scanning electron microscopy measurements.

2.2 Ligand Exchange

Nanoparticle ligand exchange allows for nanoparticles to be functional in a way that they can interact with other molecules such as sensing, becoming biocompatible, or creating superstructures. ODA-capped CdSe/ZnS QDs CZ640 were purchased from NN-Labs. CZ640 QDs have a core diameter of 4.8 nm (5–10% size inhomogeneity). Their surfaces were modified using bis(imino)pyridine. Surface exchange was carried out under inert conditions by adding the QDs to a hexane solution containing an excess of the modifying ligands relative to the native ODA. This solution is incubated for at least 5 min and then purified with acetonitrile (MeCN) and chloroform ($CHCl_3$). The QDs are then separated by centrifugation and redispersed in toluene.

2.3 Characterization

2.3.1 Dynamic Light Scattering (DLS)

Dynamic Light scattering (DLS) is a method to determine the size of submicron particles by measuring their thermal motion (diffusion) in suspensions and emulsions. The intensity of scattered light is recorded for some time interval and by analyzing the auto correlation function, the size and diffusion coefficient can be determined. DLS was used for the characterization of very diluted suspensions of nano-assembled nanoparticles into primarily shell structures. The sizes of nanoparticles with three different ligand molecules that functionalize the surface were characterized.

2.3.2 Photoluminescence Spectroscopy

Employment of optical characterization on materials is a powerful method for extracting useful information regarding semiconductor material, such as electronic band gap, free electrons and holes, and energy transfer mechanisms. It offers a non-invasive and simple sample preparation in acquiring information and evaluating sample performance or interface characterization. Photoluminescence is a valid optical characterization method to characterize the optical properties of CZ QDs that have been surface modified molecularly and when assembled into clusters or shells. A schematic of the optical set up is shown in Figure 2-1.

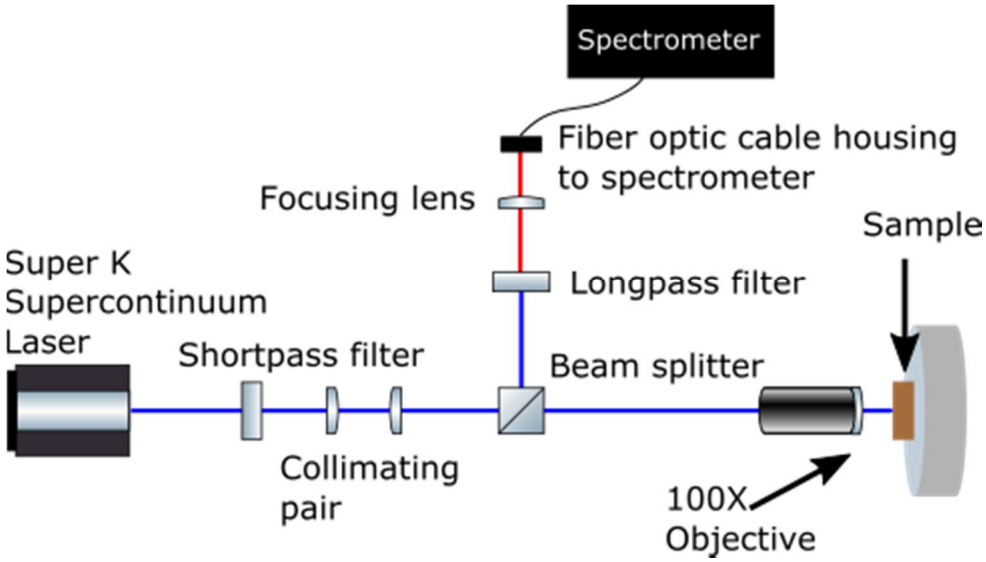

Figure 2-1 Fluorescence microscope in reflection geometry

2.3.3 Scanning Photoluminescence

Scanning photoluminescence spectroscopy is used to collect spectroscopic data to generate a high-resolution photoluminescence map of a sample. This method provides useful information of the sample, such as density of quantum dots on a specific area interpreted by the variations in the intensity and wavelength of the photoluminescence spectra. The resolution of the measurement is diffraction limited to the wavelength of the excitation laser, which is chosen to be a shorter wavelength, in this case 409 or 430 nm, to get the highest achievable resolution. A schematic of the optical setup is shown in Figure 2-2.

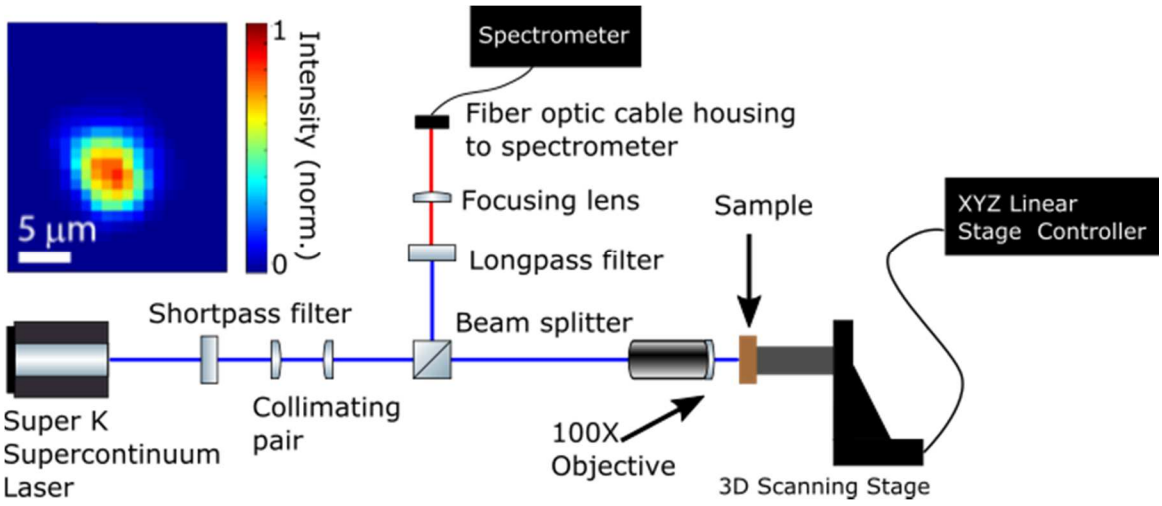

Figure 2-2 Optical setup for scanning photoluminescence spectroscopy. Map of peak wavelength for a MNP and QD cluster acquired from this setup as inset.

A sample is mounted on the 3D scanning stage with Newport's MFA-PPD with minimum step size resolution of 100 nm and ability to raster scan the laser's excitation across a designated sample area. A repository of spectra collected by the spectrometer at each excitation spot is acquired by a LabView program and analyzed with MATLAB to generated maps of photoluminescence intensity and emission wavelength as shown in the top left of Figure 2-2.

2.3.4 Time Resolved Photoluminescence (TRPL)

Time resolved photoluminescence is a technique used in optical spectroscopy to obtain the time-dependent profile of light emitted from a sample following excitation. Time dependent numerical values of the photoluminescence emission lifetime of a fluorophore, or electron-hole recombination lifetime in semiconductors may be obtained. To obtain

lifetime measurements, a time-correlated single photon counting electronics are used. A pulsed laser to excite the sample periodically, a single photon avalanche diode (SPAD) for data acquisition, optics to filter excitation light and pass emission, and electronics to designate the repetitive times of excitation and collection of photons. With the above equipment, the data can be used to construct the emission decay profile which appears as a histogram of photon counts against time in nanoseconds to microseconds[56]. An illustration of this process is shown in Figure 2-3 below.

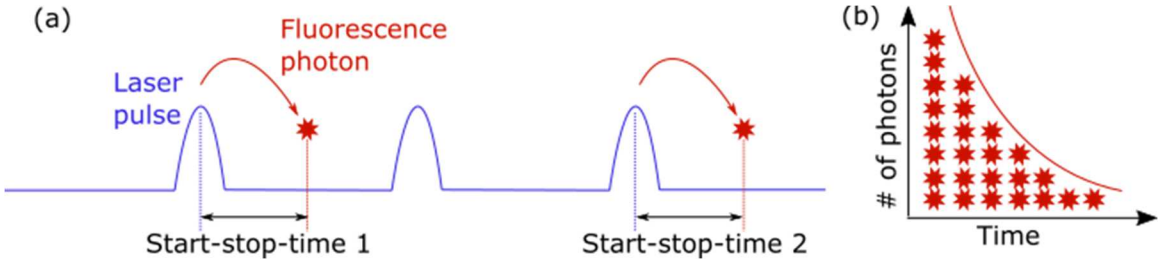

Figure 2-3 (a) Laser pulse showing the start time and top time at the detected photon. (b) An accumulation of start-stop times constructs the histogram.

The emission decay is exponential and can be explained by the probability of an excited molecules having 50% probability of returning to ground state after the first nanosecond post-excitation, having the remaining population of 50% in the excited state. The process is iterated over time, collecting the number of photons at each time representing the intensity and is proportional to the population of excited molecules. As the excited population of molecules over time go back to the ground state, the intensity decreases to zero[56].

Experimentally, the measurements are done with electrical synchronization by recording the time difference between the excitation pulse and photon emission, by referencing former with a time-correlated single photon counting (TCSPC) system and detecting the latter with a SPAD. With the collected signals, and fast electronics to perform digital timing, the histogram can be populated[56]. The optical setup for this measurement is shown below in Figure 2-4.

Here, a bi-exponential decay function[57] to determine the average lifetime of the surface functionalized quantum dots. Lifetime measurements are indispensable tool for characterization of any materials and interface.

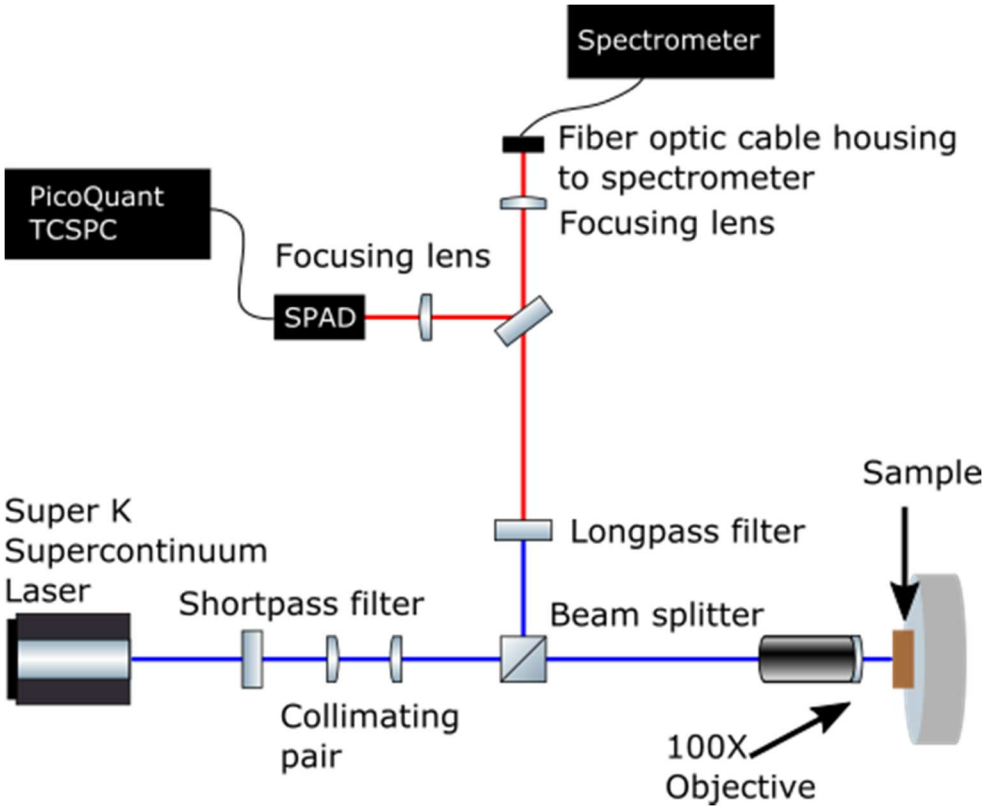

Figure 2-4 TCSPC optical schematic setup

2.3.5 Magneto-Optical Kerr Effect (MOKE) Spectroscopy

Magneto-optics (MO) refer to all activities that involve the interactions with an incident light (electromagnetic radiation) with magnetized material. The magneto-optical Kerr effect (MOKE) is the rotation of polarization or change of intensity of an electromagnetic wave reflected from a magnetized sample[58]. Not to be confused with one of the first MO effects discovered, the Faraday effect which are the same changes but through a material magnetized material[59]. MOKE has been utilized to investigate

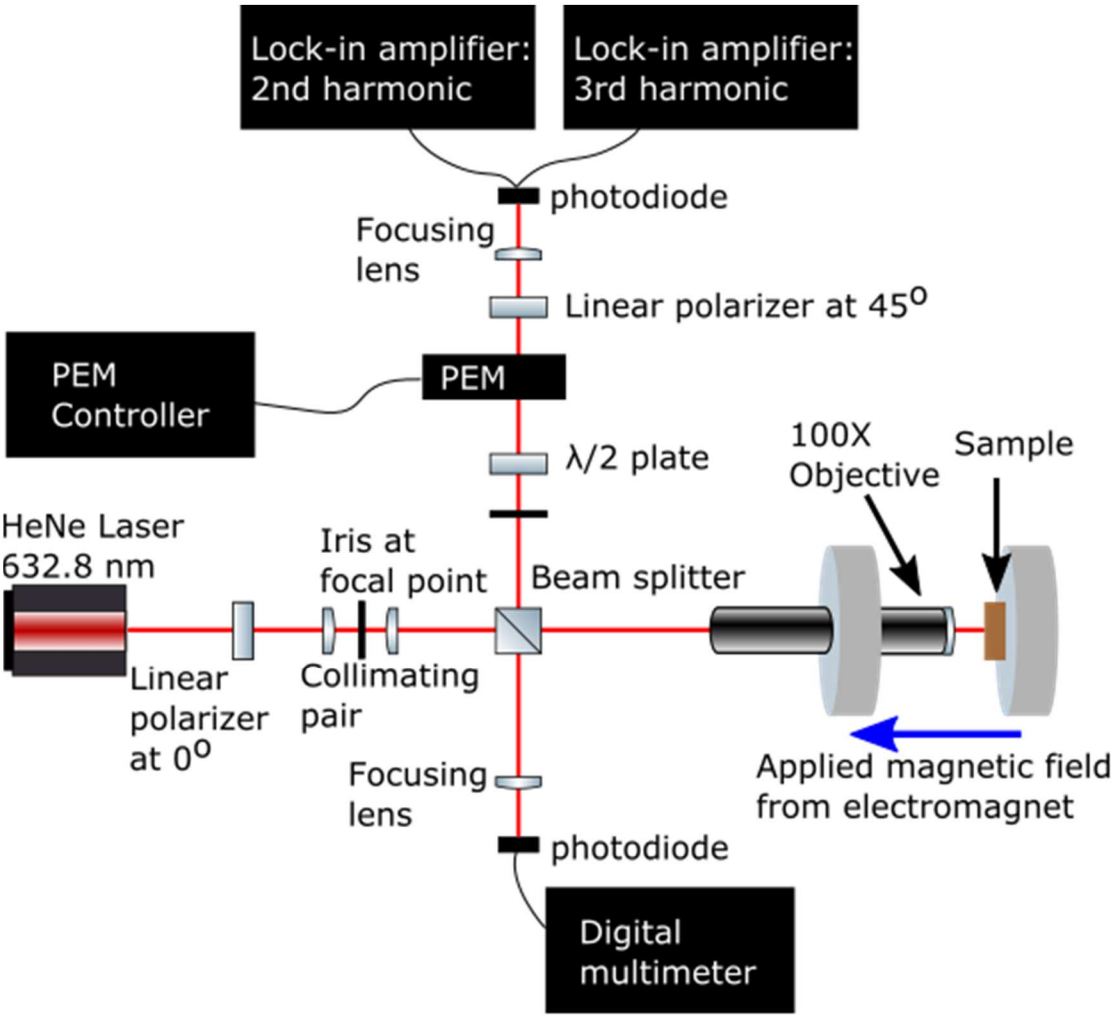

Figure 2-5 Experimental setup for polar MOKE spectroscopy. In this geometry, light is at normal incidence to the sample, which is magnetized perpendicular to the sample surface. The Kerr rotation and ellipticity are proportional to the magnetization of the sample.

magnetization of thin samples containing liquid crystal 5CB, and co-self-assembled Fe_3O_4 and CZ quantum dots. Materials that have demonstrated MO effects have been applied in

various applications such as optical devices (waveguiding)[60], data storage (especially)[61], magneto-sensors, and others. The setup for this measurement is depicted in Figure 2-5.

In reference to Figure 2-5, the laser beam is polarized with a linear polarizer and collimated through a collimating pair to come into contact with the magnetized sample and splitting at our beam splitter through to the l/2 wave plate, photo-elastic modulator (PEM), second linear polarizer (analyzer), and finally the photodiode connected to lock-in amplifiers to collect data into a computer. The data is then calculated for Kerr rotation (q_k) and Kerr ellipticity (j_K).

There are three main configurable geometries in which we can observe MOKE signal: polar (PMOKE), longitudinal (LMOKE), and transverse (TMOKE). Here, we focus on PMOKE spectroscopy which has the configuration of the magnetic field perpendicular to the sample plane and parallel to the light's plane of incidence as shown in Figure 2.6.

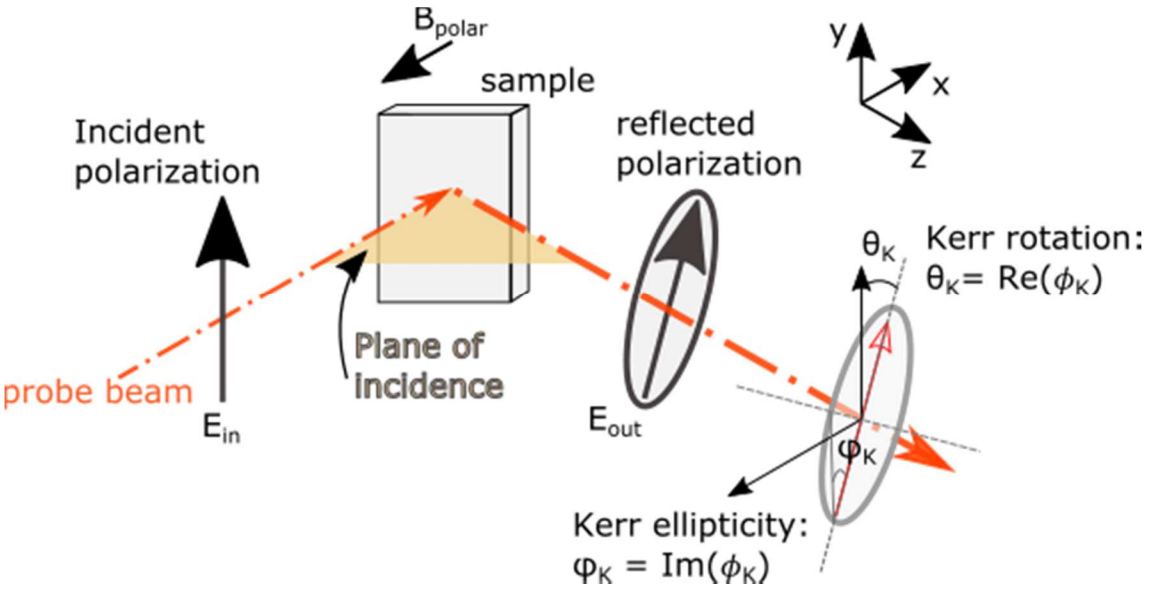

Figure 2-6 Magneto-optical Kerr effect illustration. In this case the applied magnetic field B_{polar} is perpendicular to the plane of the sample surface and parallel to the plane of incidence, which is the polar MOKE geometry. Additionally, a geometrical representation of the complex Kerr angle ϕ_K. $Re(\phi_K)$ relates to the ellipse's major axis and Kerr ellipticity $Im(\phi_K)$ relates to the minor to major axis ratio.

To obtain Kerr rotation ($Re(\phi_K)$) and Kerr ellipticity ($Im(\phi_K)$) experimentally, the complex Kerr angle (ϕ_K) is expressed in terms of the complex refractive index for the left

circularly polarized (LCP) light ($\tilde{n}_+$) and right circularly polarized (RCP) light ($\tilde{n}_-$) components of linearly polarized light. The complex index of refraction is given by $\tilde{n}_\pm = n_\pm + k_\pm$ and the complex Kerr angle is given by [58]:

$$\phi_K \cong tan\phi_K = \frac{i2(\tilde{n}_- - \tilde{n}_+)}{1-\varepsilon} = \frac{2}{1-\varepsilon}[-(k_- - k_+) + i(n_- - n_+)] \quad \text{Eq. 2.1}$$

From the above expression of Eq. 2.1, $(Re(\phi_K))$ refers to circular dichroism given by $(k_- - k_+)$, and $(Im(\phi_K))$ refers to the circular birefringence $(n_- - n_+)$ with the assumption that the imaginary component of tensional permittivity, ε, is small compared to 1.

To measure both the real and imaginary parts of the Kerr angle, the PEM is necessary. A lock-in amplifier matches the frequency at which the PEM is set to ignoring other signals, locking in the signals generated by the PEM when affecting the Kerr signal. The PEM is designed with an optically isotropic crystal and two piezoelectric transducers that create stress alternations at a resonant frequency (ω_{PEM}) set at 50 kHz. With the optical head driven by the resonant frequency, large swings in the strain in the horizontal direction creates significant swings in the index of refraction. The index refraction in the x-direction $n_x(t)$ varies as:

$$n_x(t) = n_0 + \Delta n \cdot sin(\omega_{PEM}) \quad \text{Eq. 2.2}$$

and in the y-direction $n_y(t)$ remains constant equal to n_0, the unstrained index of refraction. The term, Δn refers to the difference in refractive index produced at the peak of the strain oscillations. The oscillations in the x-component of the electric field experiences a time dependent periodical phase modulation $\delta(t)$ with respect to the y-component given by[58]:

$$\delta(t) = \beta \cdot cos(\omega_{PEM}t) \quad \text{Eq. 2.3}$$

where β is the phase modulation amplitude, also known as the retardance, describing how far one linear polarization is shifted from the other and is expressed as[58]:

$$\beta = 2\pi\frac{\Delta L}{\lambda} = 2\pi\frac{\Delta nD}{\lambda} \quad \text{Eq. 2.4}$$

where ΔL is the effective optical path difference for x and y polarized radiation due to Δn (the maxiumum difference between n_x and n_y), D is the thickness of the PEM crystal, and λ is the wavelength of light. In this setup, the optical axis of the PEM is parallel to the y-component of light and we see variations in the x-component of polarization due to the Kerr rotation or ellipticity.

Prior to measuring the Kerr rotation or ellipticity, a calibration of the PEM is done to set the retardance with the wavelength used. Differing from the setup in Figure 2-5 Experimental setup for polar MOKE spectroscopy. In this geometry, light is at normal

incidence to the sample, which is magnetized perpendicular to the sample surface. The Kerr rotation and ellipticity are proportional to the magnetization of the sample., the PEM is set at 45° between two cross polarizers at 90° of each other, blocking any light from reaching a detector when the PEM is off (retardance is zero). When the retardance on the PEM oscillates close to half-wave, the transmitted light intensity is at maximum. Minor adjustments may be made to the PEM device or optical setup for signal sensitivity.

After propagating through the PEM, the initial electric field E_0 has components along the PEM's x-axis and y-axis and experiences a phase shift where the transmitted electric field (E_1) is given by Eq. 2.5[58]:

$$E_1 = (E_0 cos45)\hat{x} - \left(E_0 e^{i\delta(t)} sin45\right)\hat{y} = E_0 \frac{\sqrt{2}}{2}\left(\hat{x} - e^{i\delta(t)}\hat{y}\right) \quad \text{Eq. 2.5}$$

The transmitted field E_1 is then projected onto the second polarizer, allowing only components parallel to its axis through, where the transmitted field E_2 is given by Eq. 2.6:

$$E_2 = E_0 \frac{\sqrt{2}}{2}\left(1 - e^{i\delta(t)}\right) \quad \text{Eq. 2.6}$$

Giving a resulting intensity of I_2 given by Eq. 2.7,that is sensed by a detector with magnitude E_2^2:

$$I_2 = \frac{1}{2} c\varepsilon_0 |E_2^2| = I_0(1 - 1cos[\beta cos(\omega_{PEM} t)]) \quad \text{Eq. 2.7}$$

Note that the signal is dependent on the last term, a cosine of a cosine, that may be expanded of even harmonics of ω_{PEM} in a Fourier series given by Eq. 2.8:

$$cos[\beta cos(\omega_{PEM} t)] = J_0(\beta) + 2J_2(\beta)\cos(2\omega_{PEM} t) + 2J_4(\beta)\cos(4\omega_{PEM}) + \cdots \quad \text{Eq. 2.8}$$

where J_n are the n[th] order Bessel functions.

Finally, the signal at the detector can be calculated and see the relationship between the complex Kerr angle and the ratio of the signal at the detector with equations Eq. 2.9 and Eq. 2.10:

$$Re[\phi_K] = \frac{1}{4J_2(\beta)} \frac{I_{2\omega_{PEM}}}{I_0} \propto I_{2\omega_{PEM}} \quad \text{Eq. 2.9}$$

$$Im[\phi_K] = \frac{1}{4J_3(\beta)} \frac{I_{3\omega_{PEM}}}{I_0} \propto I_{3\omega_{PEM}} \quad \text{Eq. 2.10}$$

Note that $I_{n\omega_{PEM}}$ represents the signal intensity at the n[th] harmonic of ω_{PEM},and I_0 is the signal intensity at the frequency of ω_{PEM}. The Kerr rotation, Eq. 2.9, is associated with even harmonics, whereas the Kerr ellipticity, Eq. 2.10 associates with odd harmonics. The frequency is referenced from the PEM to two lock-in amplifiers, one for each harmonic,

both of which are connected to the photodiode detector illustrated in Figure 2-5. The signals detected from the lock-in amplifiers are used in calculation with a LabVIEW program along with applied magnetic fields in polar geometry. The magnetic field is applied in polar geometry via an electromagnet with currents ranging from -5 to 5 A. The current may be converted to an applied magnetic field using the following expression:

$$H_{applied}(G) = 13.143 - 1238.769I - 0.301I^2 + 2.572I^3 + 0.047I^4 \quad \text{Eq. 2.11}$$

where I represents the current in Amperes for the electromagnet. The expression is for a magnetic field with configuration of 1 pole. After collecting data at various currents, the program plots the curves for Kerr rotation and ellipticity as a function of current.

The rotation in polarization of incident s-polarized light after being reflected from the thin sample of 5CB and co-assembled Fe_3O_4 and CZ QDs can then be observed. What we detect in measuring MOKE, is how the incident p-polarized light becomes elliptically polarized after reflection. The incident light's polarization changes and is what is measured. We observed MOKE in this work when magnetic nanoparticles and quantum dot clusters were assembled in liquid crystal. By having these clusters in LC, we reduce the Fréedericksz transition threshold of the LC and is observed by MOKE.

2.3.6 Scanning Electron Microscopy

Scanning electron microscopy (SEM) is used to extract topographical and elemental information about a sample at much higher resolution than that of optical microscopy by utilizing electrons for imaging instead of photons. With a much smaller wavelength, magnification can reach 100,000X or nm scale. Operation is based on a focused electron beam which scans the sample surface and results in secondary electrons, backscattered electrons, and characteristic x-rays being able to be detected by different detectors to create images of the sample that are digitally converted to an image[62,63]. Secondary electrons are a result of inelastic interactions between the incoming electrons and the sample and produce topographical images of the sample[63]. Backscatter electrons are due to elastic collisions of the incident electrons with the atoms of the sample, increasing the number of backscatter electrons as the atomic number of the element increases, and can deduce elemental information of the sample in addition to topographical information[63].

2.3.7 Transmission Electron Microscopy

Transmission electron microscopy (TEM) is another electron-based technique that I used to measure the distance average between surface functionalized nanoparticles. I used this to get images at the nanoscale with high resolution. TEM images were obtained with the JEOL-2010 TEM equipped with a LaB6 filament and operated at 200 kV in the Imaging and Microscopy Facility at UC Merced. TEM samples were prepared by depositing 2.5 mL

of solvated sampled on a TEM copper grid with carbon film (300 mesh, Ted Pella, Inc.) then removing excess solvent by placing in heating oven at 40 ^{o}C for 1 hour.

Chapter 3 Directed assembly of magnetic and semiconducting nanoparticles with tunable and synergistic functionality

This chapter studies the photoluminescence (PL) enhancement of co-dispersed CdSe/ZnS quantum dots and Fe_3O_4 magnetic nanoparticles by applied magnetic fields < 250 mT. The study involves spectroscopic, magneto Kerr effects, and electron microscopy to investigate the PL enhancement of the co-dispersed nanoparticles in nematic LC. The effect is reversible in co-assemblies with 5 and 10 nm MNPs but demonstrates hysteresis in those with 20 nm MNPs. Transmission electron microscopy (TEM) and energy dispersive spectroscopy reveal that QDs are densely packed into the center of the co-assemblies while the MNPs are relatively uniformly dispersed throughout the cluster volume. Lorentz TEM allowed for the observation of MNPs suspended in LC rotating to align with applied magnetic fields which were determined to be the cause for the observed PL increase at the micro-scale.

3.1 Introduction

The unique size-dependent properties of semiconducting, metallic and magnetic nanomaterials are currently leveraged in a wide variety of applications, ranging from opto-electronics (lasers[64–66], light-emitting diodes[67–69], photovoltaic devices[70–75], and photodetectors[76–78]) to biological and biomedical (drug delivery platforms[46,47,79–81], biochemical sensors[82–85], theranostics[86], and tissue engineering[87]). Since ensembles of nanoparticles (NPs) behave very distinctly from both individual NPs and their bulk counterparts, another exciting research avenue is the fabrication of 'superlattices' (SLs)[88–91]. SLs are artificial materials composed from NPs, where NPs are analogous to atoms in naturally occurring crystalline materials. The possibilities that open up via these efforts are endlessly intriguing. Designer characteristics and complex, multifunctional capabilities, beyond the scope of natural materials, could become a reality, with the added layer of utility of having tunable properties. The earliest approach to fabricating SLs consisted of bottom-up techniques[88], where self-assembly was used to drive the formation of energetically optimized crystalline symmetries. This route was quite successful in developing planar structures that included not only elemental SLs, but binary and ternary ones[92], with the latter two extending to compositionally varied NPs in a single SL. Top down lithographic techniques have also been applied to produce SL structures[93], but these are better suited to studying the fundamental aspects of inter-particle interactions and less amenable to scaling up into realistic macro- or meso-scale materials.

An alternate route is templated assembly, where NPs are driven to specific arrangements following surface functionalization[94–96]. The most successful surfactant has been single stranded DNA[94], which uses the base-pair complementarity to organize NPs with high spatial precision. Also included, are the use of polymers and liquid crystal materials[97] having several advantages. They allow synthesis of nano-assemblies in non-planar geometries, extending to three-dimensions; the variation in the types of constituent NPs has greater versatility; and finally, they offer the possibility of designing controllable composite materials that could be tunable in situ in response to external stimuli, such as electromagnetic fields, temperature and strain. The only issue is that most templated techniques do not lead to long range crystalline order. However, there are many instances of amorphous materials performing adequately, or even surpassing, their crystalline counterparts. Amorphous silicon (a-Si)[98] is one such example, where although the overall power conversion efficiency is lower than crystalline silicon solar cells. Amorphous diamond[99] synthesized in a laboratory, is another example, and has shown indications of being structurally harder than its crystalline counterpart. From a more fundamental perspective amorphous molybdenum silicide (MoSi)[100] not only demonstrates superconductivity but has a critical temperature higher than the crystalline sample. And finally, there is the example of ferrofluids[101] that possess ferromagnetic order without any crystalline structure. Taken together, it appears crystalline structure is not necessarily a must in order to achieve a desired functionality. As long as there is short-range order and uniform, controllable and predictable interparticle interactions, an amorphous arrangement of NPs can suffice. Further, not requiring perfect long-range order will make the scalability aspect far more realistically achievable, extending these assemblies to the meso- and macroscopic regimes.

Here, we investigate the formation and modulation of co-assemblies of Fe_3O_4 magnetic nanoparticles (MNPs) and CdSe/ZnS core/shell quantum dots (QDs), directed by the thermotropic phase transition of a liquid crystalline (LC) material. This study builds on a prior effort by our group[102], where the formation of these co-assemblies were observed and demonstrated that a small magnetic field could be used to enhance QDs PL, up to almost three-fold. Simultaneously, the co-assemblies appeared to spatially compress, and from this we indirectly inferred that the clustering of the MNPs produced localized high fields that caused LC re-orientation at low external magnetic fields. This re-arrangement produced compaction of the clusters, resulting in the detection of increased QD emission. Without the benefit of direct imaging, the mechanism driving this spatial compaction, and the exact role of the magnetic field in the process remained speculative. This study presents an investigation of the fundamental mechanism driving the synergistic effect using a combination of high-resolution structural, spectral and magnetic contrast imaging at multiple length scales from a few microns to ~10 nm. At the nanoscale, transmission electron microscopy (TEM) in conjunction with energy dispersive spectroscopy (EDS) to correlate NP composition with spatial distribution and discover that while the MNPs maintain an equitable distribution within the assembly, the QDs close pack at the center.

When a magnetic field is applied to an ensemble of MNPs dispersed in LC, transmission electron aberration-corrected microscopy (TEAM) imaging in Lorentz mode (L-TEAM, with an applied magnetic field) shows that the MNPs re-orient in the field in a way that increases the diffraction intensity. This rotation is absent when the MNPs are deposited directly on to a TEM grid without the LC medium, but persists in the micro-scale co-assemblies, as confirmed by magneto-optical spectroscopy and confocal photoluminescence (PL) microscopy measurements. Data from the latter demonstrates that magnetic field-driven emission enhancement from the QDs in the co-assemblies occurs irrespective of the size of the MNPs but is not completely reversible when large 20 nm MNPs are used. Further, the alignment of the LC molecules hosting the QDs and MNPs have markedly different manifestations in terms of the pattern in PL spectroscopy. When the LC molecules are homeotropically aligned (director axis perpendicular to sample plane) in the nematic phase, as was the case in our prior study, the PL enhancement occurs at the center of the assembly. This increase in intensity is reversible for 5 and 10 nm MNPs but demonstrates hysteresis when using 20 nm ones. At planar orientation of the LC molecules (director axis in the sample plane), QD PL enhancement begins along the edge of the assemblies, creating a ring pattern for applied fields $B < 120$ mT, and encompassing the entire assembly as the field is further increased.

3.2 Results and Discussion

3.2.1 Imaging-based characterization

The formation of the co-assemblies is directed by the phase transition of the nematic liquid crystal (LC) material[33,102]. This method of directed assembly was developed in our group, using phase transition templating to form micro- to meso-scale arrays of NPs. Despite the lack of translational order, the NPs organize in assemblies in a fractal-like manner, maintaining a uniform inter-particle separation throughout. This shows up not only as a structural metric in small angle x-ray scattering measurements[102] but is reflected in the functionality as well. For example, in homogenous assemblies of QDs only, the spectral emission energy is constant throughout a several micron-sized array, indicating the equanimity of inter-QD coupling[33]. The LC used here is popularly known as 5CB (4′-Pentyl-4-biphenylcarbonitrile), and has a nematic-to-isotropic phase transition at 35 °C. Both types of nanomaterials, QDs and

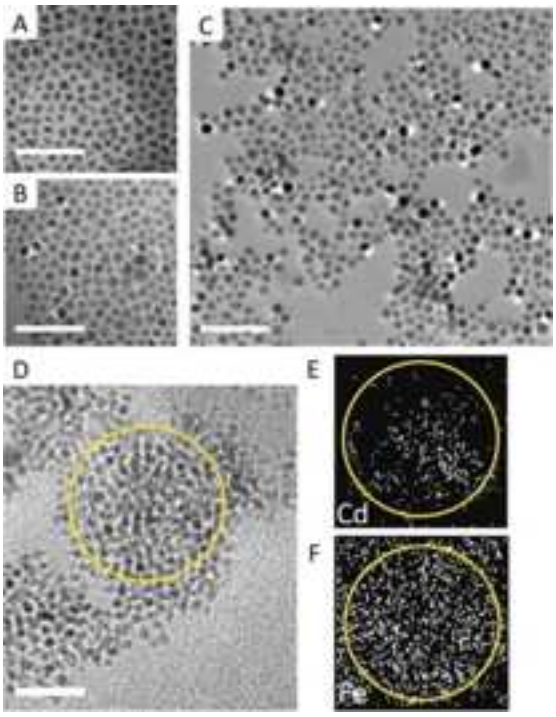

Figure 3-1 Transmission electron microscopy (TEM) images of (A) drop cast CdSe/ZnS QD layer, (B) drop cast Fe3O4 MNP layer and (C,D) QD-MNP dispersion in nematic liquid crystal (LC). Unlike the images in A and B, dispersion in LC produces a non-uniform layer due to the nematic phase-induced assembly. Energy dispersive spectroscopy (EDS) in the region of interest circled in D is mapped for (E) Cd and (F) Fe, which indicates that while the QDs are confined to specific locations, the MNPs remain well-dispersed. All scale bars: 50 nm.

MNPs, are dispersed in the isotropic LC at 40 °C. This mixture is then controllably cooled to allow the assemblies to form.

Figure 3-1 highlights the nano-scale organization of the QDs and MNPs, comparing dry drop-cast films with assemblies within the LC. Figure 3-1 A,B are TEM images of QD and MNP monolayers assembled via drop-casting followed by evaporation of the native solvent. This method tends to form homogenous arrays, as shown. Figure 3-1 C is a TEM image of QD-MNP dispersion in 5CB, at 25 °C, where the LC is in the nematic phase with planar orientation, and the proportions of the nanoparticles are 0.02% wt. of QDs and 0.04% wt. MNPs. The image seems to re-affirm the arrangement of NPs we have observed in earlier works, where the inter-particle separation remains relatively uniform throughout the assembly. This fractal-type organization of QDs and MNPs is independent of the LC alignment and MNP size Figure 3-2. But TEM images cannot unequivocally identify how the two different types of NPs are distributed within an assembly. Therefore, we use energy dispersive spectroscopy (EDS) in conjunction with TEM.

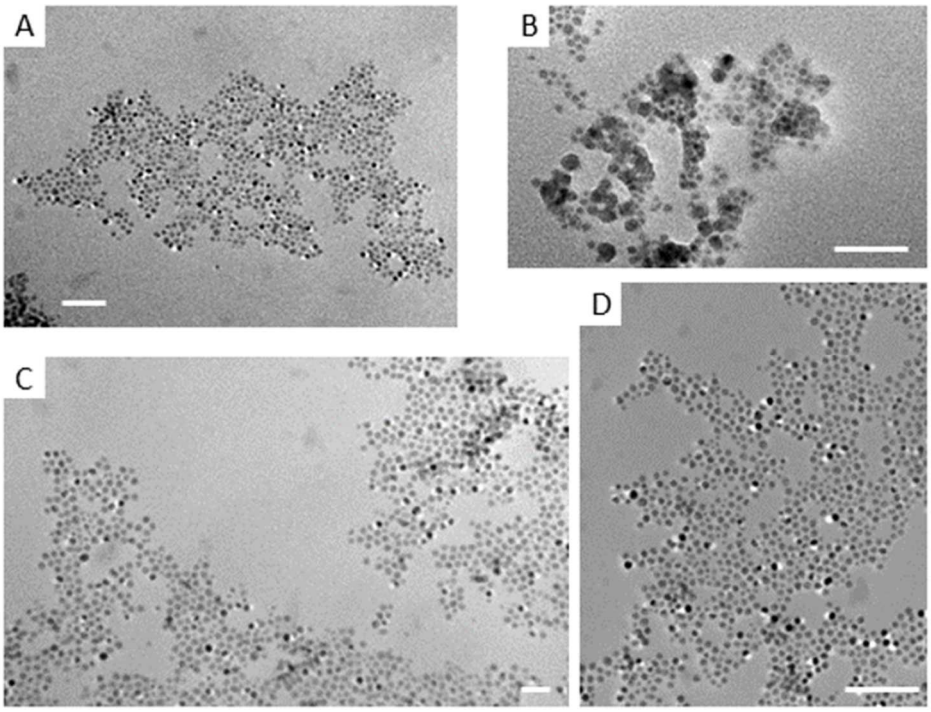

Figure 3-2 TEM images of co-assemblies QDs with (A) 10 nm MNPs with homeotropic LC alignment (B) 20 nm MNP with homeotropic LC alignment (C) 5 nm MNPs with homeotropic LC alignment (D) 5 nm MNPs with planar LC alignment. All scale bars: 50 nm.

Figure 3-1 D shows a TEM image of an area of the co-assembly with a region of interest marked out for which the corresponding EDS data is shown in Figure 3-1E,F. Following the elemental signatures, we see that the MNPs are present everywhere within the assembly, whereas the QDs are more densely packed closer to the center. It has been observed in prior works[103–106] that MNPs tend to aggregate at ~0.05 wt.% unless their surfaces are modified with mesogenic ligands. The highest fraction of MNPs we use is 0.04 wt.%, below this threshold, which may explain why the MNPs are not prone to as much aggregation as the QDs.

Figure 3-3 focuses on the effect of an applied magnetic field on the MNPs alone, with and without dispersion in the LC. Figure 3-3 A,B are L-TEAM images of a drop-cast layer of MNPs obtained with $B = 0$ and 100 mT, respectively, applied in situ perpendicular to the sample plane. Comparing these two images, we observe that the application of 100 mT causes some of the MNPs to appear darker (one is highlighted with a yellow arrow), while at the same time, some appear brighter (white arrow). In Figure 3-3 C,D the same procedure is demonstrated in a sample where MNPs are dispersed in LC, where the nematic phase did not have any intentional alignment. A visual inspection suggests that several MNPs in this case show increased scattering intensity when $B > 0$ and there are

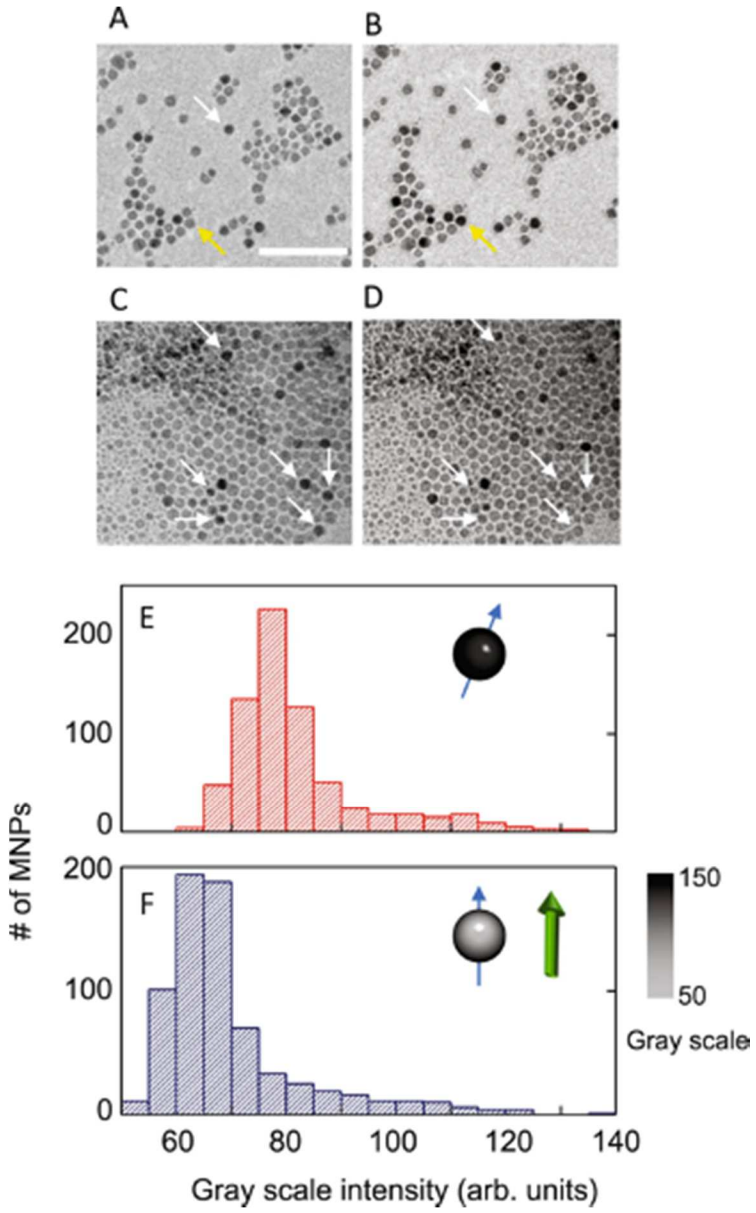

Figure 3-3 Lorentz TEM on drop cast 10 nm MNPs with (A) 0 and (B) 100 mT applied magnetic field. White arrow demarcates MNP whose scattering intensity decreases on the application of the magnetic field, and yellow arrow highlights the MNPs where the intensity intensity increases. Scale bar: 100 nm. Similar imaging on MNPs dispersed in nematic LC with (C) 0 and (D) 100 mT field. The LC phase does not have an intentional alignment. Between C and D there are negligible MNPs whose scattering intensity increases, as the numerous white arrows indicate. Analysis of C and D TEM images plotting histograms of scattering intensity of MNPs in (E) for 0 field and (F) 100 mT applied field. The schematics in the inset represent a single MNP with its Bragg angle shown as a blue arrow. The direction of the applied field is shown by the green arrow.

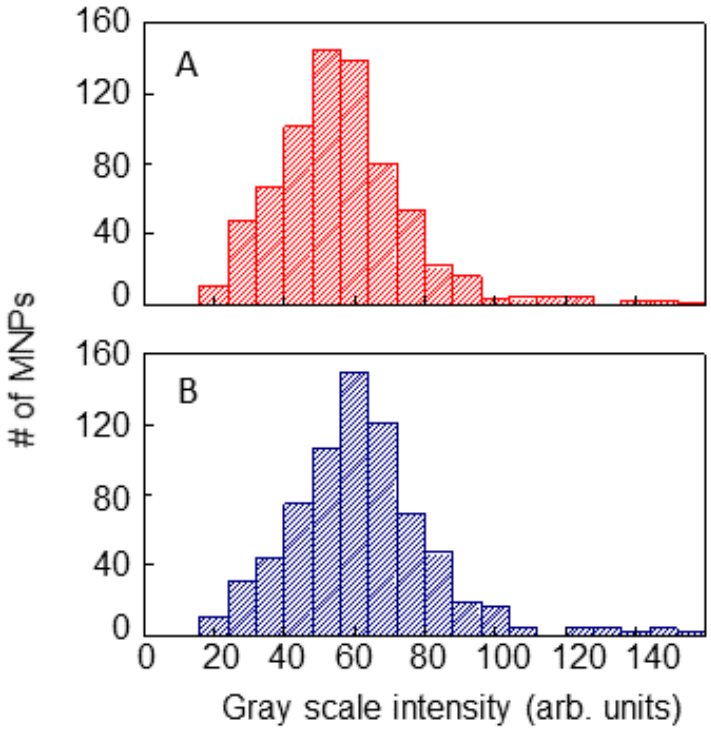

Figure 3-4 Analysis of TEM images of 10 nm MNPs drop-casted on to TEM grids without any LC. Histograms of scattering intensity of MNPs in (A) 0 field and (B) 100 mT applied field demonstrate that without the presence of LC, the average scattering intensity (and consequently MNP orientation) shows no variation of the extent observed with MNPs in LC.

almost none in this comparison that changes the other way. A quantitative analysis of the scattering difference with B for the MNPs in LC was done using ImageJ. The images were segmented into individual nanoparticles using standard thresholding and clustering, and the average gray scale intensity of each nanoparticle was calculated. Histograms representing this analysis are shown in Figure 3-3 E,F. There is a distinct shift to the lighter side of the gray scale, signifying an increase in overall scattering intensity with the application of the magnetic field. This implies that a portion of the MNPs rotate such that their Bragg angles align along B, but this is only observed when the MNPs are dispersed in LC. For the sample images in Figure 3-3 A,B, there are some stochastic changes in scattering intensity, but when averaged over large areas, no net change is discerned Figure 3-4.

3.2.2 Spectroscopy-based characterization

In the first set of spectroscopic measurements, we focus on the co-assemblies similar to those from our prior study, where the LC is aligned homeotropically, except that here we enlarge the phase space to include MNPs of 5, 10, and 20 nm diameters.

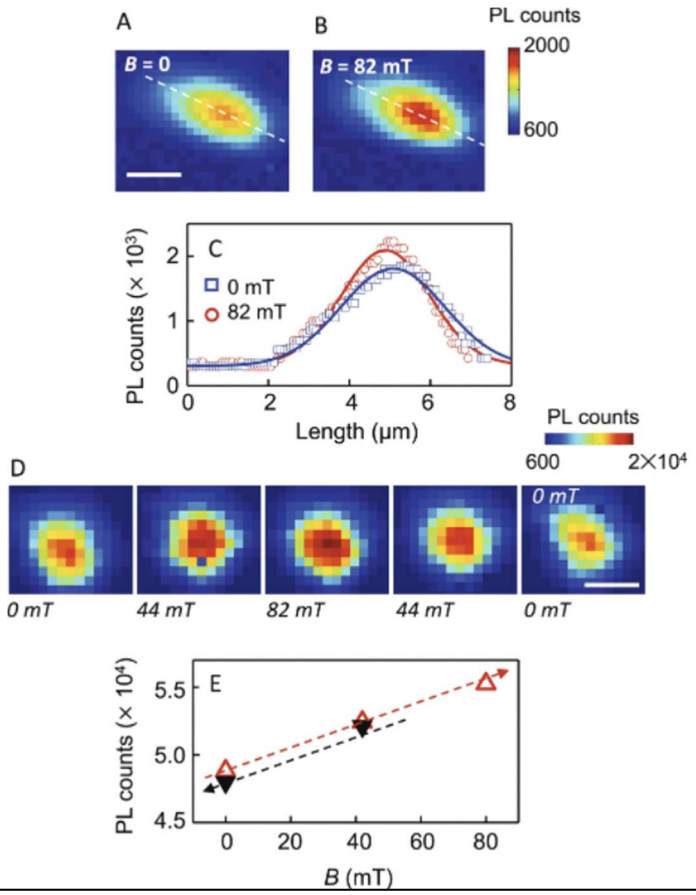

Figure 3-5 PL maps of a co-assembly with 5 nm MNPs at (A) 0 field and (B) 82 mT. (C) PL counts along the line cuts of A and B. (D) PL intensity maps as magnetic field is increased and then decreased with 5 nm MNPs. (E) Spatially-integrated PL intensities from the maps as a function of applied magnetic field. Arrows indicate the direction of magnetic field change. Scale bar: 6 μm.

Figure 3-5 highlights PL data from co-assemblies of QDs and 5 nm MNPs. Comparison of the spatially-resolved PL maps in Figure 3.5A,B show a small enhancement ~33% with B = 82 mT, applied perpendicular to the sample plane, along the LC director axis. Line-cuts across the PL maps along the dashed lines are plotted in Figure *3-5*C which confirms the small increase. A similar increment around the center is seen in the series of PL maps of co-assemblies with 10 nm MNPs as well. PL maps in Figure *3-5*D, and the integrated PL intensity of these maps in Figure *3-5*E, as B is ramped up and down show that the intensity changes are linear and almost entirely reversible for the 5 nm MNP co-assemblies

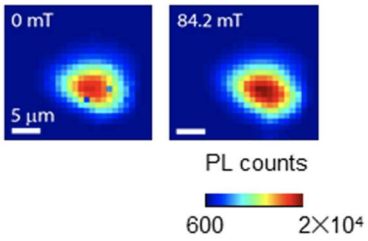

Figure 3-6 PL maps of a co-assembly of 10 nm MNPs at 0 field and 82 mT with homeotropic LC alignment.

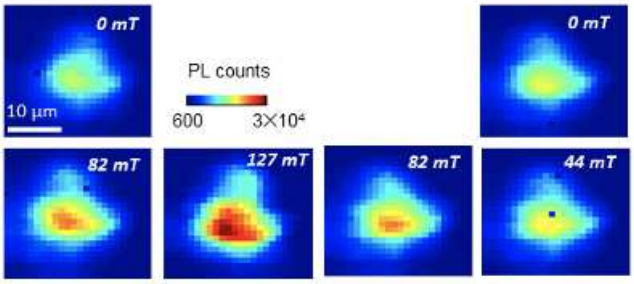

Figure 3-7 Figure S5 PL maps of a co-assembly of 10 nm MNPs with homeotropic LC alignment showing reversibility of PL enhancement.

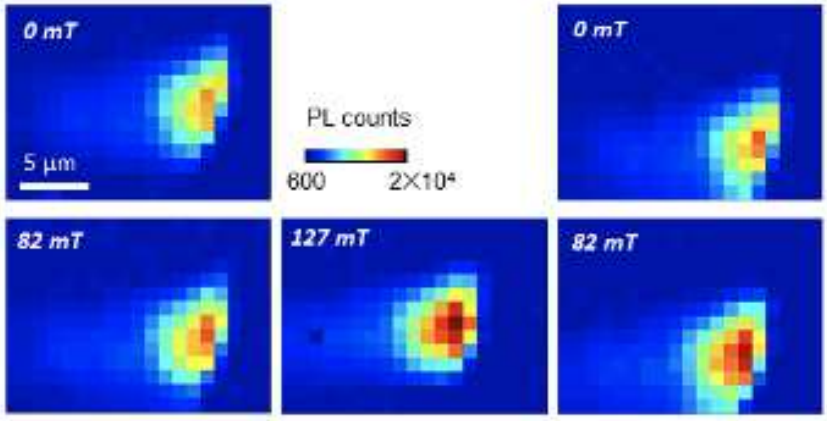

Figure 3-8 Figure S5 PL maps of a co-assembly of 10 nm MNPs with homeotropic LC alignment showing reversibility of PL enhancement.

Figure *3-7*. 10 nm MNPs had demonstrated some hysteresis, Figure 3-8 and when 20 nm MNPs are used to form the co-assemblies in Figure *3-9*, the change of PL intensity is found to be strongly dependent on the direction of applied field change. As the field is increased up to 127 mT, a small intensity enhancement is observed in the PL maps of Figure *3-9*A. As the field starts ramping down in Figure *3-9*B, QD emission intensity continues to increase, and by B = 82 mT on the ramp down, the integrated intensity is 21% greater than at the highest applied field.

At B = 0 the PL intensity is ~6% higher than the starting value. Further, this remanence persists for over 24 hours, shown in the PL map of Figure 9C. The observations of Figure *3-5* and Figure *3-9* are summarized in Figure *3-10* and suggest that while PL enhancement with applied field does not demonstrate a strong variation with MNP size, the reversibility of the PL enhancement does. In order to decipher this size dependence, it is useful to recall while all MNPs used here are most likely single domain (typically values

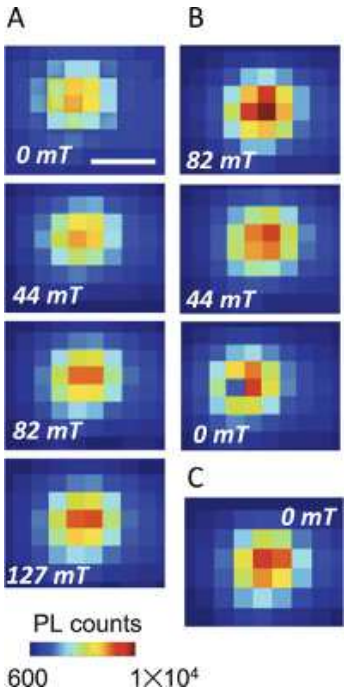

Figure 3-9 Spatially resolved PL maps tracking the intensity changes for co-assembly with 20 nm MNPs with (A) increasing and (B) decreasing magnetic field. (C) PL map taken 24 h after magnetic field was ramped to zero. Scale bar: 5 mm.

of 75–80 nm are found for the shift from single domain to multi-domain in the case of magnetite), only the 5 nm ones are superparamagnetic. It could therefore be the case that the 5 nm MNPs, acting as superparamagnets, do not demonstrate hysteresis, while the larger single domain MNPs show hysteresis effects because of clustering.

LC materials do respond to magnetic fields similar to the way in which they do to electric fields, i.e., above a certain threshold the LC molecules switch orientation, known as the Fréedericksz transition. However, the ultra-low magnetic susceptibility of LCs requires a large magnetic field to drive this re-orientation. For 5CB in particular, this critical threshold is ~600 mT[102]. This critical threshold can be lowered with the inclusion of dispersed MNP[103], and to track this, we monitored the LC orientation as a function of applied magnetic field using spatially-resolved scanning magneto-optical Kerr effect (MOKE)[102], schematically represented in Figure *3-11*A. MOKE leverages the interaction between the electric field of an incident optical excitation with the magnetization of the sample. Experimentally, a linearly polarized laser is reflected off the sample causing a change in the polarization direction, measured as the Kerr angle, θ_K. Typically, θ_K is directly and solely proportional to the magnetization of the sample under investigation, but here, the optical anisotropy of liquid crystal molecules contributes to the signal as well. MOKE measurement of LC samples with 0.04% wt. of MNPs dispersed in it allows an estimation of the threshold magnetic field required for Fréedericksz transition,

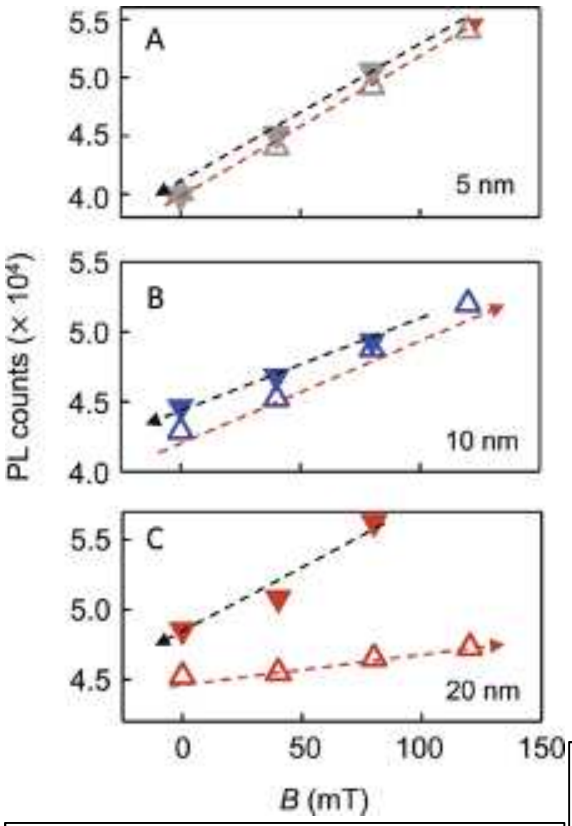

Figure 3-10 Integrated PL intensity for co-assemblies with (A) 5 nm MNPs, (B) 10 nm MNPs, and (C) 20 nm MNPs. Open triangles indicate magnetic field ramping up and filled triangles represent data taken while field was ramping down.

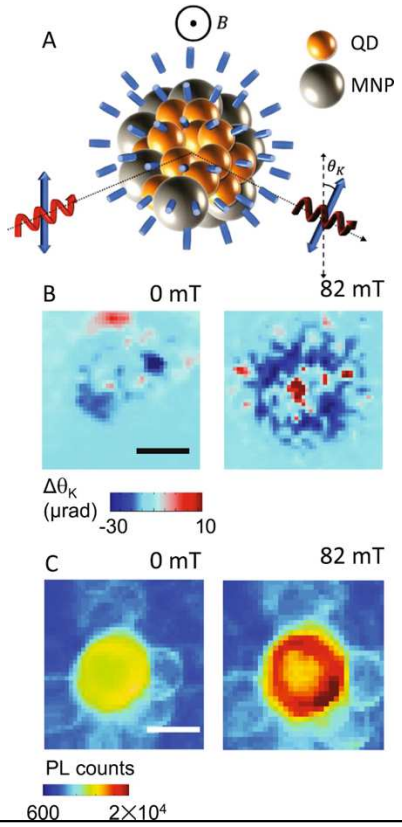

Figure 3-11 (A) Schematic of magneto-optical Kerr effect (MOKE). (B) Spatially-resolved map of Kerr angle change $\Delta\theta_K$ of a co-assembly of QDs and 10 nm MNPs with 0 and 82 mT applied magnetic field (C) Spatially-resolved PL scan of a similar co-assembly under the same conditions. Scale bar: 10 μm.

and we find that this critical field lies in the range of 310–350 mT for all the MNPs Figure *3-12*. Figure *3-6*B maps the MOKE signal at, and in the vicinity of, a single co-assembly with magnetic fields B = 0 and 82 mT directed out of the plane of the sample. The LC molecules are planar aligned to minimize the birefringence imparted to a p-polarized incident laser tuned to 632 nm, and the Kerr signal is plotted as $\Delta\theta_K$ to take this background into account. The maps look significantly different. The large positive $\Delta\theta_K$ at the center is the expected contribution from the superparamagnetic 10 nm MNPs. The change in $\Delta\theta_K$ surrounding the central assembly indicates a re-orientation of the LC molecules, despite the fact that the applied B is far smaller than the above-mentioned threshold field. Similar changes in $\Delta\theta_K$ are also observed in co-assemblies with 5 and 20 nm MNPs Figure *3-13*. The full impact of this effect is seen by comparing the two parts of Figure 11C, which are scanning PL maps of the same co-assembly at B = 0 and 82 mT. The application of the

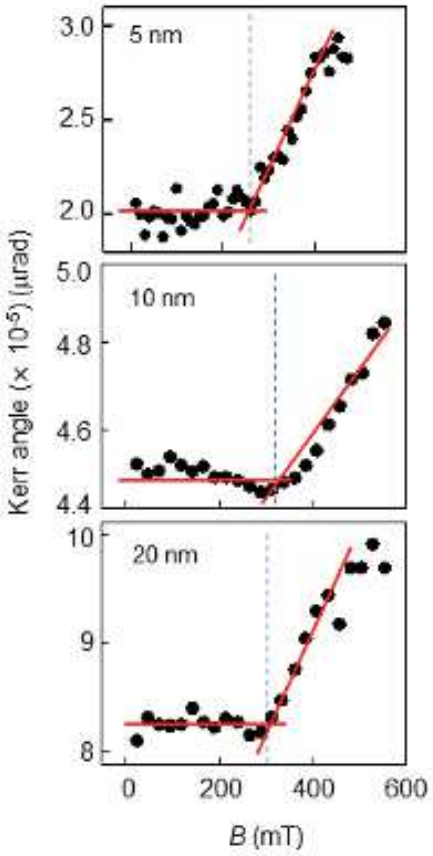

Figure 3-12 Birefringence of 5CB with 0.04% wt. of MNPs of various sizes measured using MOKE. The Kerr angle is proportional to the birefringence and the abrupt change at specific magnetic field marks the threshold of magnetically-driven LC re-orientation to align with the applied field. For all MNP sizes, the critical field lies within a narrow range between 310-350 mT.

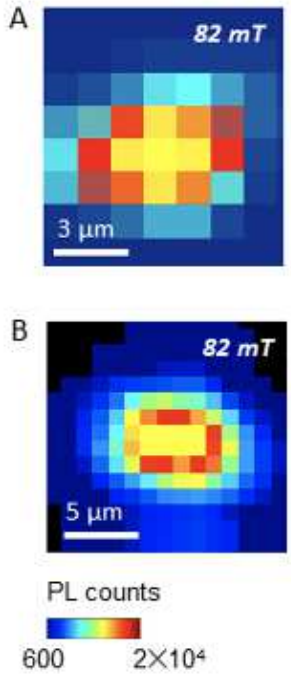

Figure 3-13 PL maps of a co-assemblies in planar LC alignment with QDs and (A) 5 nm MNPs and (B) 20 nm MNPs

field increases the emission intensity of the QDs throughout the entire co-assembly, but the enhancement is stronger around the outer edge. As magnetic field is increased further, the PL enhancement becomes more homogenous and by 225 mT the entire co-assembly shows an increase in PL counts by a factor of 2 Figure *3-14*. This edge-enhancement is observed at low applied fields in co-assemblies with 5 and 20 nm MNPs in planar aligned LC samples as well Figure *3-15*.

Given that the MNPs do rotate in the applied field as seen under L-TEAM and highlighted in Figure *3-3*, there are two possible mechanisms driving the LC re-organization: the steric effect of the physical MNP rotation, or the strong localized magnetic fields produced in the vicinity of the co-assemblies originating from the MNPs.

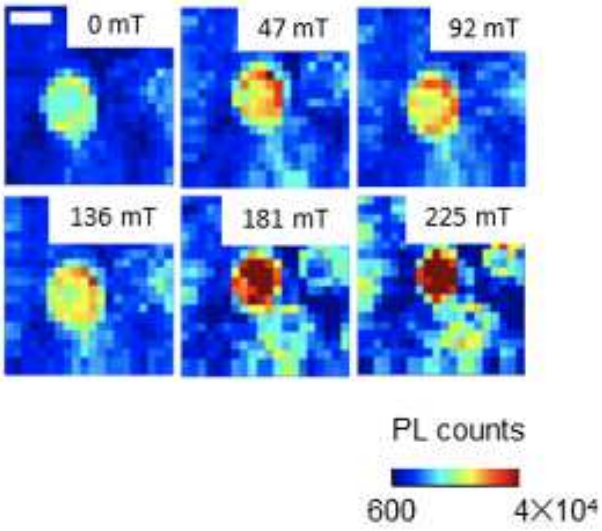

Figure 3-14 PL maps of a single co-assembly with 10 nm MNPs with increasing applied field. Initially the PL enhancement occurs along the outer periphery but eventually the entire assembly shows PL brightening. Scale bar: 2 μm

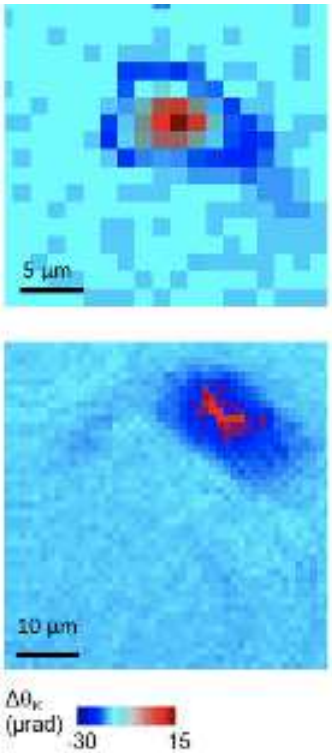

Figure 3-15 Spatially-resolved MOKE images of co-assemblies with QDs and (A) 10 nm MNPs and (B) 20 nm MNPs. Both dispersions are in homeotropic alignment.

The saturation magnetization values lie in the range of 70–45 emu/g[107] or all MNPs used here. A rough estimate of the number of MNPs in a 2 μm co-assembly yields ~10^7, and combining this with the density of Fe_3O_4 (7.9 g/cm^3), a single co-assembly is assessed to produce a maximum local field ~100 mT, which is of the order of magnitude of the threshold field. The L-TEAM results imply it is quite possible that this maximum local field is achieved and is the underlying cause of the LC molecules re-orienting and spatially compacting the QDs, resulting in a perceived higher emission within the field of measurement. The hysteresis observed with the larger MNPs, in particular the 20 nm ones, is likely resultant of greater inertia to relax back to random orientation as the applied field is decreased. The difference in the pattern of PL increase between Figure *3-5* and Figure *3-9* (at the center) and Figure *3-11* (at the circumference) can be attributed to the LC alignment in either case. For homeotropic alignment the director axis of the LC film is along the applied magnetic field everywhere except within the assemblies where the LC molecules are disordered due to the presence of the NPs. The LC orientational changes due to the increased local fields therefore are more prominent at the center. With planar arrangement, the LCs anywhere are more susceptible to the effect of localized strong magnetic fields and coupled with the fact that the MNP:QD ratio is higher at the

edges than the center, the PL increase in the samples in Figure *3-11* and Figure *3-6* begin at the outer circumference.

3.3 Conclusion

In conclusion, we have that the observed magnetic field driven emission enhancement can be tuned using the magnetic nanoparticle size and the LC alignment. The relative concentration of MNPs and QDs in the co-assemblies also play a role in the enhancement efficiency. It was previously[102] found that the optimal QD:MNP ratio where co-assembly was successfully achieved was between 1:1–1:2 when the total NP concentration was 0.02–0.04%. For co-assemblies with 1:1 proportion of QDs and MNPs, and an application of 80 mT increased the PL intensity ~60%[102]. In this current work, the fraction of MNPs is higher, approximately 1:2, and the enhancement is lower, between 25–38%, is irrespective of the LC alignment (for details of sample statistics, see Table 1 in Methods). Therefore, it would seem that the ratio of the constituent nanoparticles do have an effect on PL enhancement, with higher enhancement observed when the proportion of QDs is greater. The reversibility of this effect is also controllable by using larger MNPs, where the PL enhancement persists for over 24 h after the field is removed. Using L-TEAM, a unique in situ technique best-suited to understand the mechanism driving the PL enhancement, we have observed that the MNPs rotate to align in the direction of the applied field. Scanning MOKE shows that with a similar applied magnetic field, the LC molecules in the immediate vicinity of an MNP assembly also re-orient along the field, despite its magnitude being smaller than the critical field required to switch 5CB. Consideration of the L-TEAM and MOKE data together leads us to conclude that the MNP alignment along the applied field direction creates a strong localized field, which is close to what is needed to drive LC re-orientation, in turn bringing about the spatial compaction of the co-assemblies. The LC-driven assembly of nanoparticles, as we have demonstrated, is an attractive research area, both from fundamental and applied perspectives. And while characterization of these 3D assemblies is very challenging and requires highly specialized techniques for a complete picture to develop, this could be a highly-valued route towards the design of new materials where long-distance spatial order is unnecessary for novel functionalities.

3.4 Methods

3.4.1 Materials

The magnetic nanoparticles (MNPs) used in the co-assemblies are Fe_3O_4 NPs (purchased from NN-labs) with average diameters of 5, 10, and 20 nm, with Octadecylamine (ODA) ligand overcoat in toluene. The quantum dots (QDs) are CdSe/ZnS core-shell NPs (purchased from NN-labs) with a 6.2 nm core diameter and oleic acid (OD) ligand overcoat, also in toluene. The LC material is 4′-pentyl-4-biphenylcarbonitrile (popularly known as 5CB, purchased from Sigma Aldrich).

3.4.2 Sample preparation

For transmission electron microscopy (TEM) samples of QDs and MNPs without LC, 0.2 μL of stock solution (2 mg mL^{-1}) diluted to 1:10 is deposited directly onto Cu TEM grids with a carbon film (400 mesh, Ted Pella Inc) and then placed in a vacuum oven at 40 °C, −25 mmHg, for ~2 hours to evaporate residual solvent. For TEM analysis with LC, 0.2 μL of the mixture is deposited directly onto Au lacey carbon TEM grids (400 mesh, Ted Pella Inc). Excess solvent is wicked away with a Kimwipe and the samples allowed to cool slowly in an oven. Similar samples can be prepared by letting 20 μL of the mixture cool in an eppendorf tube and after the process is complete, following the same deposition procedure. As the samples are predominantly LC, there is no need to allow time for drying, as there is no solvent left to evaporate. To form the co-assemblies in LC, we mix the MNPs with 5CB at 0.04% (5 nm), 0.01% (10 nm) and 0.004% (20 nm) by wt. and sonicate at 40 °C for 3–6 hours. Then QDs are added to the mixture at 0.02% wt. and sonicated for another 4–6 hours. These proportions are chosen in order to maintain an approximate ratio of 1:2 ratio of QDs to MNPs. In the final stage of sonication, small amounts of the samples were checked for complete QD dispersion with fluorescence microscopy. The mixture is held at 40 °C and then placed in a vacuum oven and slowly cooled overnight, which drives the assembly of the NPs.

3.4.3 Measurement statistics

We prepared and measured between 8–10 samples with each size of MNP for each type of LC alignment for the PL enhancement measurements. For every sample

prepared, between 5–7 assemblies were studies in each. The PL enhancement factors (for applied fields of 127 mT) and variations are listed in the table below:

MNP size and LC alignment	Total # measured	Avg. PL enhancement (%)	SD of enhancement (%)
5 nm MNP, planar	48	26%	6%
5 nm MNP homeotropic	65	29%	8%
10 nm MNP, planar	52	32%	7%
10 nm MNP homeotropic	71	38%	5%
20 nm MNP planar	57	30%	8%
20 nm MNP homeotropic	67	33%	6%

This compilation indicates that for each size the homeotropic alignment yields higher PL enhancement.

3.4.4 Characterization techniques

TEM images are obtained with a JEOL-2010 TEM equipped with a LaB_6 filament and operated at 200 kV in the Imaging and Microscopy Facility, UC Merced. Transmission electron aberration-corrected microscopy (TEAM) imaging is performed using the TEAM I microscope (<1 nm resolution) in Lorentz mode at Lawrence-Berkeley National Labs (LBNL) at 300 keV. For application of the magnetic field, the samples are tilted to 20° and the field is applied using the objective lens parallel to the beam direction. Energy dispersive X-ray spectroscopy (EDS) imaging is performed with a CM 200 TEM machine set to diffraction mode operating at 200 keV. Brightfield, cross-polarized, and fluorescence microscopy are performed using a Leica DM2500P equipped with a Q-image Retiga camera Figure *3-16*. Scanning photoluminescence (PL) is performed by using a continuous wave Coherent CUBE laser (409 nm, with a diffraction limited spot size of approximately 0.5 μm) and collected with an Acton 300i spectrometer dispersed onto a thermo-electrically cooled CCD camera (resolution ~0.18 nm). The samples are placed on high-resolution motorized scanning stages that allow PL scanning with a diffraction limited resolution ~500 nm. MOKE data are taken with a continuous wave He-Ne laser (632 nm). A photo-elastic modulator (Hinds Instrument) is used to modulate the signal at 50 kHz and the Kerr rotation resolved using a lock-in amplifier technique with a resolution of 0.2 μrad[107].

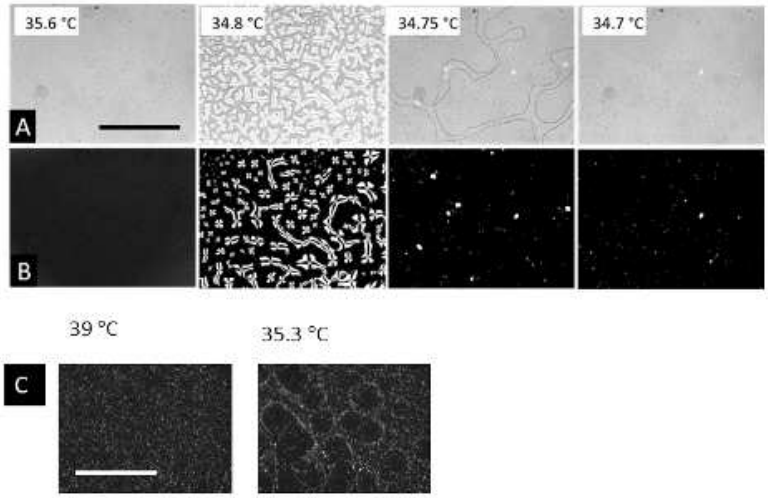

Figure 3-16 (A) Brightfield (B) Cross-polarized and (C) Fluorescence images taken as a function of temperature showing the directed assembly process.

3.5 Acknowledgements

This research was supported by funds from UCMEXUS-CONACYT, CBET-1507551 (to L.H. and S.G.), and in part by the NSF-CREST: Center for Cellular and Bio-molecular Machines (CCBM) at UC Merced (HRD-1547848). S.G. acknowledges support of the Aspen Center for Physics, which is supported by NSF PHY-1607611. Work at the Molecular Foundry was supported by the Office of Science, Office of Basic Energy Sciences, of the U.S. Department of Energy and by the Laboratory Directed Research and Development Program of Lawrence Berkeley National Laboratory under U.S. Department of Energy contract no. DE□AC02□05CH11231.

Chapter 4 Impact of Bis(imino)pyridine Ligands on Mesoscale Properties of CdSe/ZnS Quantum Dots

This chapter discusses an investigation of surface modification of CdSe/ZnS quantum dots (QDs) with bis(imino)pyridine (BIP) ligands. BIPs are organic ligands known to facilitate charge transfer in base metals on the molecular scale, but their behavior in nano- to mesoscale are largely unexplored. The optical and electronic properties were characterized by electron microscopy, crystallography, and ultrafast spectroscopy. Three variations are used, unsubstituted (BIP-H), dimethyl (BIP-Me), and diisopropyl (BIP-iPr) BIP. The results when compared to native octadecylamine ligand, we find that both energy and charge transfer efficiencies between QDs are increased post-ligand exchange, with BIP-iPr showing the highest of the three. Time-resolved spectroscopy was used to investigate the charge transfer from QD films to conducting (indium tin oxide, ITO) and semiconducting (zinc oxide, ZnO) substrates and found that the influence from the ligands is QD band gap dependent. The BIP ligands facilitate charge transfer to both ITO and ZnO substrates in QDs with a large band gap (2.3 eV), however, in dots with a small band gap (1.9 eV), the BIPs pose a hindrance when ZnO is used reducing recombination rates. The BIP ligands were found to also hasten the rate of QD photobrightening under continuous illumination leading to stabilized emission faster than with the use of native ligands. This study demonstrates a novel charge transfer system in the meso- and nanoscale, providing a diverse selection of new surface ligands for applications in conductive materials and energy production/storage devices that employ QDs.

Introduction

Semiconducting quantum dots (QDs) are widely implemented in a variety of applications that leverage their size-tunable optical and electronic properties.[108–110] These include optoelectronic devices, such as, photodetectors,[10,111,112] light-emitting diodes,[19] and photovoltaics[113] among others, as well as devices for biomedical sensing[9,114] and diagnostics.[115,116] In order to optimize performance in these platforms, the treatment of QD surfaces is of critical importance, given the dots' large surface-to-volume ratios, and the one effective approach to surface passivation is via the use of organic ligands.[6,7,117] The most common among these are long-chain aliphatic hydrocarbons, which have been proven very successful in passivating surface defect-related trap states, thereby suppressing nonradiative recombination and stabilizing the

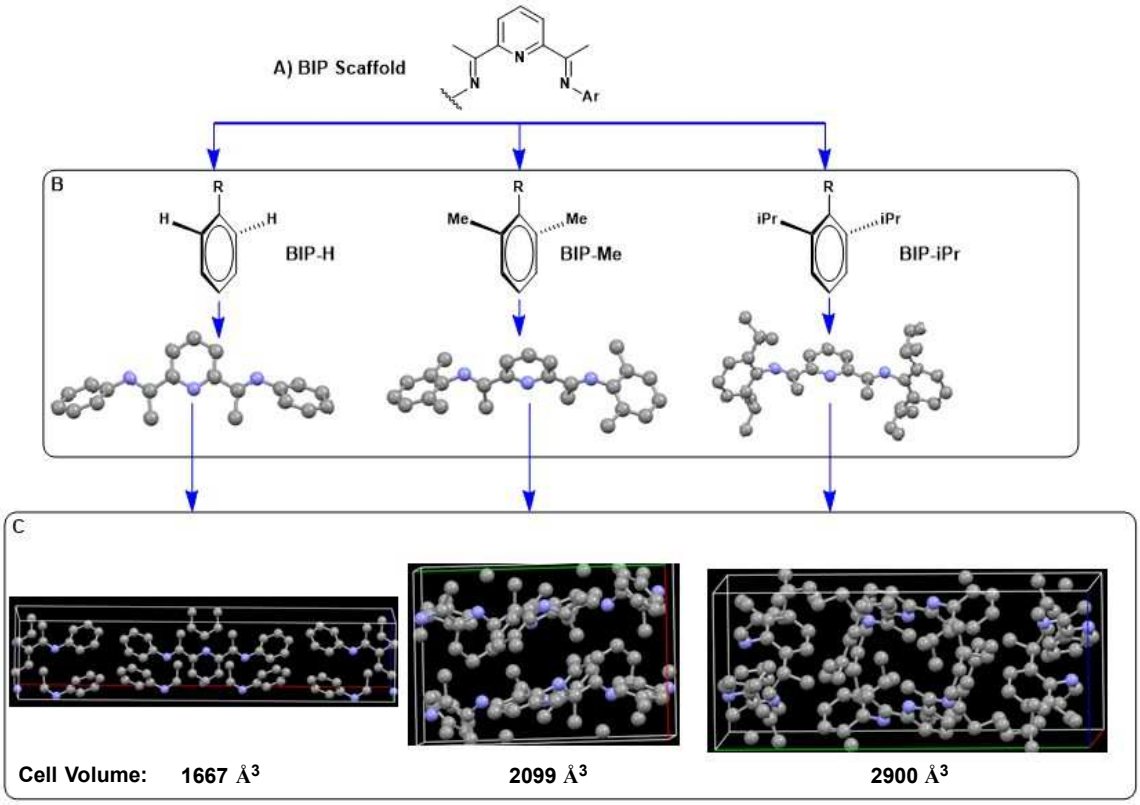

Figure 4-1 (A) The basic BIP scaffold (B) The three modular units used to design the ligands: BIP-H (unsubstituted BIP), BIP-Me (Dimethyl BIP), and BIP-Ipr (Diisopropyl BIP) (C) Unit cell structures formed by the ligands on crystallization.

QD core from photoinduced degradation, such as photodarkening and photo-oxidation.[118–121] However, as they insulate molecules they hinder transport of charge carriers within QD films, reducing the conductivity, and consequently, the performance in optoelectronic applications. Aromatic hydrocarbon molecules have facilitated interdot charge transport in QD films when used for surface functionalization owing to the presence of delocalized electrons, but these have occasionally altered the bandgap by reducing the excitonic confinement, especially when used in conjunction with metal complexes.[122–125] However, heterogenous charge transfer is a subject that garners interest not only in QD-based systems but across the scientific spectrum, from photovoltaics to electrode systems in batteries.[126] A specific type of charge transfer using organic ligands being heavily explored is for the purpose of advancing base metal catalysis and lowering the dependency on noble metals (palladium, rhodium, etc.). That area is dominated by a class of organic molecules referred to as “redox non-innocent ligands” (RNI). These ligands have the capability to perform reversible charge transfers between a chelated metal and itself. This ability to participate in charge transfer allows metals like iron and cobalt to perform like rhodium and palladium, respectively, in catalytic reactions, through the process of acting as electron reservoirs.[127,128] This

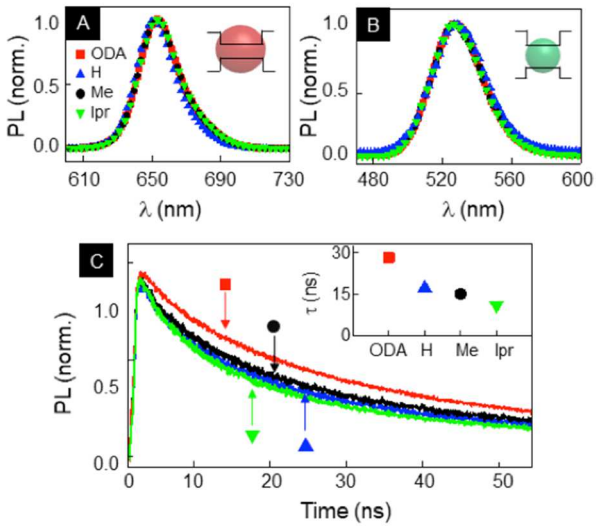

Figure 4-2 PL emission of (A) CZ640 and (B) CZ500 CdSe/ZnS QDs functionalized with ODA and the three BIP variations. (C) Time-resolved PL for all four populations of QD films deposited on an insulating glass substrate. (Inset) Recombination lifetime τ extracted from exponential fits to the data in the main part.

principle of RNI molecules acting as electron reservoirs is highly intriguing and has yet to be applied on systems outside of the molecular scale. In this article, we demonstrate that RNI ligands can be utilized to modulate the optoelectronic properties of nonmolecular scale systems such as semiconducting QDs through enhanced interdot charge and energy transfer.

We focus on a highly recognizable and well-behaved class of RNI ligands, the bis(imino)pyridine (BIP) scaffold (Figure 4-1A). The BIP scaffold is used for traditional organometallic chemistry[129–131] where it functions as the single-electron reservoir to facilitate two-electron processes with base metal catalysts. We use three variations of BIPs, unsubstituted (BIP-H), dimethyl (BIP-Me), and diisopropyl (BIP-Ipr) BIP (Figure *4-1*B) to displace the native ligand, octadecylamine (ODA), of CdSe/ZnS core/shell QDs. Single crystals of each BIP are obtained to provide insights into how these ligands may orient/pack on the surface of the QDs. Then, using electron microscopy and ultrafast spectroscopy, we reveal that structure-specific π–π stacking of the BIP ligands alters interdot separation in QD films, which correlates with the crystal lattice features of BIPs in the solid state (Figure *4-1*C, unit cells of single-crystal data shown). This change in interdot separation leads to remarkable changes in both optical and electronic properties of the BIP-QD film in comparison to the native ligand. These include increases of both energy and charge transfer efficiencies between QDs post ligand exchange, the highest achieved with BIP-Ipr. We further investigate charge transfer from QD films to conducting (indium tin oxide, ITO) and semiconducting (zinc oxide, ZnO) substrates using time-

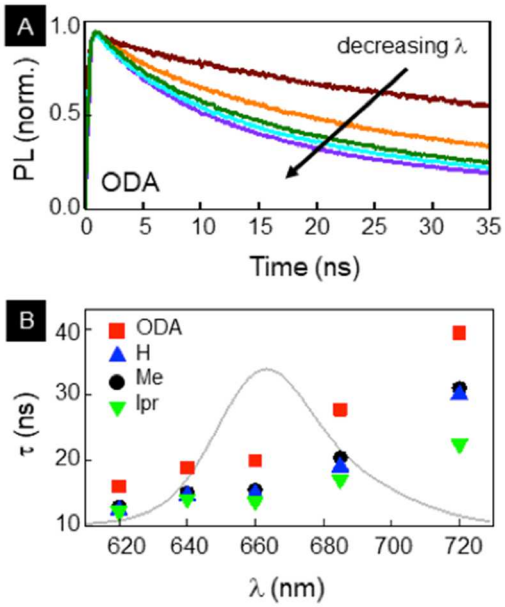

Figure 4-3 (A) Time-resolved PL curves at different spectral bands of the emission curve for the ODA-functionalized QD film. Lifetimes decrease with decreasing emission wavelength. (B) Spectrally resolved recombination times τ for all four QD films superposed on the corresponding spectral region over which they are evaluated.

resolved spectroscopy and determine that the influence of the BIP ligands is QD bandgap dependent. In QDs with a large band gap (2.3 eV), the BIP ligands facilitate charge transfer to both ITO and ZnO substrates, but in dots with a small band gap (1.9 eV), they pose a hindrance when ZnO is used, resulting in reduced recombination rates. Surface states also play a significant role in the photostability of colloidal QDs.[132,133] Photoinduced changes include photo brightening, photodarkening, and photo-oxidation, all of which result in changes in spectral emission intensity and wavelength over time. These shorten the shelf-life of QD samples and affect performance. The presence of ligands passivates the surface states and arrests these processes to varying degrees,[120,134,135] and therefore, it is important to investigate this aspect following a ligand exchange. We verify that BIP ligands hasten the rate of QD photobrightening under continuous illumination, allowing the ensemble to achieve stable emission faster than in their native configuration.

Results and Discussion

To investigate intermolecular packing and size properties of QDs bound with organic BIP ligands, single crystal X-ray analyses were performed on each unbound ligand shown in Figure *4-1*. Substitution at the 2- and 6-positions of the aniline subunits produced solid-state molecular geometries that minimize steric interaction between the aniline and central pyridine units, causing an out of plane tilt of aromatic rings that increases with substituent size (molecular geometries shown in Figure *4-1*B, i-Pr > CH3 >

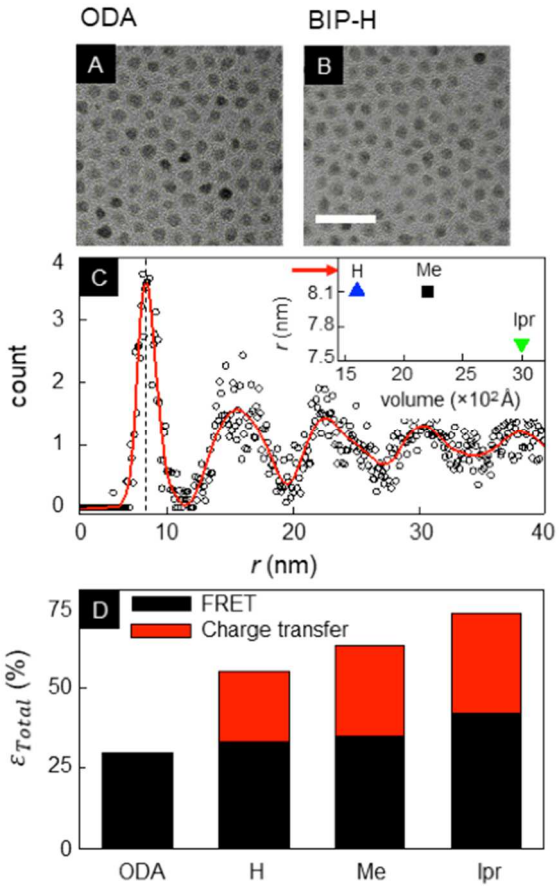

Figure 4-4 TEM images of drop-cast QD films with (A) ODA and (B) BIP-H ligands. Scale bar: 50 nm. (C) Radial distribution of interdot separation r obtained from TEM images and (inset) r values of the BIP variations plotted with the unit cell volume. Arrow indicates r for ODA-functionalized QDs. (D) Energy and charge transfer efficiencies for the four QD populations.

H for the degree of out of plane aromatic tilt). These results are consistent with previous reports of BIP ligands when chelated to a central metal in a Lewis basic fashion.[136] Although the geometric configuration of an single BIP ligand may be unsurprising, analysis of unit-cell packing is likely more informative for considering the bulk properties of numerous ligands creating a surface layer on the exterior of QDs. Because of the size disparity between QDs and BIP ligands, direct binding of the central pyridine to the QD surface is unlikely. Alternatively, induced dipole interactions between BIP π-systems and the QD surface could provide electrostatic attraction to promote an alternative mode of binding. Subsequent layers of BIP ligands extending from the QD surface would depend on intermolecular forces between BIP ligands to determine the overall size of the BIP-ligated QDs.

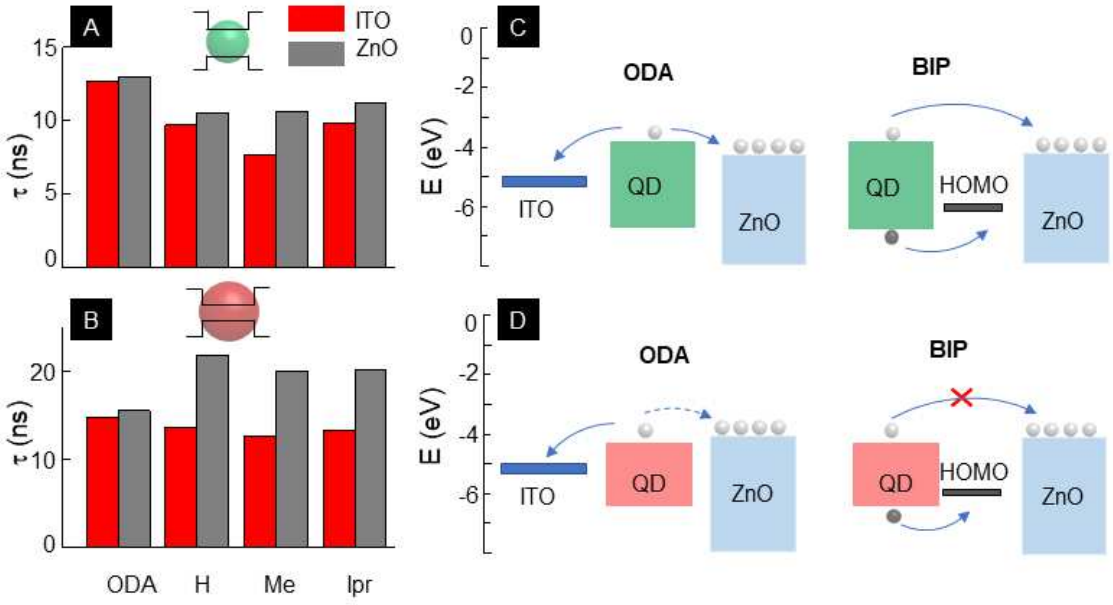

Figure 4-5 Recombination times τ for (A) CZ500 and (B) CZ640 QD films functionalized with ODA and the BIP ligands, when deposited on conducting ITO and semiconducting n-ZnO substrates. (C,D) Schematics sketching the charge transfer routes for the differently sized QDs.

As shown in Figure *4-1*C, the unsubstituted BIP-H ligand interacts primarily through the pre-existing dipole of the central pyridine unit, resulting in a tightly packed unit cell with the smallest observed volume and less than 3 Å between repeating pyridine units. The reduced steric size of BIP-H renders it the only ligand studied that packed in this fashion. Unit cells for the remaining ligands showed primarily π–π interactions between aniline subunits on neighboring ligand molecules, resulting in larger values for the distance of interligand spacing and overall unit cell volumes for BIP-Me (3.7 Å spacing, 2099 $Å^3$ volume) and BIP-Ipr (4.5 Å spacing and 2900 $Å^3$ volume) ligands. Such a difference in packing and interligand distance affects the physical and electronic properties of QDs ligated with different BIP ligands, resulting in unique structure–activity relationships for the QDs depending on their environment (*vide infra*).

We summarize the basic spectroscopic characterization of QDs post ligand exchange in Figure *4-2*, along with the results of the ODA-ligated control dots for comparison. This is an important check because surface functionalization can cause changes in quantum confinement, which result in an emission red-shift, or proliferation of surface defects, which may accelerate core photo-oxidation and darkening. Photoluminescence (PL) of CZ640 and CZ500 nm QDs dispersed in solution shown in Figure *4-2*A,B confirms that there are no significant changes to any aspect of the emission

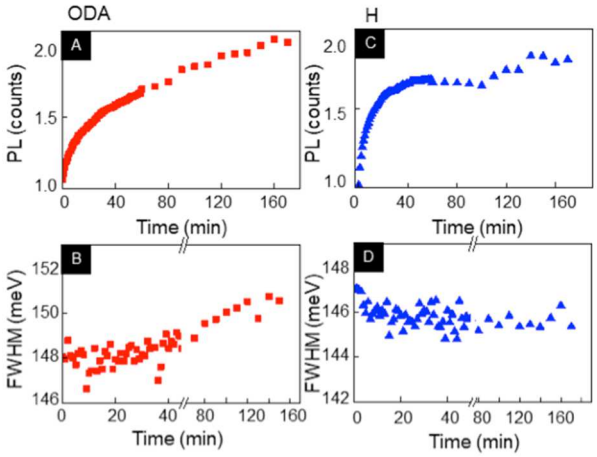

Figure 4-6 (A) Spectrally integrated PL intensity and (B) fwhm of the emission spectra for ODA-functionalized QDs under constant photoexcitation as a function of illumination time. (C) Spectrally integrated PL intensity and (B) fwhm of the emission spectra for BIP-H-functionalized QDs measured under the same conditions.

spectra after the ODA ligands are exchanged by the three variations of BIP. Photoluminescent quantum yield (PLQY) is another critical parameter that directly reflects the impact of ligand exchange. Our measurements do not reveal a significant difference in the PLQY between different QD populations. For ODA, H, Me, and IPr, the measured PLQYs are 35, 30, 36 and 32%, respectively. Time-resolved PL measurements of the QDs in a dilute solution further reveal no distinction between dots functionalized with ODA, BIP-H, BIP-Me, and BIP-Ipr, with the recombination time for all four populations being 40 ± 3 ns. Figure *4-2*C plots the time-resolved PL curves for QD films deposited on a glass substrate, and the charge recombination lifetimes are calculated by first using a biexponential fit $I_{PL} = A_1 e^{-t/\tau_1} + A_2 e^{-t/\tau_2}$ and then using the results to extract the average lifetime $\tau = (A_1\tau_1^2 + A_2\tau_2^2)/(A_1\tau_1 + A_2\tau_2)$. These values are plotted in the inset and show a clear variation between the native ODA and the BIP ligands, where τ decreases from 30 ns for ODA-QDs to 11 ns for BIP-Ipr. Faster lifetimes are the norm when comparing QDs in films versus isolated QDs in dilute solutions, as interdot interactions allow additional routes of charge recombination. These mechanisms, the resulting timescales, and associated effects are strongly dependent on surface states and the subsequent modifications, a good overview of which has been previously described.[137–140] The most common mechanism is Forster resonant energy transfer (FRET), a dipole–dipole coupling where the efficiency $\varepsilon \sim 1/r^6$, r being the interdot separation.[137] These data would, therefore, suggest that the distance between QDs in the films, on average, decreases in ODA-, BIP-H-, BIP-Me-, and BIP-Ipr-functionalized QDs.

In an ensemble, FRET occurs as a result of the size inhomogeneity of the QDs, and the roles of donors and acceptors are satisfied by the smaller and larger dots in the population. As a result, the extent of FRET varies with wavelength of the emission

spectrum. We verify this in Figure *4-3*. Time-resolved PL curves for ODA-QDs with spectral resolution are plotted in Figure *4-3*A, and the recombination can be seen to get faster as the emission wavelength at which the data are taken decreases. Figure *4-3*B shows the extracted τ across the emission spectrum for all four differently ligated QDs. For ODA-QDs, we notice the expected variation of τ with wavelength, as well as the fact that at the long wavelength end, τ approaches the lifetime measured in solution. For the BIP-functionalized QDs, the trend is the same, but the shorter lifetimes even at the reddest end of the spectrum imply that the recombination is much faster than the solution values. This would indicate that there is some other route in addition to FRET, and the nature of aromatic ligands would suggest that to be charge transfer.

There remains the possibility that some of the difference in recombination between the ODA-QDs and the BIP-QDs may be because of the differences in interdot separation. To investigate that, we analyze the transmission electron microscopy (TEM) images of close-packed QD films, such as those shown in Figure *4-4*A,B, for ODA and BIP-H functionalized QDs, respectively. For each type of QD, we generate a pair-distribution function (PDF) of its TEM image, as shown in Figure *4-4*C, which plots the probability of finding a QD at a separation r from another QD. The first peak of this PDF is the average nearest-neighbor distance between the dots, and from this main figure which shows the PDF of ODA functionalized QDs, that distance is 8.3 nm. Similar analyses of the other QDs return varying QD separations and are plotted in the inset as a function of volume of the ligand unit cells. The inverse relation provides an interesting insight into the packing efficiency of the different ways the three BIP ligands stack. However, it also implies that there is a variation in FRET efficiency based on the ligand on the QDs. As shown in Figure *4-1*C, the shape of the packing units (unit cells) is not uniform across the three BIPs studied. This shape disparity likely affects the mode of ligand stacking on QD surfaces, which should directly impact interdot separation.

We return to the averaged lifetimes of the QD films in the inset of Figure *4-2*C and using τ of ODA-QDs in film and solution, calculate the efficiency $\varepsilon_{total} = 1 - {\tau_{film}}/{\tau_{solution}}$.[97] As ODA is insulating, it is reasonable that energy transfer is the only interdot interaction among these QDs, and given that, we extract the FRET constant R_0 using $\varepsilon_{total} = \varepsilon_{FRET} = {1}/{1 + ({r}/{R_0})^6}$ $\varepsilon_{total} = \varepsilon_{FRET} = 1/1 + (r/R_o)^6$. $R_0$is defined as the separation where ε_{FRET} = 50% and is theoretically calculated using the overlap integral of the donor emission spectrum with the acceptor absorption spectrum and its mutual molecular orientation. Here, we evaluate it by equating the two expressions of ε_{FRET} and estimate R_o = 7 nm, which is very close to the rigorously calculated value of ~6.8 nm. Then, we calculate ε_{FRET} for the QDs ligated with the BIP ligands using this distance-dependent relation and the same Ro and when plotted in Figure *4-4*D, it highlights that FRET does increase in the case of the BIP-functionalized QDs. However, when we calculate $\varepsilon_{total}$for the BIP-QDs using the formulation involving recombination times,

those values are significantly greater than what is accounted for by FRET. For example, ε_{total} = 54% for BIP-H QDs but ε_{FRET} = 33%. We attribute this difference to charge transfer, and calculate that efficiency $\varepsilon_{total} - \varepsilon_{FRET} = \eta$ to be 21% (BIP-H), 28% (BIP-Me), and 30% (BIP-Ipr) functionalized QDs. The increase of η between the different BIP ligands follows the trend of ε_{FRET}in them, both getting larger as interdot separation decreases in the QD films. To identify the nature and mechanism of charge transfer, we note that the BIP ligands are photogenerated hole-acceptors as their highest occupied molecular orbital (HOMO) aligns above the QD valence band. BIPs share similar structural elements to a well-known high efficiency hole acceptor, triazatruxene (TAT). The similarities between TAT and BIPs is significant with both molecules comprising of primarily SP2 hybridized carbons and nitrogens, as well as having extensive π character. This extensive π character is known to facilitate hole mobility and stabilize charged states through a reduction in the energy gap between the HOMO and lowest unoccupied molecular orbital bands. Along with extensive π π character, various heteroatoms (nitrogens) also facilitate charge stabilization.[141]

While inter-QD charge transfer is important or optimal device performance, efficient and fast charge extraction at electrodes or other interfaces is also a necessity. With this in mind, we investigate the recombination dynamics of the QD films when deposited on metallic and semiconducting substrates. The four differently ligated QDs are spin coated onto ITO-coated glass and on the optically polished n-type zinc oxide (n-ZnO) single crystalline sample. The recombination time τ for both sized QDs on the two substrates is shown in Figure *4-5*A,B. For CZ500 (the smaller QDs with a larger bandgap), charge recombination times when ligated with ODA, while expectedly shorter than on glass, are nearly the same (12.6 and 13 ns) on ITO and ZnO. When functionalized with BIP variations, recombination does get faster for both substrates, which may be attributed to the charge delocalization of the aromatic rings resulting in a narrowing of the band gap between the QDs and substrates.[130,141–144] The schematics in Figure *4-5*C demonstrates the relative band alignments of ITO and ZnO with the QD. The positional advantage of the QD conduction band makes electron transfer to either substrate energetically favorable when functionalized with ODA (Figure *4-5*C, left). However, the hole-accepting nature of the BIP ligands allows both electrons and holes to be transferred away from the QD core, resulting in the faster recombination in the BIP-QDs (Figure *4-5*, right).

The same measurements for CZ640 QDs, which are larger and, therefore, have a smaller bandgap, have different results. For ODA, τ is again very similar on ITO and ZnO (14.7 and 15.3 ns, respectively). As the left schematic in Figure *4-5*D shows, electron transfer to ITO is clearly favorable. Although the conduction band of ZnO ~0.1 eV is above that of the QD, stochastic electron transfer is allowed. BIP-QDs show a minor increase in electron transfer to ITO, driven again by the delocalized charges of the ligands. However, the change in the recombination rate when BIP-QDs are deposited on ZnO is both significant and unexpected. Recombination lifetimes of BIP-QDs are approximately 30%

longer than that of ODA-QDs, indicating that functionalization by the BIP ligands, while facilitating hole transfer, somehow prevents electron transfer from the QD. As the excitation energy used in our studies is smaller than the wide bandgap of ZnO, the presence of oxygen vacancies makes as-grown ZnO highly n-doped. Therefore, a possibility is that the delocalized electron cloud of the BIP ligands not only interacts with the photogenerated electrons in the QD core, but also with those in the conduction band of ZnO. This has no consequence for the smaller QDs, where the difference between the energy levels of the QD core and ZnO drives electrons from the former to the latter. The near alignment of conduction bands in the case of the larger QDs and ZnO removes the advantage of this driving potential and concludes with the BIP ligands preventing electron extraction, while still allowing hole transfer. As a result, the recombination rate drops. This modulation of charge carrier transfer based on band alignment between the QDs and the substrates mediated by the BIP ligands is an interesting finding, as it opens up the possibility of tailoring functionalization based on specific needs of an application. An important point to note here is that while the charge transfer efficiency η in the QD films is ligand dependent, as shown in Figure *4-4*D, in this demonstration of charge transfer from QDs to ITO and ZnO, there is little variation of the same with the different BIP ligands. We attribute this distinction to the fact that while charge transfer in the former is determined by inter-QD separation, for the latter the energetics control the efficiency. A second look at Figure *4-4*D shows that η in the ascending order is IPr > Me > H, and as the inset in Figure *4-4*C confirms, interdot separation follows H > Me > IPr. This is also the reason that no charge transfer is observed when the QDs are in solution. Transfer to substrates is nearly independent of which BIP ligand is used as the HOMO levels of all three are within 0.5 eV of each other and are, therefore, all nearly equivalently aligned with the QD valence band.

However, as mentioned earlier, the influence of ligands extends beyond that of transient charge transfer. Modification of QD surfaces may adversely affect long-term photostability of the QDs, and in Figure *4-6* we compare how functionalization with BIP ligands alters photoinduced effects. Figure *4-6*A plots the spectrally integrated PL intensity for ODA-QDs over time under continuous photoexcitation. It increases rapidly for the first 20 min and then continues to rise at a slower rate. This photobrightening is a sign that there exist trap states within the bandgap of the core, most likely at the core–shell interface. Photogenerated carriers saturate these states, effectively deactivating nonradiative recombination centers, resulting in increasing PL. However, over the same time frame, the full width at half-maximum (fwhm) of the QD ensemble increases, which, coupled with a small blue-shift of the emission wavelength, suggests there is photo-oxidation of the QD core. As this reduces the core diameter, the size inhomogeneity of the ensemble is worsened, and the spectral width enhanced. In contrast, the photobrightening of BIP-H QDs stabilizes much faster and there is no observable increase in the emission fwhm over time. It is known that hole-accepting ligands can passivate QD surfaces more effectively than insulating ones[130] and our results confirm that here. It is also an important result as

it demonstrates there are no detrimental long-term stability effects as a result of the BIP ligands.

Conclusions

Heterogenous charge transfer has continued to be a critical area of advancement in science because of the increase in demand of society on technology that predicates itself off interfacial charge movement. The role of heterogenous charge transfer in modern conveniences such as smart phones to energy infrastructure cannot be under-represented. This importance on understanding heterogenous charge transfer has set the stage for this work and has shown both a novel and nuanced approach to modulate the kinetics of mesoscale heterogenous charge transfer. This was accomplished through the functionalizing semiconducting QDs with redox noninnocent (RNI) ligands as hole acceptors. Through nonstandard application of these RNI ligands, controlled modulation of the charge transfer dynamics has been achieved on mesoscale materials. Moreover, this study has illuminated an intriguing band gap dependence on the photoluminescent recombination lifetimes, which can be observed across both deposited substrates of ITO and ZnO. While interesting, further work is needed in terms of characterizing the complex charge transfer dynamics as well as the effect of other RNI type ligands through tuning of the band gap.

Methods

Representative Ligand Synthesis

BIP ligands were synthesized through azeotropic distillation of 2,6-diacetylpyridine in toluene with the corresponding aniline. 2,6-Diacetylpyridine (3 mmol), the aniline derivative (12 mmol), and p-toluenesulfonic acid (0.3 mmol) were added to a flame-dried 250 mL round bottom flask. Dry toluene (100 mL) was added, and the resulting mixture was refluxed using a Dean–Stark apparatus for 24 h. The reaction mixture was cooled to room temperature and aqueous saturated sodium bicarbonate (100 mL) was added. This mixture was transferred to a separatory funnel and the organic layer was extracted. The aqueous layer was washed 3–4 times with dichloromethane and the organic layers were combined, dried with sodium sulfate, and concentrated. The resulting concentrate was dissolved in 15–20 mL of methanol and placed at −20 Celsius for approximately 12 h. The resulting yellow solid was vacuum filtered and washed with cold methanol. ^{1}H NMR was used to assess purity and recrystallization in cold methanol was performed if impurities were detected. Single crystals were grown through solvation in hot methanol and allowed to cool over night at room temperature.

Ligand Exchange

ODA-capped CdSe/ZnS QDs CZ640 (bandgap 1.91 eV) and CZ500 (bandgap 2.3 eV) were purchased from NN-Labs. CZ640 QDs have a core diameter of 4.8 nm (5–10% size inhomogeneity) and CZ500, a 2.0 nm core diameter (10–15% size inhomogeneity). Their surfaces were modified using BIP-H, BIP-Me, and BIP-Ipr. Surface exchange was carried out under inert conditions by adding the QDs to a hexane solution containing an excess of the modifying ligands relative to the native ODA. This solution is incubated for at least 5 min and then purified with acetonitrile (MeCN) and chloroform ($CHCl_3$). The QDs are then separated by centrifugation and dispersed in hexanes for optical measurements.

Sample Preparation

For analysis in solution, the QDs were housed in 2.5 mL glass vials. For measurements of QD films, the dots were spin coated onto glass, ITO, and n-ZnO (zinc oxide) substrates at 4500 rpm for 15 s, followed by annealing in an oven for 50 °C for 30 min.

Spectral Characterization

For static spectroscopy, we use a Princeton Instruments SP2300i spectrometer coupled to a thermoelectrically cooled deep depletion and low noise charge coupled detector, with a spectral resolution of 0.18 nm. An NKT Photonics Super-K laser tuned to 430 nm is used for excitation. For time-resolved measurements, the Super-K is set to a repetition rate of 26 MHz and the collected signal is first dispersed using the spectrometer, and then directed onto a single-photon avalanche diode coupled to a PicoHarp 300 time-correlated single photon counting system with an instrument response function of 28 ps.

Transmission Electron Microscopy

QD solutions were pipetted onto Pure C on 300 mesh Cu grids and left to dry overnight in an oven at 50 °C, then imaged in Thermo Fisher's Talos F200C G2 TEM.

Acknowledgements

The work was done in collaboration with Dr. Ryan Baxter and Ryan Brisbin who synthesized the custom designed bis(imino)pyradine ligands. This article is based upon work supported by the National Science Foundation under grant nos. NSF-CAREER 1752821 (R.D.B.) and NSF-CREST HRD-1547848 (S.G., M.D.B., and R.P.

Chapter 5 Bis(imino)pyridine-CdSe/ZnS Nanoparticle Interactions: Shell Structure and Self-Assembly

Herein we investigate the effect of non-mesogenic ligands, bis(imino)pyridines (BIPs), on the phase transition temperature of 5CB and the subsequent role that plays in guiding the self-assembly of nano to micro scale shells with quantum dots. Resulting self-assembled structures are characterized in depth through SEM while population dispersity is determined through differential light scattering. Weighted ratios computed for the population dispersity of BIP-QD shells serves as a proxy for equilibrium constants. Differential scanning calorimetry determined enthalpies of the isotropic/nematic phase transition of 5CB as a function of BIP ligand weight percentage.

Introduction

As advancing technology and engineering demand more complex structures on smaller length scales, systems relying on self-assembly become critical. Although numerous technologies utilize self-assembly, those relying on mesogenic host-guest interactions are of interest for their high degree of both modularity and understanding of the physics associated with them. While certain aspects of self-assembly in these systems are well characterized, little is known about the effect of thermodynamics associated with the guest interaction of non-mesogenic guests in a mesogenic host. Advancement of critical technologies including computer circuitry, medical, and energy devices have all become reliant on precision engineering on progressively smaller length scales.[145–148] However, a known paradigm is that decreasing length scale increases the difficulty of precision engineering. Current limits of effective engineering have been established at the nano and micro scales. Further decreases in length scale, such as atomistic scale, have been achieved but the difficulty of precision engineering at that scale limits the use in device fabrication.[149,150] Difficulties in small-scale engineering has led to the pursuit of self-assembling systems that negate the need for mechanical intervention.[151–156] These systems are typically comprised of various organic or organo-metallic components that, when exposed to an appropriate set of conditions, assemble into complex structures.[157–159] An intriguing subset of these self-assembling systems are those guided by host-guest interactions of mesogenic solvents.[160,161] These mesogenic systems are structurally diverse with the potential for modularity through iterative variation of both host and guest structures. In a majority of these systems the self-assembly process of the "guests" (dendrimers, nano particles, etc.) takes place at the phase transition boundary.[162–164] While the phase transition process in mesogenic solvents ("hosts") has demonstrated significance in the assembly process, little is known regarding the effect of host-guest

interactions. Currently, it is known that self-assembly in these systems is a complex processes in which the conservation of global entropy is critical to achieving thermodynamic equilibrium.[165,166] Little is currently known about the use of non-mesogenic materials for the formation process in a mesogenic host. Herein we demonstrate the effect of using non-mesogenic, bis(imino)pyridine ligands (BIPs) for guiding the self-assembly process of cadmium selenide zinc sulfide quantum dots (CZ QDs) in a mesogenic host media of 4-Cyano-4'-pentylbiphenyl (5CB). Subtle changes to the non-mesogenic materials results in a tunable assembly process yielding shell-like structures of predictable size. Average shell sizes were confirmed using scanning electron microscopy and dynamic light scattering. The formation of specific shell sizes was found to be driven primarily by subtle alterations of the thermodynamic parameters associated with isotropic/nematic phase change of the 5CB and the BIP-CZ-host interactions. The ability to reliably produce 3-dimensional shells on the meso- and nano-scales has potential applications to light-scattering (cloaking) and drug delivery systems.

Results / Discussion

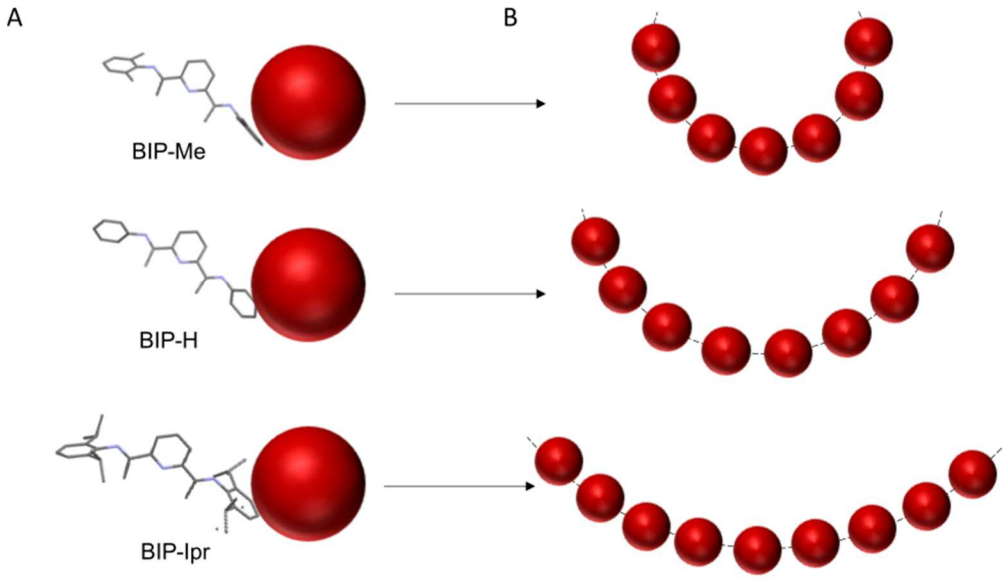

Figure 5-1 Illustrations of how ligand binds to QD and the curvature of shell wall. (A) BIP molecules binding with the outer aryl groups on the surface of the QD. (B) Illustrates a curvature dependence on the BIP ligand and resulting average shell size distribution.

Previous work demonstrated the bis(imino)pyridine (BIP) ligand could successfully bind to the surface of cadmium zinc sulfide quantum dots[167]. Further investigation of BIP-QD properties demonstrated the ability to form 3-dimensional shell structures. Figure 5-1A illustrates how the ligands may bind to the surface of the nanoparticle. Shells composed of densely packed functionalized NPs form upon the phase transition of 5CB from isotropic to nematic phases Figure 5-1B.

This self-assembly method has previously been shown for alternative sets of ligands[18,33,168]. These ligands possessed long aliphatic chains and series of aromatic linkers to confer mesogenic properties but required cumbersome syntheses to produce small quantities. Alternatively, BIP ligands are synthesized efficiently from only a few steps, allowing structural modularity in an efficient manner. Multiple aromatic systems and Lewis basic nitrogens still present in the BIP system presented a structural platform for exploring their efficacy in replacing previous ligands in the shell-forming process. The NPs were able to disperse uniformly in the isotropic phase when checked directly after removal on a heated 50 °C glass slide and coverslip and heated plate for fluorescence microscopy. The formed shells were too small to resolve on with fluorescence and confocal microscopy. Characterization of the nanoscale morphology of the NP shells were acquired with scanning electron microscopy (SEM).

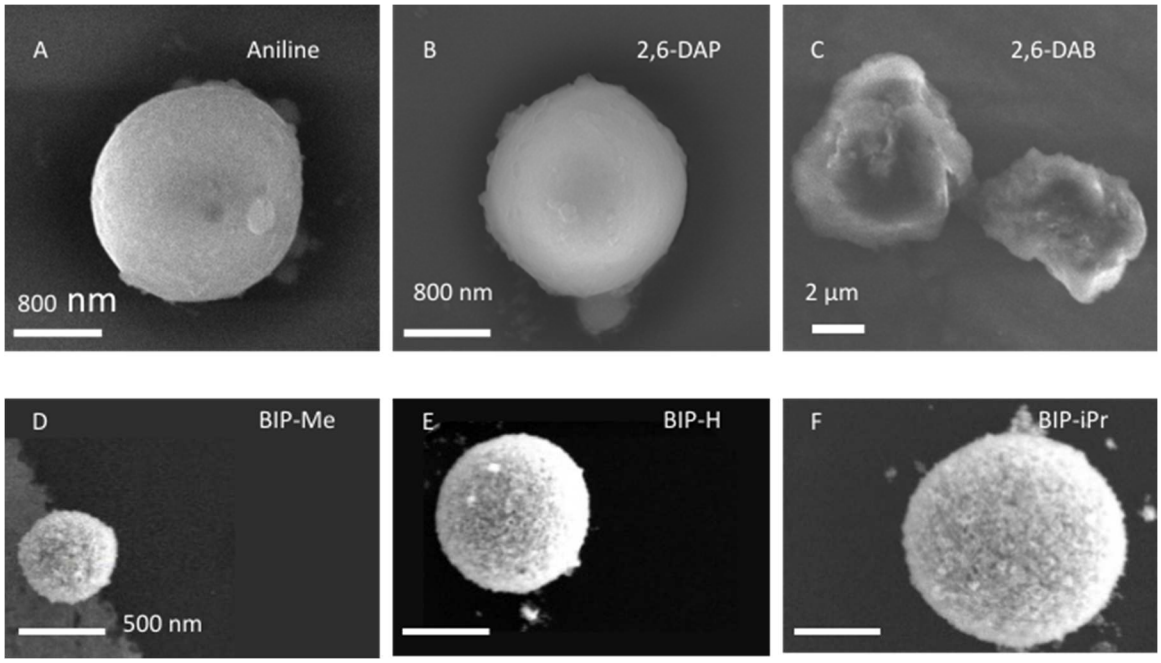

Figure 5-2 SEM images of self-assemblies. The control ligands on QD surface are shown for (A) Aniline, (B) 2,6-DAP, and (C) DAB. The BIP ligands on the QD surfaces shown for (D) BIP-Me, (E) BIP-H, (F) BIP-iPr.

After confirming that the BIP ligands were able to form shells, controls were devised from components that make up the BIP ligands. Aniline, 2,6-DAB, and 2,6-DAP were provided fundamental understanding of the physiochemical relationships that governed shell formation. From Figure 2A and 2B, we see that shells with diameters of up to 3 µm has formed when aniline and 2,6-DAP were functionalized onto the surface of the QDs. Shells are not formed with 2,6-DAB as shown in Figure 2C. This demonstrates that aromaticity is important, but the presence of nitrogen is critical to shell formation. 2,6-DAB does not form shells despite having an aromatic ring, but rather forms aggregated clusters of NPs. This is typically observed when surfaces are unbound with supporting

molecules or when stabilizing ligands with long organic chains such as octadecylamine are on the NPs[102,169,170].

All the BIP functionalized quantum dots presented in Figure 2 D-F show the resulting shell formations and an average shell sizes of the three BIP ligand functionalized NPs. The shell size distribution was determined using dynamic light scattering of quadruplets of shells formed in LC extracted and diluted in toluene,

Table *5-1*. The diluted sample was also subsequently used for SEM imaging in doublets.

Table 5-1 Table summarizing the mean diameter size by DLS and histogram from image analysis.

Shell by Ligand	Mean diameter size (d.m) by Intensity (DLS)	Mean diameter size (d.nm) by Histogram
BIP-Me	305	283
BIP-H	468	643
BIP-iPr	935	1076

BIP-Me, BIP-H, and BIP-iPr had mean size from DLS measurements of 305 nm, 468 nm, and 935 nm respectively. From the histograms created from the sets of SEM images and measuring diameters of shells via FIJI/ImageJ analysis, the mean sizes for BIP-Me, BIP-H, and BIP-iPr were 283 nm, 643 nm, and 1076 nm respectively. The combination of DLS and SEM confirms the mean size of the shells.

Broken Shells

As shown in Figure *5-3*, we have observed fractured shells that allowed us to determine relative shell wall thickness with respect to overall shell size. In scanning electron microscopy and looking at their inner and out radius, there are wall thicknesses that range for specific diameters as determined from previous work to be 20%. [168] Typically, as the shell diameter increases the shell wall thickness should increase along with it. BIP-Me for example in Figure *5-3*A had a diameter of 616 nm and a wall thickness of 114 nm which is approximately 18% of the shell diameter. BIP-iPr broken shell of 433 nm had a shell wall thickness of 29 nm which is 6% of the diameter. One of the controls, 2,6-DAP, produced a shell diameter of 3.05 microns and a shell wall thickness of 64 nm, 2% of the shell diameter. Based on our findings, the maximum shell thickness is 20% of the shell diameter. From the variations of the different shell sizes, the shell thickness vary based on the shell diameter, and the type of ligand molecule that is adsorbed to the surface of the NPs.

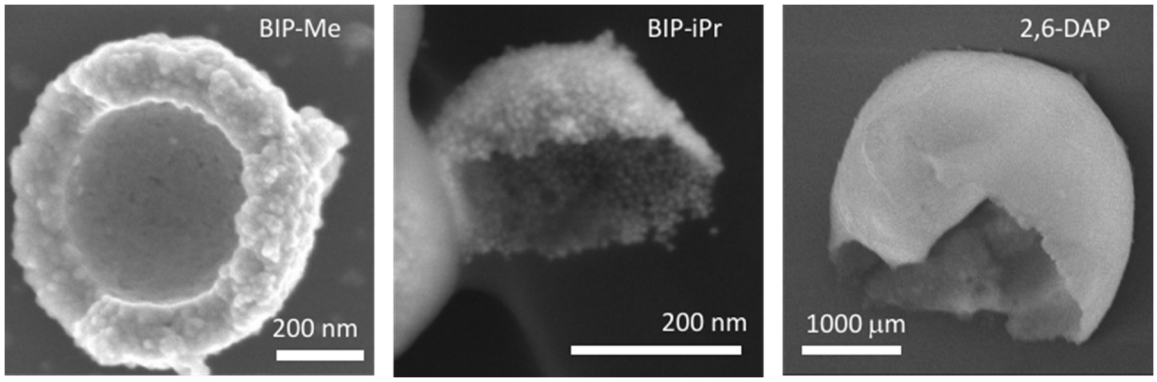

Figure 5-3 SEM images of broken shells for BIP-Me, BIP-iPr, and the control molecule 2,6-DAP.

Consistency in Shell Size

The mean size of the various BIP functionalized shells were compared with Charton values of the alkyl substituents of the BIPs to ascertain a physiochemical relationship between steric parameters and mean shell size, but no such relationship was observable. Due to the self-assembly process in 5CB being governed by thermodynamic equilibrium, further investigation of the polydispersity allowed for a weighted ratio to be calculated between the predominant population ranges divided by the product of the minority populations to serve as a proxy for an equilibrium constant. The natural log of the equilibrium constant was taken and compared to the polydispersity range of shell formation and linearity was observed as shown in Figure 5-4A. The linearity of the natural log of the equilibrium constant compared to the polydispersity of the shell sizes implies ligand functionalization was having a fundamental effect on the thermodynamics associated with shell formation, however this relationship could not be attributed n to traditional steric effects. While evidence supported a free energy relationship between the ligands and the self-assembly process the lack of a relationship to any physiochemical property (lattice dimensions, torsional angles, sterics, lattice volumes) led to the investigation of the thermodynamic effect of the ligands on the mesogenic host 5CB.

With well-documented precedence for the assembly process taking place at the isotropic-nematic phase transition, the effect of the BIP ligands on the enthalpy of phase transition of 5CB at various BIP weight percentages was explored using differential scanning calorimetry (DSC) as seen in Figure 5-4B. It was found that the BIPs exhibited a depression of the phase transition temperature proportional to the observed polydispersity. As a qualitative check the natural log of the previously calculated equilibrium constant was

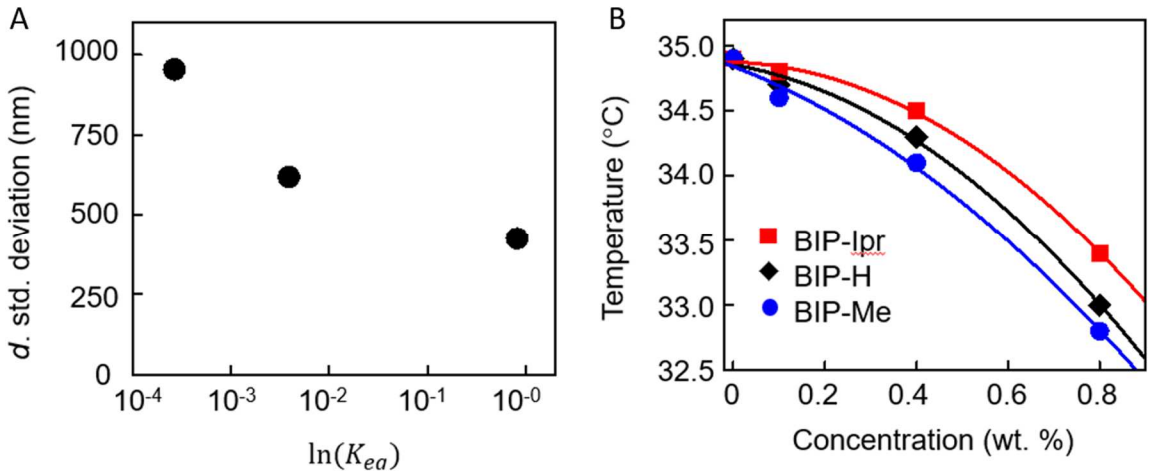

Figure 5-4 (A) Shell size versus the linear free energy relation of the BIP molecules. (B) Thermotropic phase transition temperature of the liquid crystal versus BIP concentration increases.

compared to the enthalpy terms derived from integration of the endotherms in the DSC curves. Linearity was observed indicating that these two terms, equilibrium constant and the change in enthalpy of the isotropic to nematic phase transition, (l⍰(K_{eq}) and $\Delta H_{Isotropic-Nematic}$), were related. This relationship between the free energy of formation and the enthalpy of phase transition provides evidence of the significant impact thermodynamic properties of mesogenic hosts have on the self-assembly process of non-mesogenic guests representing an often overlooked aspect of these systems.

The mean shell size for each BIP molecule is consistent and can be considered a product of the change of free energy as a function of radius. When the assemblage of the BIP-CZ nanoparticles reaches a certain size that is most thermodynamically favorable, the structure stabilizes to complete the formation of the 3-dimensional shells.

Modeling

A theoretical model has previously been developed to describe the phase behavior of mesogenic ligands. [166] During the shell formation process, the shell wall is a boundary between the nematic (N) phase outside and the isotropic phase (I) inside. This boundary, or front, has an effective pressure P_{IN} associated with it that serves as the driving force. The speed at which this front progresses is proportional to P_{IN}, which in turn varies linearly [171] with the free energy difference δf_{IN} between the two homogenous phases, leading to:

$$P_{IN} = \delta f_{IN}$$

The effective pressure additionally creates a compressive stress γ in the shell, which can be expressed as:

$$\gamma = R_S P_{IN}/2$$

where R_S is the shell radius. As shell formation progresses, the insertion of each additional NP to the shell wall has an energy cost δG_P associated with it, which can be expressed as:

$$\delta G_P t_S = \gamma$$

where t_S is the shell thickness. Combining these equations, the shell radius is:

$$R_S = 2t_S \left({}^{\delta G_P}/_{\delta f_{IN}} \right)$$

The energy cost δG_P is dominated by the NP properties, rather than the ligands, but δf_{IN} defined as the change in free energy between the N and I phases, is directly proportional to T_{IN}, the thermotropic transition temperature. [172] Therefore, lower the value of T_{IN} the larger the value of R_S where the shell structure will stabilize.

As an aside, some of the shell structures have formed bead like structures and this is similar to other works that formed helical structures[17]. In which case colloidal nanoparticles were grafted/functionalized with mesogenic ligands that were known to form helical nanofilaments. A helical structure is formed from a thin film of thermotropic liquid crystal doped with the mesogenic ligand grafted gold nanoparticles during phase transition. Although the BIP ligands have not been found to create helical structures, there were occasions where bead like structures of shells would form, interconnecting shells with nanoparticles. Here, there may be similarity in the two in that during the phase transition, at some nucleation point, interconnected shells can form bead like structures using BIP-NPs as shown in *Figure 5-5*.

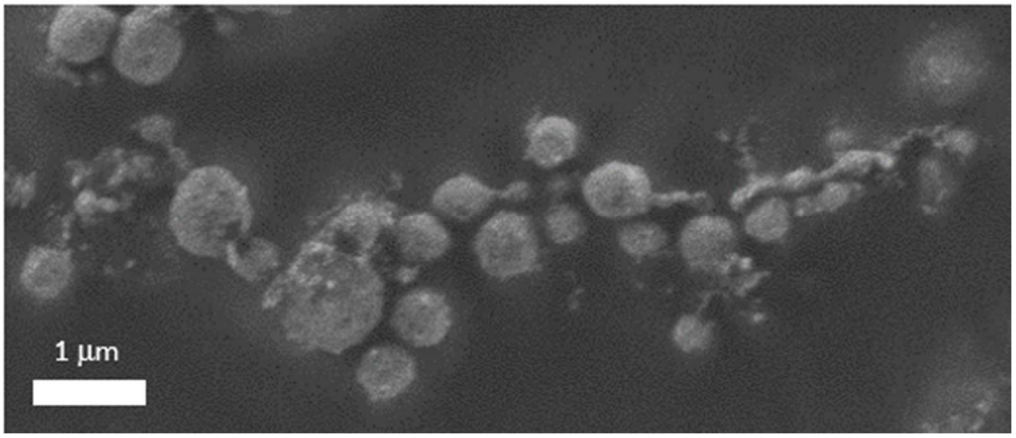

Figure 5-5 Bead like arrangement of shells with BIP-Me.

Methods

Ligand Synthesis

Ligands were synthesized via published methodology. See citation [136] for explicit details.

Ligand exchange process

ODA-capped CdSe/ZnS QDs CZ640 were purchased from NN-Labs. CZ640 QDs have a core diameter of 4.8 nm (5–10% size inhomogeneity). Their surfaces were modified using BIP-H, BIP-Me, and BIP-Ipr. Surface exchange was carried out under inert conditions by adding the QDs to a hexane solution containing an excess of the modifying ligands relative to the native ODA. This solution is incubated for at least 5 min and then purified with acetonitrile (MeCN) and chloroform ($CHCl_3$). The QDs are then separated by centrifugation and redispersed in toluene.

Shell formation protocol

A 1.5 mL microcentrifuge tube (mct) was filled with 20 uL of 5CB (Sigma Aldrich) and mixed with 20 µL of BIP functionalized CdSe/ZnS (CZ640) quantum dots (NN Labs) that were diluted to 0.5 mg/mL in toluene. The BIP-QD-LC mixture is sonicated and heated and maintained at 50 °C in a sonication bath for a minimum of 5 hours to obtain complete NP dispersion within the LC medium. Then the mct is cooled from the heated bath onto a room temperature copper block in which the formation of the shells occurs from isotropic to nematic phases of the LC.

Dynamic light scattering

Preparation for dynamic and light scattering (DLS) was done after cooling the QD-LC mixture. Quadruplets of BIP-QD shells in 1.5 mL microcentrifuge tubes are mixed with 40 µL $CHCl_3$ and centrifuged for 10 minutes at 6k rpm. The aliquot is removed, redispersed in CHCl3 for a second centrifugation, and redispersed in 250 µL of toluene by sonication. The 4 solutions are then stored in a 2.5 mL vial totaling 1 mL of shells in toluene. A Malvern Zetasizer Pro was used to conduct DLS at 40 °C.

Scanning electron microscopy

From one of the microcentrifuge tube or the 1 mL vial of quadruplet samples in preparation for dynamic light scattering, 2 µL is pipetted on a TEM grid held by a tweezer or on carbon tape placed on SEM pin stub mount. Samples are created in doublets and are then vacuumed and heated in an oven at 40 °C for drying.

Image Analysis (FIJI/ImageJ)

In parallel to DLS measurements, image analysis of the shell sizes were done with FIJI to determine an average size distribution for each BIP functionalized QD shell structures.

Conclusion

While the advancement of technology continues to rely on the development of increasingly complex structures on decreasing length scales, understanding of self-assembling systems is becoming critical. We have presented strong evidence that modulation of the enthalpy associated with the isotropic to nematic phase transition of 5CB has a significant impact on the self-assembly process. The surface chemistry of semiconducting nanoparticles were modified to be capable of self-assembling into spherical shell structures with 5CB liquid crystal as a template. The surface morphologies of the shells were observed under SEM, with average shell sizes confirmed via DLS. Thermodynamic relationships were generated between BIP ligands and both shell size polydispersity and phase transition of 5CB to assess the effect of ligand functionalization on both polydispersity and depression of phase transition temperature the mesogenic host. This relationship produces the first evidence of the thermodynamic control of hierarchical structure formation through modulating the thermodynamics associated with phase transitions of mesogenic host-based assembly systems.

The possible self-assembly pathway was modeled under thermodynamic constraints to approximate shell formation. This study furthers the understanding of self-assembling systems and the use of host-guest interactions for tuning the self-assembly process by both increasing and decreasing the aggregate population of hierarchal structures formed. This type of understanding will serve to enhance a broad range of various applications in which precision engineering on the sub-micron length scale is critical.

Acknowledgements

The work was done in collaboration with Dr. Ryan Baxter and Ryan Brisbin who synthesized the custom designed bis(imino)pyradine ligands. This work is based upon work supported by the National Science Foundation under grant nos. NSF-CAREER 1752821 (R.D.B.) and NSF-CREST HRD-1547848 (S.G., M.D.B., and R.P.

Chapter 6 Discussion/Conclusion

In this dissertation, the work done demonstrated that co-assembled magnetic nanoparticles and quantum dots have a synergistic effect on photoluminescence enhancement with applied magnetic field in the milli-Tesla range. In addition, surface functionalization of nanoparticles with aromatic ligands is a viable way of creating electro responsive, non-toxic, and functional self-assembly of quantum dots into shell structures.

Self-assembling co-assembled nanoparticles, namely, quantum dots and magnetic nanoparticles were investigated to show synergistic effects that allowed for magnetic field sensing in the milli-Tesla range. Normally, photoluminescence enhancement would not occur unless a large magnetic field of 10 Tesla is applied to only quantum dots. The synergy between the magnetic nanoparticles and the quantum dots provides some insight into how enhancing the photoluminescence of QDs can be done with local neighboring magnetic nanoparticles.

CdSe/ZnS quantum dots had their native ligands, octadecylamine, were surface functionalized with electroactive molecules (ligands) to allow the tuning of heterogenous charge transfer that open pathways into the energy industry. In addition, the ligands were also multi-functional by assisting in the formation of superstructures, spherical sub-micro-structures to provide a proof-of-concept of encapsulating cargo such as drugs or protein.

The research recognized that functionalizing with bis(imino)pyridine gave way to a robust structure and a way to rupture the shell by alternative actuation methods. Laser light was one of the main actuation methods, however, electric potential can possibly be done which can lead to an effective method for drug delivery, electrodynamic therapy, or tissue engineering repair applications. To determine the morphology of the assembled sub-micro-structures, a combination of optical spectroscopy and both optical & electron microscopy were utilized to characterize the material for potential use cases in magnetic sensing and cargo delivery systems. Surface characterization was done by electrochemistry, utilizing cyclic voltammetry to probe the characteristic features of the BIP molecules and a QD-BIP feature. This was noticed by recognizing the free BIP signatures in solution versus a noticeable but adjusted signature when probing the QD-BIP solution without free BIP ligands.

By utilizing functional molecules like bis(imino)pyridine to alter the properties of quantum dots, for example, enable them to function in ways that they were initially unintended to. With the right type of molecular features for molecules used in surface functionalization, the applications for nanoparticles can vary from LEDs to biocompatible products for drug delivery.

Next steps and future work

For the magnetic sensor platform, a device may be developed to build a low-cost device that can be calibrated to output magnetic field strength. This magnetic sensor should respond to a small range of magnetic fields (0-100 mT) by reading the intensity as input that the magnetic and quantum dot cluster emit when under an applied magnetic field and output the magnetic field strength.

For the quantum dot BIP systems, there maybe be further investigations in electronic heterostructures for more efficient charge transfer in applications such as quantum dot solar cells or LEDs. These types of devices need improvement in terms of charge transfer capabilities. Since BIP molecules seem to be great hole acceptors, a molecule that could be closer to the conduction band and be a great photogenerated electron acceptor, then creating a system that can propagate electrons and holes efficiently to their respective anode and cathodes would be worth trying.

The shell platform can be extended to make sure that a shell structure is nontoxic to a biological system. There are a few steps that need to be met, first, is changing the self-assembly template of 5CB to some other liquid crystal that is biocompatible. 5CB is toxic in a biological setting and would need to find a biocompatible replacement for shell assembly. Considering that when encapsulation would come included with the host liquid crystal when creating the shells. Second, changing the nanoparticle to gold or silver for their inert properties relative to a biological system. The BIP molecules would also need to have a solution-based protocol to adsorb to metallic nanoparticles such as gold nanoparticles to observe whether shell rupturing may occur when illuminated with laser light. Third, cell specificity by adding a molecule to the surface of the shell structure to target and bind to cancer cells. For cancer therapy, the surface of shells would need to additionally have the capability of cancer cell targeting for specificity.

Additionally, if it were to be included in tissue engineering, there are a couple of experiments that may be worth testing. The nano-assembled shells could be included within the mixture of cells, fibrin matrix, and pericytes in a microfluidic device with growth factors being perfused into the mixture. If it disrupts the growth, then wait until growth happens and see if it collapses the tissue network just by being included in stasis within the tissue network. If it does not, then see what happens when the shells are ruptured within a grown tissue network and observe whether it collapses the tissue network. If all is well from here, then try feeding a different type of cell by rupturing shells encapsulating a different type of cell to try to form a patterning of cells within an already growing tissue network. In this case, it is the observation of whether if there may be a switch between cell types that grow within the tissue network. This is based on the concept of being able to change a cell's behavior based on signaling between cells. This patterning of cells may lead to a novel method of understanding how to properly layer tissue cells or disrupt them.

Extending and confirming electric potential rupturing of the shell can be investigated since BIP molecules are electroactive. Seeing the characteristic BIP features in cyclic voltammetry measurements and the charge transfer capabilities of the BIP molecules when interacting metallic and semiconducting substrates, developing an experimental setup that allows a thin film of the QD Shells to be exposed to a linear increase of electric potential to determine the rupture or critical threshold it can withstand in terms of voltage would provide insight into whether it is a feasible system to work with as an encapsulation and release method. Since the BIP ligands result in much smaller shells compared to their predecessors, greater magnification and resolving power in terms of imaging and characterization methods will have to be developed to record and observe the rupture occurring in real time while either optically excited, heated or under an applied electric potential.

One last note, if we were to go with a different approach rather than working with an encapsulation method requiring multiple nanoparticles to form a shell, the BIP molecules could be attempted to be surface functionalized onto mesoporous nanoparticles. Test to see if there is a pathway or route to electroactively increase the size of mesoporous shells with ligand interactions so that encapsulated molecules, drugs or proteins, are released instead of using heat.

References

1. Tripathi, R.M., and Chung, S.J. (2019) Biogenic nanomaterials: Synthesis, characterization, growth mechanism, and biomedical applications. *J. Microbiol. Methods*, **157**, 65–80.
2. Fernandes, R.J.C., Magalhães, C.A.B., Amorim, C.O., Amaral, V.S., Almeida, B.G., Castanheira, E.M.S., and Coutinho, P.J.G. (2019) Magnetic Nanoparticles of Zinc/Calcium Ferrite Decorated with Silver for Photodegradation of Dyes. *Materials (Basel).*, **12** (21), 3582.
3. Sanità, G., Carrese, B., and Lamberti, A. (2020) Nanoparticle Surface Functionalization: How to Improve Biocompatibility and Cellular Internalization. *Front. Mol. Biosci.*, **7**, 381.
4. Abdelkhaliq, A., Van Der Zande, M., Punt, A., Helsdingen, R., Boeren, S., Vervoort, J.J.M., Rietjens, I.M.C.M., and Bouwmeester, H. (2018) Impact of nanoparticle surface functionalization on the protein corona and cellular adhesion, uptake and transport 03 Chemical Sciences 0306 Physical Chemistry (incl. Structural). *J. Nanobiotechnology*, **16** (1), 70.
5. Jeevanandam, J., Barhoum, A., Chan, Y.S., Dufresne, A., and Danquah, M.K. (2018) Review on nanoparticles and nanostructured materials: history, sources, toxicity and regulations. *Beilstein J. Nanotechnol.*, **9**, 1050–1074.
6. Chuang, C.H.M., Brown, P.R., Bulović, V., and Bawendi, M.G. (2014) Improved performance and stability in quantum dot solar cells through band alignment engineering. *Nat. Mater.*, **13** (8), 796–801.
7. Choi, M.J., García de Arquer, F.P., Proppe, A.H., Seifitokaldani, A., Choi, J., Kim, J., Baek, S.W., Liu, M., Sun, B., Biondi, M., Scheffel, B., Walters, G., Nam, D.H., Jo, J.W., Ouellette, O., Voznyy, O., Hoogland, S., Kelley, S.O., Jung, Y.S., and Sargent, E.H. (2020) Cascade surface modification of colloidal quantum dot inks enables efficient bulk homojunction photovoltaics. *Nat. Commun.*, **11** (1), 1–9.
8. Bilan, R., Fleury, F., Nabiev, I., and Sukhanova, A. (2015) Quantum dot surface chemistry and functionalization for cell targeting and imaging. *Bioconjug. Chem.*, **26** (4), 609–624.
9. Khan, S.A., Smith, G.T., Seo, F., and Ellerbee, A.K. (2015) Label-free and non-contact optical biosensing of glucose with quantum dots. *Biosens. Bioelectron.*, **64**, 30–35.
10. Livache, C., Martinez, B., Goubet, N., Gréboval, C., Qu, J., Chu, A., Royer, S., Ithurria, S., Silly, M.G., Dubertret, B., and Lhuillier, E. (2019) A colloidal quantum dot infrared photodetector and its use for intraband detection. *Nat. Commun.*, **10** (1), 1–10.
11. Yang, Z., Song, J., Dai, Y., Chen, J., Wang, F., Lin, L., Liu, Y., Zhang, F., Yu, G., Zhou, Z., Fan, W., Huang, W., Fan, Q., and Chen, X. (2017) Self-assembly of

semiconducting-plasmonic gold nanoparticles with enhanced optical property for photoacoustic imaging and photothermal therapy. *Theranostics*, **7** (8), 2177–2185.

12. Portela, C.M., Vidyasagar, A., Krödel, S., Weissenbach, T., Yee, D.W., Greer, J.R., and Kochmann, D.M. (2020) Extreme mechanical resilience of self-assembled nanolabyrinthine materials. *Proc. Natl. Acad. Sci. U. S. A.*, **117** (11), 5686–5693.

13. Zhong, K., Song, K., and Clays, K. (2018) Hollow spheres: Crucial building blocks for novel nanostructures and nanophotonics. *Nanophotonics*, **7** (4), 693–713.

14. Taheri, S.M., Michaelis, M., Friedrich, T., Förster, B., Drechsler, M., Römer, F.M., Bösecke, P., Narayanan, T., Weber, B., Rehberg, I., Rosenfeldt, S., and Förster, S. (2015) Self-assembly of smallest magnetic particles. *Proc. Natl. Acad. Sci. U. S. A.*, **112** (47), 14484–14489.

15. Amabilino, D.B., Smith, D.K., and Steed, J.W. (2017) Supramolecular materials. *Chem. Soc. Rev.*, **46** (9), 2404–2420.

16. Gangula, A., Chelli, J., Bukka, S., Poonthiyil, V., Podila, R., Kannan, R., and Rao, A.M. (2012) Thione-gold nanoparticles interactions: Vroman-like effect, self-assembly and sensing. *J. Mater. Chem.*, **22** (43), 22866–22872.

17. Bagiński, M., Tupikowska, M., González□Rubio, G., Wójcik, M., and Lewandowski, W. (2020) Shaping Liquid Crystals with Gold Nanoparticles: Helical Assemblies with Tunable and Hierarchical Structures Via Thin□Film Cooperative Interactions. *Adv. Mater.*, **32** (1), 1904581.

18. Keshavarz, A., Riahinasab, S.T., Hirst, L.S., and Stokes, B.J. (2019) New Promesogenic Ligands for Host Medium Microencapsulation by Quantum Dots via Liquid Crystal Phase Transition Templating. *ACS Appl. Nano Mater.*, **2** (4), 2542–2547.

19. Yu, S., Tang, Y., Li, Z., Chen, K., Ding, X., and Yu, B. (2018) Enhanced optical and thermal performance of white light-emitting diodes with horizontally layered quantum dots phosphor nanocomposites. *Photonics Res.*, **6** (2), 90.

20. Markwalter, C.E., Pagels, R.F., Hejazi, A.N., Gordon, A.G.R., Thompson, A.L., and Prud'homme, R.K. (2020) Polymeric Nanocarrier Formulations of Biologics Using Inverse Flash NanoPrecipitation. *AAPS J.*, **22** (2), 18.

21. Deng, Y., Zhang, X., Shen, H., He, Q., Wu, Z., Liao, W., and Yuan, M. (2020) Application of the Nano-Drug Delivery System in Treatment of Cardiovascular Diseases. *Front. Bioeng. Biotechnol.*, **7**, 489.

22. Patra, J.K., Das, G., Fraceto, L.F., Campos, E.V.R., Rodriguez-Torres, M.D.P., Acosta-Torres, L.S., Diaz-Torres, L.A., Grillo, R., Swamy, M.K., Sharma, S., Habtemariam, S., and Shin, H.S. (2018) Nano based drug delivery systems: Recent developments and future prospects 10 Technology 1007 Nanotechnology 03 Chemical Sciences 0306 Physical Chemistry (incl. Structural) 03 Chemical

Sciences 0303 Macromolecular and Materials Chemistry 11 Medical and Health Sciences 1115 Pharmacology and Pharmaceutical Sciences 09 Engineering 0903 Biomedical Engineering Prof Ueli Aebi, Prof Peter Gehr. *J. Nanobiotechnology*, **16** (1), 1–33.

23. Claridge, S.A., Castleman, A.W., Khanna, S.N., Murray, C.B., Sen, A., and Weiss, P.S. (2009) Cluster-Assembled Materials. *ACS Nano*, **3** (2), 244–255.

24. Josten, E., Wetterskog, E., Glavic, A., Boesecke, P., Feoktystov, A., Brauweiler-Reuters, E., Rücker, U., Salazar-Alvarez, G., Brückel, T., and Bergstrm, L. (2017) Superlattice growth and rearrangement during evaporation-induced nanoparticle self-assembly. *Sci. Rep.*, **7** (1), 1–9.

25. Ye, X., Zhu, C., Ercius, P., Raja, S.N., He, B., Jones, M.R., Hauwiller, M.R., Liu, Y., Xu, T., and Alivisatos, A.P. (2015) Structural diversity in binary superlattices self-assembled from polymer-grafted nanocrystals. *Nat. Commun.*, **6** (1), 1–10.

26. Si, K.J., Chen, Y., Shi, Q., and Cheng, W. (2018) Nanoparticle Superlattices: The Roles of Soft Ligands. *Adv. Sci.*, **5** (1), 1700179.

27. Schulz, F., Pavelka, O., Lehmkühler, F., Westermeier, F., Okamura, Y., Mueller, N.S., Reich, S., and Lange, H. (2020) Structural order in plasmonic superlattices. *Nat. Commun.*, **11** (1), 1–9.

28. Scheeler, S.P., Mühlig, S., Rockstuhl, C., Hasan, S. Bin, Ullrich, S., Neubrech, F., Kudera, S., and Pacholski, C. (2013) Plasmon coupling in self-assembled gold nanoparticle-based honeycomb islands. *J. Phys. Chem. C*, **117** (36), 18634–18641.

29. Chen, Y., Liu, H., Yin, H., Zhu, Q., Yao, G., and Gu, N. (2020) Hierarchical Fabrication of Plasmonic Superlattice Membrane by Aspect-Ratio Controllable Nanobricks for Label-Free Protein Detection. *Front. Chem.*, **8**, 307.

30. Chu, Y.H., Martin, L.W., Holcomb, M.B., Gajek, M., Han, S.J., He, Q., Balke, N., Yang, C.H., Lee, D., Hu, W., Zhan, Q., Yang, P.L., Fraile-Rodríguez, A., Scholl, A., Wang, S.X., and Ramesh, R. (2008) Electric-field control of local ferromagnetism using a magnetoelectric multiferroic. *Nat. Mater.*, **7** (6), 478–482.

31. Zhou, X., Zhou, Y., Ku, J.C., Zhang, C., and Mirkin, C.A. (2014) Capillary force-driven, large-area alignment of multi-segmented nanowires. *ACS Nano*, **8** (2), 1511–1516.

32. Vila□Liarte, D., Feil, M.W., Manzi, A., Garcia□Pomar, J.L., Huang, H., Döblinger, M., Liz□Marzán, L.M., Feldmann, J., Polavarapu, L., and Mihi, A. (2020) Templated□Assembly of $CsPbBr_3$ Perovskite Nanocrystals into 2D Photonic Supercrystals with Amplified Spontaneous Emission. *Angew. Chemie Int. Ed.*, **59** (40), 17750–17756.

33. Rodarte, A.L., Cao, B.H., Panesar, H., Pandolfi, R.J., Quint, M., Edwards, L., Ghosh, S., Hein, J.E., and Hirst, L.S. (2015) Self-assembled nanoparticle micro-shells templated by liquid crystal sorting. *Soft Matter*, **11** (9), 1701–1707.

34. Weller, T., Deilmann, L., Timm, J., Dörr, T.S., Beaucage, P.A., Cherevan, A.S.,

Wiesner, U.B., Eder, D., and Marschall, R. (2018) A crystalline and 3D periodically ordered mesoporous quaternary semiconductor for photocatalytic hydrogen generation. *Nanoscale*, **10** (7), 3225–3234.

35. Ghosh, S.K., and Böker, A. (2019) Self□Assembly of Nanoparticles in 2D and 3D: Recent Advances and Future Trends. *Macromol. Chem. Phys.*, **220** (17), 1900196.

36. Jain, A., Gutmann, J.S., Garcia, C.B.W., Zhang, Y., Tate, M.W., Gruner, S.M., and Wiesner, U. (2002) Effect of Filler Dimensionality on the Order−Disorder Transition of a Model Block Copolymer Nanocomposite. *Macromolecules*, **35** (13), 4862–4865.

37. Jia, L., Wang, R., and Fan, Y. (2020) Encapsulation and release of drug nanoparticles in functional polymeric vesicles. *Soft Matter*, **16** (12), 3088–3095.

38. Xiao, D., Jia, H.-Z., Zhang, J., Liu, C.-W., Zhuo, R.-X., and Zhang, X.-Z. (2014) A Dual-Responsive Mesoporous Silica Nanoparticle for Tumor-Triggered Targeting Drug Delivery. *Small*, **10** (3), 591–598.

39. Taniguchi, S., Sandiford, L., Cooper, M., Rosca, E. V., Ahmad Khanbeigi, R., Fairclough, S.M., Thanou, M., Dailey, L.A., Wohlleben, W., Von Vacano, B., TMDe Rosales, R., Dobson, P.J., Owen, D.M., and Green, M. (2016) Hydrophobin-Encapsulated Quantum Dots. *ACS Appl. Mater. Interfaces*, **8** (7), 4887–4893.

40. Dang, Y., and Guan, J. (2020) Nanoparticle-based drug delivery systems for cancer therapy. *Smart Mater. Med.*, **1**, 10–19.

41. Rizvi, S.A.A., and Saleh, A.M. (2018) Applications of nanoparticle systems in drug delivery technology. *Saudi Pharm. J.*, **26** (1), 64–70.

42. Adeel, M., Duzagac, F., Canzonieri, V., and Rizzolio, F. (2020) Self-Therapeutic Nanomaterials for Cancer Therapy: A Review. *ACS Appl. Nano Mater.*, **3** (6), 4962–4971.

43. Yang, H., Liu, Y., Qiu, Y., Ding, M., and Zhang, Y. (2019) MiRNA-204-5p and oxaliplatin-loaded silica nanoparticles for enhanced tumor suppression effect in CD44-overexpressed colon adenocarcinoma. *Int. J. Pharm.*, **566**, 585–593.

44. Jiang, Y., Huo, S., Mizuhara, T., Das, R., Lee, Y.W., Hou, S., Moyano, D.F., Duncan, B., Liang, X.J., and Rotello, V.M. (2015) The Interplay of Size and Surface Functionality on the Cellular Uptake of Sub-10 nm Gold Nanoparticles. *ACS Nano*, **9** (10), 9986–9993.

45. Huschka, R., Neumann, O., Barhoumi, A., and Halas, N.J. (2010) Visualizing Light-Triggered Release of Molecules Inside Living Cells. *Nano Lett.*, **10** (10), 4117–4122.

46. Croissant, J., and Zink, J.I. (2012) Nanovalve-Controlled Cargo Release Activated by Plasmonic Heating. *J. Am. Chem. Soc.*, **134** (18), 7628–7631.

47. (2013) Sub-100 nm Gold Nanoparticle Vesicles as a Drug Delivery Carrier

enabling Rapid Drug Release upon Light Irradiation. *ACS Appl. Mater. Interfaces*, **5** (9), 3900–3907.

48. Maier, S.A. (2007) *American National Standard for Safe Use of Lasers: ANSI Z136.1-2000*, Laser Institute of America.

49. De Gracia Lux, C., Joshi-Barr, S., Nguyen, T., Mahmoud, E., Schopf, E., Fomina, N., and Almutairi, A. (2012) Biocompatible polymeric nanoparticles degrade and release cargo in response to biologically relevant levels of hydrogen peroxide. *J. Am. Chem. Soc.*, **134** (38), 15758–15764.

50. Lombardo, D., Kiselev, M.A., and Caccamo, M.T. (2019) Smart Nanoparticles for Drug Delivery Application: Development of Versatile Nanocarrier Platforms in Biotechnology and Nanomedicine.

51. Ren, Q., Ga, L., Lu, Z., Ai, J., and Wang, T. (2020) Aptamer-functionalized nanomaterials for biological applications. *Mater. Chem. Front.*

52. Thiruppathi, R., Mishra, S., Ganapathy, M., Padmanabhan, P., and Gulyás, B. (2017) Nanoparticle Functionalization and Its Potentials for Molecular Imaging. *Adv. Sci.*, **4** (3), 1600279.

53. Khan, I., Saeed, K., and Khan, I. (2019) Nanoparticles: Properties, applications and toxicities. *Arab. J. Chem.*, **12** (7), 908–931.

54. Tsai, C.-Y., Lu, S.-L., Hu, C.-W., Yeh, C.-S., Lee, G.-B., and Lei, H.-Y. (2012) Size-Dependent Attenuation of TLR9 Signaling by Gold Nanoparticles in Macrophages. *J. Immunol.*, **188** (1), 68–76.

55. Barar, J. (2015) Bioimpacts of nanoparticle size: why it matters? *Bioimpacts*, **5** (3), 113–5.

56. Michael Wahl (2014) The Principle of Time-Correlated Single Photon Counting.

57. Sarang, S., Ishihara, H., Chen, Y.C., Lin, O., Gopinathan, A., Tung, V.C., and Ghosh, S. (2016) Low temperature excitonic spectroscopy and dynamics as a probe of quality in hybrid perovskite thin films. *Phys. Chem. Chem. Phys.*, **18** (41), 28428–28433.

58. Cerne, J. Magneto-Polarimetry Advanced Lab.

59. Haider, T. (2017) A Review of Magneto-Optic Effects and Its Application. *Int. J. Electromagn. Appl.*, **7** (1), 17–24.

60. Shoji, Y., and Mizumoto, T. (2019) Silicon waveguide optical isolator with directly bonded magneto-optical garnet. *Appl. Sci.*, **9** (3), 609.

61. Višňnovský, Š. (2018) Magnetooptics in cylindrical structures. *Appl. Sci.*, **8** (12), 2547.

62. Goldstein, J.I., Newbury, D.E., Echlin, P., Joy, D.C., Lyman, C.E., Lifshin, E., Sawyer, L., and Michael, J.R. (2003) *Scanning Electron Microscopy and X-ray Microanalysis*, Springer US, Boston, MA.

63. Scanning Electron Microscopy (SEM) – PhotoMetrics.

64. Ellis, B., Mayer, M.A., Shambat, G., Sarmiento, T., Harris, J., Haller, E.E., and Vučković, J. (2011) Ultralow-threshold electrically pumped quantum-dot photonic-crystal nanocavity laser. *Nat. Photonics*, **5** (5), 297–300.

65. Chen, S., Li, W., Wu, J., Jiang, Q., Tang, M., Shutts, S., Elliott, S.N., Sobiesierski, A., Seeds, A.J., Ross, I., Smowton, P.M., and Liu, H. (2016) Electrically pumped continuous-wave III–V quantum dot lasers on silicon. *Nat. Photonics*, **10** (5), 307–311.

66. Du, J., Zhang, M., Guo, Z., Chen, J., Zhu, X., Hu, G., Peng, P., Zheng, Z., and Zhang, H. (2017) Phosphorene quantum dot saturable absorbers for ultrafast fiber lasers. *Sci. Rep.*, **7** (1), 42357.

67. Dai, X., Deng, Y., Peng, X., and Jin, Y. (2017) Quantum-Dot Light-Emitting Diodes for Large-Area Displays: Towards the Dawn of Commercialization. *Adv. Mater.*, **29** (14), 1607022.

68. Song, J., Li, J., Li, X., Xu, L., Dong, Y., and Zeng, H. (2015) Quantum Dot Light-Emitting Diodes Based on Inorganic Perovskite Cesium Lead Halides ($CsPbX_3$). *Adv. Mater.*, **27** (44), 7162–7167.

69. Kwak, J., Bae, W.K., Lee, D., Park, I., Lim, J., Park, M., Cho, H., Woo, H., Yoon, D.Y., Char, K., Lee, S., and Lee, C. (2012) Bright and Efficient Full-Color Colloidal Quantum Dot Light-Emitting Diodes Using an Inverted Device Structure. *Nano Lett.*, **12** (5), 2362–2366.

70. Yang, Z., Janmohamed, A., Lan, X., García de Arquer, F.P., Voznyy, O., Yassitepe, E., Kim, G.-H., Ning, Z., Gong, X., Comin, R., and Sargent, E.H. (2015) Colloidal Quantum Dot Photovoltaics Enhanced by Perovskite Shelling. *Nano Lett.*, **15** (11), 7539–7543.

71. Yuan, M., Liu, M., and Sargent, E.H. (2016) Colloidal quantum dot solids for solution-processed solar cells. *Nat. Energy*, **1** (3), 16016.

72. Arinze, E.S., Qiu, B., Nyirjesy, G., and Thon, S.M. (2016) Plasmonic Nanoparticle Enhancement of Solution-Processed Solar Cells: Practical Limits and Opportunities. *ACS Photonics*, **3** (2), 158–173.

73. Reineck, P., Brick, D., Mulvaney, P., and Bach, U. (2016) Plasmonic Hot Electron Solar Cells: The Effect of Nanoparticle Size on Quantum Efficiency. *J. Phys. Chem. Lett.*, **7** (20), 4137–4141.

74. Chuang, M.-K., Lin, S.-W., Chen, F.-C., Chu, C.-W., and Hsu, C.-S. (2014) Gold nanoparticle-decorated graphene oxides for plasmonic-enhanced polymer photovoltaic devices. *Nanoscale*, **6** (3), 1573–1579.

75. Li, Y., Zhu, J., Huang, Y., Liu, F., Lv, M., Chen, S., Hu, L., Tang, J., Yao, J., and Dai, S. (2015) Mesoporous SnO_2 nanoparticle films as electron-transporting material in perovskite solar cells. *RSC Adv.*, **5** (36), 28424–28429.

76. Zhukovsky, S. V., Babicheva, V.E., Uskov, A. V., Protsenko, I.E., and

Lavrinenko, A. V. (2014) Enhanced Electron Photoemission by Collective Lattice Resonances in Plasmonic Nanoparticle-Array Photodetectors and Solar Cells. *Plasmonics*, **9** (2), 283–289.

77. Liu, B., Wang, Z., Dong, Y., Zhu, Y., Gong, Y., Ran, S., Liu, Z., Xu, J., Xie, Z., Chen, D., and Shen, G. (2012) ZnO-nanoparticle-assembled cloth for flexible photodetectors and recyclable photocatalysts. *J. Mater. Chem.*, **22** (18), 9379.

78. Nasiri, N., Bo, R., Hung, T.F., Roy, V.A.L., Fu, L., and Tricoli, A. (2016) Tunable Band-Selective UV-Photodetectors by 3D Self-Assembly of Heterogeneous Nanoparticle Networks. *Adv. Funct. Mater.*, **26** (40), 7359–7366.

79. Merino, S., Martín, C., Kostarelos, K., Prato, M., and Vázquez, E. (2015) Nanocomposite Hydrogels: 3D Polymer–Nanoparticle Synergies for On-Demand Drug Delivery. *ACS Nano*, **9** (5), 4686–4697.

80. Mura, S., Nicolas, J., and Couvreur, P. (2013) Stimuli-responsive nanocarriers for drug delivery. *Nat. Mater.*, **12** (11), 991–1003.

81. Daniel, M.-C., Grow, M.E., Pan, H., Bednarek, M., Ghann, W.E., Zabetakis, K., and Cornish, J. (2011) Gold nanoparticle-cored poly(propyleneimine) dendrimers as a new platform for multifunctional drug delivery systems. *New J. Chem.*, **35** (10), 2366.

82. Yezhelyev, M.V., Al-Hajj, A., Morris, C., Marcus, A.I., Liu, T., Lewis, M., Cohen, C., Zrazhevskiy, P., Simons, J.W., Rogatko, A., Nie, S., Gao, X., and O'Regan, R.M. (2007) In Situ Molecular Profiling of Breast Cancer Biomarkers with Multicolor Quantum Dots. *Adv. Mater.*, **19** (20), 3146–3151.

83. Liu, J., Lau, S.K., Varma, V.A., Moffitt, R.A., Caldwell, M., Liu, T., Young, A.N., Petros, J.A., Osunkoya, A.O., Krogstad, T., Leyland-Jones, B., Wang, M.D., and Nie, S. (2010) Molecular Mapping of Tumor Heterogeneity on Clinical Tissue Specimens with Multiplexed Quantum Dots. *ACS Nano*, **4** (5), 2755–2765.

84. Thorek, D.L.J., Chen, A.K., Czupryna, J., and Tsourkas, A. (2006) Superparamagnetic Iron Oxide Nanoparticle Probes for Molecular Imaging. *Ann. Biomed. Eng.*, **34** (1), 23–38.

85. Zhang, Y., Zhang, B., Luo, J., Bai, J., and Liu, F. (2013) In vivo tomographic imaging with fluorescence and MRI using tumor-targeted dual-labeled nanoparticles. *Int. J. Nanomedicine*, **9** (1), 33.

86. Foy, S.P., Manthe, R.L., Foy, S.T., Dimitrijevic, S., Krishnamurthy, N., and Labhasetwar, V. (2010) Optical Imaging and Magnetic Field Targeting of Magnetic Nanoparticles in Tumors. *ACS Nano*, **4** (9), 5217–5224.

87. Shevach, M., Fleischer, S., Shapira, A., and Dvir, T. (2014) Gold Nanoparticle-Decellularized Matrix Hybrids for Cardiac Tissue Engineering. *Nano Lett.*, **14** (10), 5792–5796.

88. Saunders, A.E., Shah, P.S., Sigman, M.B., Hanrath, T., Hwang, H.S., Lim, K.T., Johnston, K.P., and Korgel, B.A. (2004) Inverse Opal Nanocrystal Superlattice

Films. **4** (10), 1943–1948.

89. Yoon, B., Luedtke, W.D., Barnett, R.N., Gao, J., Desireddy, A., Conn, B.E., Bigioni, T., and Landman, U. (2014) Hydrogen-bonded structure and mechanical chiral response of a silver nanoparticle superlattice. *Nat. Mater.*, **13** (8), 807–811.

90. Park, J., Zheng, H., Lee, W.C., Geissler, P.L., Rabani, E., and Alivisatos, A.P. (2012) Direct Observation of Nanoparticle Superlattice Formation by Using Liquid Cell Transmission Electron Microscopy. *ACS Nano*, **6** (3), 2078–2085.

91. Wang, D., Yang, A., Hryn, A.J., Schatz, G.C., and Odom, T.W. (2015) Superlattice Plasmons in Hierarchical Au Nanoparticle Arrays. *ACS Photonics*, **2** (12), 1789–1794.

92. Dong, A., Ye, X., Chen, J., and Murray, C.B. (2011) Two-Dimensional Binary and Ternary Nanocrystal Superlattices: The Case of Monolayers and Bilayers. *Nano Lett.*, **11** (4), 1804–1809.

93. Zhang, S., Chen, Y., Lu, B., Liu, J., Shao, J., and Xu, C. (2016) Lithographically-generated 3D lamella layers and their structural color. *Nanoscale*, **8** (17), 9118–9127.

94. Schreiber, R., Do, J., Roller, E.-M., Zhang, T., Schüller, V.J., Nickels, P.C., Feldmann, J., and Liedl, T. (2014) Hierarchical assembly of metal nanoparticles, quantum dots and organic dyes using DNA origami scaffolds. *Nat. Nanotechnol.*, **9** (1), 74–78.

95. Jia, H., Bai, X., Li, N., Yu, L., and Zheng, L. (2011) Siloxane surfactant induced self-assembly of gold nanoparticles and their application to SERS. *CrystEngComm*, **13** (20), 6179.

96. Sperling, R.A., and Parak, W.J. (2010) Surface modification, functionalization and bioconjugation of colloidal inorganic nanoparticles. *Philos. Trans. A. Math. Phys. Eng. Sci.*, **368** (1915), 1333–83.

97. Rodarte, A.L., Pandolfi, R.J., Ghosh, S., and Hirst, L.S. (2013) Quantum dot/liquid crystal composite materials: self-assembly driven by liquid crystal phase transition templating. *J. Mater. Chem. C*, **1** (35), 5527.

98. Yang, J., Banerjee, A., and Guha, S. (2003) Amorphous silicon based photovoltaics - From earth to the "final frontier." *Sol. Energy Mater. Sol. Cells*, **78** (1–4), 597–612.

99. Lin, Y., Zhang, L., Mao, H., Chow, P., Xiao, Y., Baldini, M., Shu, J., and Mao, W.L. (2011) Amorphous Diamond: A High-Pressure Superhard Carbon Allotrope. *Phys. Rev. Lett.*, **107** (17), 175504.

100. Banerjee, A., Baker, L.J., Doye, A., Nord, M., Heath, R.M., Erotokritou, K., Bosworth, D., Barber, Z.H., MacLaren, I., and Hadfield, R.H. (2017) Characterisation of amorphous molybdenum silicide (MoSi) superconducting thin films and nanowires. *Supercond. Sci. Technol.*, **30** (8), 084010.

101. Clark, N.A. (2013) Ferromagnetic ferrofluids. *Nature*, **504** (7479), 229–230.

102. Amaral, J.J., Wan, J., Rodarte, A.L., Ferri, C., Quint, M.T., Pandolfi, R.J., Scheibner, M., Hirst, L.S., and Ghosh, S. (2015) Magnetic field induced quantum dot brightening in liquid crystal synergized magnetic and semiconducting nanoparticle composite assemblies. *Soft Matter*, **11** (2), 255–260.

103. Mouhli, A., Ayeb, H., Othman, T., Fresnais, J., Dupuis, V., Nemitz, I.R., Pendery, J.S., Rosenblatt, C., Sandre, O., and Lacaze, E. (2017) Influence of a dispersion of magnetic and nonmagnetic nanoparticles on the magnetic Fredericksz transition of the liquid crystal 5CB. *Phys. Rev. E*, **96** (1), 012706.

104. Kopčanský, P., Tomašovičová, N., Koneracká, M., Závišová, V., Timko, M., Džarová, A., Šprincová, A., Éber, N., Fodor-Csorba, K., Tóth-Katona, T., Vajda, A., and Jadzyn, J. (2008) Structural changes in the 6CHBT liquid crystal doped with spherical, rodlike, and chainlike magnetic particles. *Phys. Rev. E*, **78** (1), 011702.

105. Prodanov, M.F., Kolosov, M.A., Krivoshey, A.I., Fedoryako, A.P., Yarmolenko, S.N., Semynozhenko, V.P., Goodby, J.W., and Vashchenko, V. V. (2012) Dispersion of magnetic nanoparticles in a polymorphic liquid crystal. *Liq. Cryst.*, **39** (12), 1512–1526.

106. Sutens, B., Swusten, T., Zhong, K., Jochum, J., Van Bael, M., Van der Eycken, E., Brullot, W., Bloemen, M., and Verbiest, T. (2016) Tunability of Size and Magnetic Moment of Iron Oxide Nanoparticles Synthesized by Forced Hydrolysis. *Materials (Basel).*, **9** (7), 554.

107. Sato, K., Robinson, C.C., Suits, J.C., Schnatterly, S.N.J. and S.E., G. A. Osborne, J.C.C. and P.J.S., McCaffery, R.A.S. and A.J., Sato, K., P. Chaudhari, J.J.C. and R.J.G., S. Visnovski, B.K.V.P. and H.R.M., and A. P. Malozemoff, J.P.J. and R.J.G. (1981) Measurement of Magneto-Optical Kerr Effect Using Piezo-Birefringent Modulator. *Jpn. J. Appl. Phys.*, **20** (12), 2403–2409.

108. Moreels, I., Justo, Y., De Geyter, B., Haustraete, K., Martins, J.C., and Hens, Z. (2011) Size-tunable, bright, and stable PbS quantum dots: A surface chemistry study. *ACS Nano*, **5** (3), 2004–2012.

109. Wei, G., Czaplewski, D.A., Lenferink, E.J., Stanev, T.K., Jung, I.W., and Stern, N.P. (2017) Size-tunable Lateral Confinement in Monolayer Semiconductors. *Sci. Rep.*, **7** (1), 1–8.

110. Fan, Q., Biesold□McGee, G. V., Ma, J., Xu, Q., Pan, S., Peng, J., and Lin, Z. (2020) Lead□Free Halide Perovskite Nanocrystals: Crystal Structures, Synthesis, Stabilities, and Optical Properties. *Angew. Chemie Int. Ed.*, **59** (3), 1030–1046.

111. Grotevent, M.J., Hail, C.U., Yakunin, S., Dirin, D.N., Thodkar, K., Borin Barin, G., Guyot□Sionnest, P., Calame, M., Poulikakos, D., Kovalenko, M. V., and Shorubalko, I. (2019) Nanoprinted Quantum Dot–Graphene Photodetectors. *Adv. Opt. Mater.*, **7** (11), 1900019.

112. Sukhovatkin, V., Hinds, S., Brzozowski, L., and Sargent, E.H. (2009) Colloidal quantum-dot photodetectors exploiting multiexciton generation. *Science (80-.).*,

324 (5934), 1542–1544.

113. Cho, C., Song, J.H., Kim, C., Jeong, S., and Lee, J.Y. (2017) Broadband light trapping strategies for quantum-dot photovoltaic cells (>10%) and their issues with the measurement of photovoltaic characteristics. *Sci. Rep.*, **7** (1), 1–9.

114. Tajarrod, N., Rofouei, M.K., Masteri-Farahani, M., and Zadmard, R. (2016) A quantum dot-based fluorescence sensor for sensitive and enzymeless detection of creatinine. *Anal. Methods*, **8** (30), 5911–5920.

115. Brazhnik, K., Sokolova, Z., Baryshnikova, M., Bilan, R., Efimov, A., Nabiev, I., and Sukhanova, A. (2015) Quantum dot-based lab-on-a-bead system for multiplexed detection of free and total prostate-specific antigens in clinical human serum samples. *Nanomedicine Nanotechnology, Biol. Med.*, **11** (5), 1065–1075.

116. Sukhanova, A., Even-Desrumeaux, K., Kisserli, A., Tabary, T., Reveil, B., Millot, J.M., Chames, P., Baty, D., Artemyev, M., Oleinikov, V., Pluot, M., Cohen, J.H.M., and Nabiev, I. (2012) Oriented conjugates of single-domain antibodies and quantum dots: Toward a new generation of ultrasmall diagnostic nanoprobes. *Nanomedicine Nanotechnology, Biol. Med.*, **8** (4), 516–525.

117. Yang, X., Yang, J., Khan, J., Deng, H., Yuan, S., Zhang, J., Xia, Y., Deng, F., Zhou, X., Umar, F., Jin, Z., Song, H., Cheng, C., Sabry, M., and Tang, J. (2020) Hydroiodic Acid Additive Enhanced the Performance and Stability of PbS-QDs Solar Cells via Suppressing Hydroxyl Ligand. *Nano-Micro Lett.*, **12** (1), 1–12.

118. Krivenkov, V., Samokhvalov, P., Zvaigzne, M., Martynov, I., Chistyakov, A., and Nabiev, I. (2018) Ligand-Mediated Photobrightening and Photodarkening of CdSe/ZnS Quantum Dot Ensembles. *J. Phys. Chem. C*, **122** (27), 15761–15771.

119. Zhang, Y., and Clapp, A. (2011) Overview of Stabilizing Ligands for Biocompatible Quantum Dot Nanocrystals. *Sensors*, **11** (12), 11036–11055.

120. Cao, Y., Stavrinadis, A., Lasanta, T., So, D., and Konstantatos, G. (2016) The role of surface passivation for efficient and photostable PbS quantum dot solar cells. *Nat. Energy*, **1** (4), 1–6.

121. Hines, D.A., and Kamat, P. V. (2013) Quantum dot surface chemistry: Ligand effects and electron transfer reactions. *J. Phys. Chem. C*, **117** (27), 14418–14426.

122. Seker, F., Meeker, K., Kuech, T.F., and Ellis, A.B. (2000) Surface chemistry of prototypical bulk II-VI and III-V semiconductors and implications for chemical sensing. *Chem. Rev.*, **100** (7), 2505–2536.

123. Yoshihara, T., Druzhinin, S.I., and Zachariasse, K.A. (2004) Fast intramolecular charge transfer with a planar rigidized electron donor/acceptor molecule. *J. Am. Chem. Soc.*, **126** (27), 8535–8539.

124. Slama-Schwok, A., Blanchard-Desce, M., and Lehn, J.M. (1990) Intramolecular charge transfer in donor-acceptor molecules. *J. Phys. Chem.*, **94** (10), 3894–3902.

125. Tamai, K., Murakami, K., Hosokawa, S., Asakura, H., Teramura, K., and Tanaka, T. (2017) Visible-Light Selective Photooxidation of Aromatic Hydrocarbons via

Ligand-to-Metal Charge Transfer Transition on Nb2O5. *J. Phys. Chem. C*, **121** (41), 22854–22861.

126. Sevov, C.S., Hickey, D.P., Cook, M.E., Robinson, S.G., Barnett, S., Minteer, S.D., Sigman, M.S., and Sanford, M.S. (2017) Physical Organic Approach to Persistent, Cyclable, Low-Potential Electrolytes for Flow Battery Applications. *J. Am. Chem. Soc.*, **139** (8), 2924–2927.

127. Chirik, P.J., and Wieghardt, K. (2010) Radical ligands confer nobility on base-metal catalysts. *Science (80-.).*, **327** (5967), 794–795.

128. Kaim, W. (2011) Manifestations of noninnocent ligand behavior. *Inorg. Chem.*, **50** (20), 9752–9765.

129. Small, B.L., Brookhart, M., and Bennett, A.M.A. (1998) Highly active iron and cobalt catalysts for the polymerization of ethylene [18]. *J. Am. Chem. Soc.*, **120** (16), 4049–4050.

130. Lyaskovskyy, V., and de Bruin, B. (2012) Redox Non-Innocent Ligands: Versatile New Tools to Control Catalytic Reactions. *ACS Catal.*, **2** (2), 270–279.

131. Docherty, J.H., Peng, J., Dominey, A.P., and Thomas, S.P. (2017) Activation and discovery of earth-abundant metal catalysts using sodium tert-butoxide. *Nat. Chem.*, **9** (6), 595–600.

132. Bol, A.A., and Meijerink, A. (2001) Luminescence quantum efficiency of nanocrystalline ZnS:Mn2+: 2. Enhancement by UV irradiation. *J. Phys. Chem. B*, **105** (42), 10203–10209.

133. Xu, L., Chen, K., El-Khair, H.M., Li, M., and Huang, X. (2001) Enhancement of band-edge luminescence and photo-stability in colloidal CdSe quantum dots by various surface passivation technologies. *Appl. Surf. Sci.*, **172** (1–2), 84–88.

134. Yoo, D., Woo, J.Y., Kim, Y., Kim, S.W., Wei, S.H., Jeong, S., and Kim, Y.H. (2020) Origin of the Stability and Transition from Anionic to Cationic Surface Ligand Passivation of All-Inorganic Cesium Lead Halide Perovskite Nanocrystals. *J. Phys. Chem. Lett.*, **11** (3), 652–658.

135. Frederick, M.T., and Weiss, E.A. (2010) Relaxation of exciton confinement in CdSe quantum dots by modification with a conjugated dithiocarbamate ligand. *ACS Nano*, **4** (6), 3195–3200.

136. Bart, S.C., Lobkovsky, E., and Chirik, P.J. (2004) Preparation and molecular and electronic structures of iron(0) dinitrogen and silane complexes and their application to catalytic hydrogenation and hydrosilation. *J. Am. Chem. Soc.*, **126** (42), 13794–13807.

137. Zhang, J., Tolentino, J., Smith, E.R., Zhang, J., Beard, M.C., Nozik, A.J., Law, M., and Johnson, J.C. (2014) Carrier transport in PbS and PbSe QD films measured by photoluminescence quenching. *J. Phys. Chem. C*, **118** (29), 16228–16235.

138. Zhao, K., Pan, Z., and Zhong, X. (2016) Charge Recombination Control for High Efficiency Quantum Dot Sensitized Solar Cells. *J. Phys. Chem. Lett.*, **7** (3), 406–

417.

139. Tagliazucchi, M., Tice, D.B., Sweeney, C.M., Morris-Cohen, A.J., and Weiss, E.A. (2011) Ligand-controlled rates of photoinduced electron transfer in hybrid CdSe nanocrystal/poly(viologen) films. *ACS Nano*, **5** (12), 9907–9917.

140. Crooker, S.A., Hollingsworth, J.A., Tretiak, S., and Klimov, V.I. (2002) Spectrally Resolved Dynamics of Energy Transfer in Quantum-Dot Assemblies: Towards Engineered Energy Flows in Artificial Materials. *Phys. Rev. Lett.*, **89** (18), 186802.

141. Urieta-Mora, J., García-Benito, I., Molina-Ontoria, A., and Martín, N. (2018) Hole transporting materials for perovskite solar cells: a chemical approach. *Chem. Soc. Rev.*, **47** (23), 8541–8571.

142. Kaim, W. (2012) The Shrinking World of Innocent Ligands: Conventionaland Non-Conventional Redox-Active Ligands. *Eur. J. Inorg. Chem.*, **2012** (3), 343–348.

143. Pitchaiya, S., Natarajan, M., Santhanam, A., Asokan, V., Yuvapragasam, A., Madurai Ramakrishnan, V., Palanisamy, S.E., Sundaram, S., and Velauthapillai, D. (2020) A review on the classification of organic/inorganic/carbonaceous hole transporting materials for perovskite solar cell application. *Arab. J. Chem.*, **13** (1), 2526–2557.

144. Tan, Y., Jin, S., and Hamers, R.J. (2013) Influence of hole-sequestering ligands on the photostability of CdSe quantum dots. *J. Phys. Chem. C*, **117** (1), 313–320.

145. Likharev, K.K. (2008) CMOL: Second life for silicon? *Microelectronics J.*, **39** (2), 177–183.

146. Adir, O., Poley, M., Chen, G., Froim, S., Krinsky, N., Shklover, J., Shainsky-Roitman, J., Lammers, T., and Schroeder, A. (2020) Integrating Artificial Intelligence and Nanotechnology for Precision Cancer Medicine. *Adv. Mater.*, **32** (13), 1901989.

147. Jian, W., Hui, D., and Lau, D. (2020) Nanoengineering in biomedicine: Current development and future perspectives. *Nanotechnol. Rev.*, **9** (1), 700–715.

148. Yun, S., Zhang, Y., Xu, Q., Liu, J., and Qin, Y. (2019) Recent advance in new-generation integrated devices for energy harvesting and storage. *Nano Energy*, **60**, 600–619.

149. Liddle, J.A., and Gallatin, G.M. (2016) Nanomanufacturing: A Perspective. *ACS Nano*, **10** (3), 2995–3014.

150. Yoon, H.S., Lee, H.T., Jang, K.H., Kim, C.S., Park, H., Kim, D.W., Lee, K., Min, S., and Ahn, S.H. (2017) CAD/CAM for scalable nanomanufacturing: A network-based system for hybrid 3D printing. *Microsystems Nanoeng.*, **3** (1), 1–11.

151. Du, X., Zhou, J., Shi, J., and Xu, B. (2015) Supramolecular Hydrogelators and Hydrogels: From Soft Matter to Molecular Biomaterials. *Chem. Rev.*, **115** (24), 13165–13307.

152. Whitesides, G.M., and Grzybowski, B. (2002) Self-assembly at all scales. *Science (80-.).*, **295** (5564), 2418–2421.

153. Li, Y., Wang, Y., Huang, G., and Gao, J. (2018) Cooperativity Principles in Self-Assembled Nanomedicine. *Chem. Rev.*, **118** (11), 5359–5391.

154. Zeng, F., and Zimmerman, S.C. (1997) Dendrimers in supramolecular chemistry: From molecular recognition to self-assembly. *Chem. Rev.*, **97** (5), 1681–1712.

155. Thota, B.N.S., Urner, L.H., and Haag, R. (2016) Supramolecular architectures of dendritic amphiphiles in water. *Chem. Rev.*, **116** (4), 2079–2102.

156. Rosen, B.M., Wilson, C.J., Wilson, D.A., Peterca, M., Imam, M.R., and Percec, V. (2009) Dendron-mediated self-assembly, disassembly, and self-organization of complex systems. *Chem. Rev.*, **109** (11), 6275–6540.

157. Habibi, Y., Lucia, L.A., and Rojas, O.J. (2010) Cellulose nanocrystals: Chemistry, self-assembly, and applications. *Chem. Rev.*, **110** (6), 3479–3500.

158. Boles, M.A., Engel, M., and Talapin, D. V. (2016) Self-Assembly of Colloidal Nanocrystals: From Intricate Structures to Functional Materials. *Chem. Rev.*, **116** (18), 11220–11289.

159. Leininger, S., Olenyuk, B., and Stang, P.J. (2000) Self-Assembly of Discrete Cyclic Nanostructures Mediated by Transition Metals. *Chem. Rev.*, **100** (3), 853–907.

160. Shimizu, T., Ding, W., and Kameta, N. (2020) Soft-Matter Nanotubes: A Platform for Diverse Functions and Applications. *Chem. Rev.*, **120** (4), 2347–2407.

161. Said-Mohamed, C., Niskanen, J., Karesoja, M., Pulkkinen, P., Tenhu, H., Daoud, M., and Lee, L.T. (2011) Interparticle distance in monolayers controlled by soft spacers. *Soft Matter*, **7** (15), 7112–7122.

162. Melton, C., Riahinasab, S., Keshavarz, A., Stokes, B., and Hirst, L. (2018) Phase Transition-Driven Nanoparticle Assembly in Liquid Crystal Droplets. *Nanomaterials*, **8** (3), 146.

163. Riahinasab, S.T., Elbaradei, A., Keshavarz, A., Stokes, B.J., and Hirst, L.S. (2017) Nanoparticle microstructures templated by liquid crystal phase-transition dynamics. *Emerg. Liq. Cryst. Technol. XII*, **10125**, 1012503.

164. Amaral, J.J., Betady, E., Quint, M.T., Martin, D., Riahinasab, S.T., Hirst, L.S., and Ghosh, S. (2016) Effect of mesogenic ligands on short and long-term spectral dynamics and stability of core–shell CdSe/ZnS quantum dots. *Mater. Res. Express*, **3** (10), 105029.

165. Savage, J.R., Hopp, S.F., Ganapathy, R., Gerbode, S.J., Heuer, A., and Cohen, I. (2013) Entropy-driven crystal formation on highly strained substrates. *Proc. Natl. Acad. Sci. U. S. A.*, **110** (23), 9301–9304.

166. Atzin, N., Guzmán, O., Gutiérrez, O., Hirst, L.S., and Ghosh, S. (2018) Free-energy model for nanoparticle self-assembly by liquid crystal sorting. *Phys. Rev.*

E, **97** (6), 062704.

167. Bartolo, M.D., Brisbin, R.P., Fettinger, J.C., Ghosh, S., and Baxter, R.D. (2020) Impact of Bis(imino)pyridine Ligands on Mesoscale Properties of CdSe/ZnS Quantum Dots. *J. Phys. Chem. C*, **124** (41), 22677–22683.

168. Quint, M.T., Sarang, S., Quint, D.A., Keshavarz, A., Stokes, B.J., Subramaniam, A.B., Huang, K.C., Gopinathan, A., Hirst, L.S., and Ghosh, S. (2017) Plasmon-actuated nano-assembled microshells. *Sci. Rep.*, **7** (1), 17788.

169. Bartolo, M., Amaral, J.J., Hirst, L.S., and Ghosh, S. (2019) Directed assembly of magnetic and semiconducting nanoparticles with tunable and synergistic functionality. *Sci. Rep.*, **9** (1), 1–11.

170. Rodarte, A.L., Nuno, Z.S., Cao, B.H., Pandolfi, R.J., Quint, M.T., Ghosh, S., Hein, J.E., and Hirst, L.S. (2014) Tuning quantum-dot organization in liquid crystals for robust photonic applications. *Chemphyschem*, **15** (7), 1413–21.

171. Rey, A.D., and Herrera-Valencia, E.E. (2014) Dynamic wetting model for the isotropic-to-nematic transition over a flat substrate. *Soft Matter*, **10** (10), 1611–1620.

172. Popa-Nita, V., Gerlič, I., and Kralj, S. (2009) The Influence of Disorder on Thermotropic Nematic Liquid Crystals Phase Behavior. *Int. J. Mol. Sci.*, **10** (9), 3971–4008.